

MOTION-BASED SENSING AND IMAGING IN SCATTERING MEDIA USING
SPECKLE INTENSITY CORRELATION

A Dissertation

Submitted to the Faculty

of

Purdue University

by

Qiaoen Luo

In Partial Fulfillment of the

Requirements for the Degree

of

Doctor of Philosophy

December 2019

Purdue University

West Lafayette, Indiana

THE PURDUE UNIVERSITY GRADUATE SCHOOL
STATEMENT OF DISSERTATION APPROVAL

Dr. Kevin Webb, Chair

School of Electrical Engineering

Dr. Dan Jiao

School of Electrical Engineering

Dr. Mark Bell

School of Electrical Engineering

Dr. Okan Ersoy

School of Electrical Engineering

Approved by:

Dr. Dimitrios Peroulis

Head of the School Graduate Program

To my family, whose support, patience, and love made this possible.

ACKNOWLEDGMENTS

This work would not have been possible without the guidance and support of my professors, peers, family, and friends. In particular, I would like to acknowledge my advisor Kevin Webb for his optimistic outlook and assiduous drive for true knowledge and important understanding. I would also like to thank Mark Bell, Okan Ersoy, and Dan Jiao for being on my committee and whose classes provided me with the fundamentals necessary to accomplish this work. I thank Justin Patel and Ryan Hastings for their contributions to the projects we worked on together. I also thank the rest of our group members, Brian, Yulu, Li-fan, and Yu-chun just to name a few, for their support and friendship over the years.

TABLE OF CONTENTS

	Page
LIST OF FIGURES	vii
ABSTRACT	xi
1 Introduction	1
2 REFRACTIVE INDEX DISTRIBUTION OF OBJECT HIDDEN INSIDE HEAVILY SCATTERING MEDIA [†]	5
2.1 Theory	6
2.2 Simulated Reconstruction	12
2.3 Conclusion	17
3 MOTION-BASED COHERENT OPTICAL IMAGING IN HEAVILY SCAT- TERING RANDOM MEDIA [†]	19
3.1 Theory	21
3.2 Experiments	24
3.3 Conclusion	29
4 SPECKLE INTENSITY CORRELATIONS OVER OBJECT POSITION FOR SENSING AND IMAGING IN A HEAVILY SCATTERING MEDIUM	31
4.1 Introduction	31
4.2 Theory	34
4.3 Experiments	37
4.4 Conclusion	44
5 THE THEORY OF SPECKLE INTENSITY CORRELATIONS OVER OB- JECT POSITION	46
5.1 Introduction	46
5.2 Object Parameterization	49
5.3 Detected Field Moments	51
5.4 Relationship Between Object and Detected Field Moments	53

	Page
5.5 Physical Basis of $g_{ss}^{(1)}(\Delta\mathbf{r})$ and $g_{bs}^{(1)}(\Delta\mathbf{r})$	56
5.6 Detector Intensity Correlation	58
5.7 Correlation Length Scales, Object Scattering Regimes and Experimental Evidence	61
5.7.1 $\Delta\mathbf{r} \gg \lambda$	62
5.7.2 $\Delta\mathbf{r} < \lambda$	63
5.7.3 $\langle I_{db} \rangle \gg \langle I_{ds} \rangle$	64
5.7.4 $\langle I_{db} \rangle \ll \langle I_{ds} \rangle$	64
5.8 Sensing and Imaging Methodology	65
5.8.1 Formation of Averages ($\langle \cdot \rangle$) with Experimental Data	65
5.8.2 $\langle I_{db} \rangle = 0$: Aperture in a Screen	66
5.8.3 $\langle I_{db} \rangle \neq 0$: General Object	66
5.9 Applications and Perspectives	67
5.10 Conclusion	71
6 ENHANCED COHERENT SENSING USING A SCATTERING ANALYZER VIA SPECKLE CORRELOGRAPHY	73
6.1 Introduction	73
6.2 Theory	74
6.3 Experiment	77
6.4 Simulation	81
6.5 Conclusion	84
7 Summary	85
REFERENCES	87
VITA	95

LIST OF FIGURES

Figure	Page
1.1 A typical speckle image from an experiment with fully developed speckle statistics. No information about the imaging system is apparent in the image. However, collections of speckle images can be used by correlation analysis to obtain information about the scattering medium, the illumination source, and the objects embedded within the scattering medium. . . .	3
2.1 (a) Conceptual for imaging a moving object hidden within a scattering medium by collecting speckle intensity images as a function of object position. (b) Experiment with an 850 nm laser illuminating a pair of scattering slabs. An object was placed between the slabs and scanned using a set of linear stages. Speckle images were collected at each object position using a 4-f spatial filter, magnifying optics, and a polarizer.	7
2.2 (a) Spatial speckle intensity correlation for a 1000 μm and a 500 μm diameter circular aperture placed between two scattering slabs, a 3 mm thick slab between the laser and aperture and a 9 mm thick slabs between the aperture and camera, with $\mu'_s = 4 \text{ cm}^{-1}$. Our theoretical result for the correlation, (2.18), matches very well to the experimental results. (b) 2D spatial intensity correlation from measured speckle patterns as a function of object position the 500 μm diameter aperture moving between the two scattering slabs. (c) Reconstructed image of the hidden 500 μm circular aperture using the experimental intensity correlation data over object position in (b).	14
2.3 Speckle correlations measured through a total of 12 mm of scattering material with $\mu'_s = 4 \text{ cm}^{-1}$, a 3 mm thick slab between the rod and the laser and a 9 mm slab between the object and the camera, for three square rods, 8 mm on each side: $\mu'_s = 4 \text{ cm}^{-1}$, $\mu'_s = 14 \text{ cm}^{-1}$, and a black absorbing rod. The spatial speckle correlation is able to clearly show their movement and distinguish them one from another. (a) For large movement, the correlation corresponds to the physical size of the objects. (b) For wavelength-scale movement, the decorrelation is primarily due to the sub-wavelength features of the embedded scatterers.	16

Figure	Page
3.1 (a) A coherent 850 nm laser diode illuminates a scanned object located between two scattering slabs. A small spot on the back of the right-hand scattering slab was imaged by the camera through a 4-f system, a magnifying lens (so that speckle spots are larger than a pixel), and a polarizer (to provide zero-mean circular Gaussian fields). Speckle patterns were collected as a function of object position in the $x - y$ plane. (b) The normalized speckle correlation for the hidden circular patch is shown as a function of object translation $(\Delta x, \Delta y)$, along with central regions of actual speckle patterns taken at three positions along the y -direction (y_1, y_2, y_3) . Using all camera pixels, pairs of normalized speckle patterns taken at different object positions such as $(0, y_1)$ and $(0, y_2)$, are used to compute cross-correlation coefficients with displacements of the object $(0, d_y)$. The cross-correlation coefficients having the same displacement are averaged, then interpolated in a 2D space for reconstruction.	20
3.2 (a) A photograph of a black 7.5 mm diameter patch in front of a scattering slab. Each slab is 6 mm thick with $\mu'_s = 4 \text{ cm}^{-1}$. (b) The two scattering slabs are separated by a distance of 5 cm. (c) The object cannot be seen through the slab.	21
3.3 (a) Photograph of a circular black vinyl patch object having a diameter of 7.5 mm that was hidden between two 6 mm-thick acrylic scattering slabs having $\mu'_s = 4 \text{ cm}^{-1}$. (b) Measured (blue) and simulated (green, using (3.8)) normalized intensity speckle correlations, with data collected in the experiment described by Fig. 3.1. (c) The reconstructed image of the circular patch, showing a geometry true to the object size.	26
3.4 Aperture objects reconstructed from speckle intensity correlations over object position. (a) Photograph of the "LUX" object. (b) Interpolated measured speckle intensity correlation for the LUX object between 3-(source side) and 9-mm (detector side) scattering acrylic slabs ($\mu'_s = 4 \text{ cm}^{-1}$). (c) Reconstructed image for the "LUX" object. (d) Photograph of the " π " object. (e) Interpolated measured intensity correlation for the " π " aperture located between two fresh chicken breast slices, 2 mm thick on the source side and 7 mm thick on the detector side. (f) Reconstructed image for the " π " object.	28
4.1 Concept figure for imaging and sensing a moving object in a scattering environment.	33
4.2 The experimental setup for measuring the speckle intensity correlation of a moving circular patch translated along the y -axis between two scattering layers. Speckle patterns are collected at the camera after passing through a spatial filter and a polarizer.	37

Figure	Page	
4.3	Example heavily scattering material used in our experiments. (a) Two 6 mm, $\mu'_s = 4\text{cm}^{-1}$ slabs of acrylic are placed on top of a page with printed stripes. Through one 6 mm thick slab, one can no longer distinguish individual stripes, and through a total of 12 mm, it is not possible to distinguish the striped area. (b) The centrally cropped speckle patterns for a moving 4 mm circular patch placed between a 4-ground-glass stack and a 6-ground-glass stack are highly-decorrelated over an object displacement of about 2.5 mm.	38
4.4	Intensity correlations over object position with various patch size, and hence, varying degree of object scatter. (a) Keeping the same slab configuration (a four-piece ground glass diffuser at the laser side and a 6 mm thick $\mu'_s = 4\text{cm}^{-1}$ acrylic slab at the detector side), the measured intensity correlations are shown for circular patches having diameters of 3.7, 5, and 6 mm. The larger the size of the object, the deeper the decorrelation dip. (b) The scaled decorrelation of each circular patch ($ g_{ss}^{(1)}(\Delta\mathbf{r}) ^2$) in (4.11)) agrees well with our prediction using (4.2) for $\Delta\mathbf{r}$ smaller than the object's size. The measured correlation increases after the minimum because the speckle patterns become similar to the bright background as the object is displaced away from the center.	40
4.5	Intensity correlations over object position with various amounts of scatter on either side of the object of interest, which is a circular patch of 3.7 mm in diameter. (a) and (c) show the measured correlation and the rescaled correlation for different amounts of scatter on the detector side (gg represents the number of ground glass used, and mm represents the thickness of acrylic slab). (b) and (d) show the measured correlation and the rescaled correlation for different amounts of scatter on the laser side. The measured correlation decreases at a slower rate to a larger minimum when more environmental scatter is present. The scaled speckle correlation ($ g_{ss}^{(1)}(\Delta\mathbf{r}) ^2$) agrees with the magnitude squared of the autocorrelation of the circular patch of 3.7 mm in diameter except for the case of 3 mm acrylic slab at the laser side, for which laser heating dominates the change in speckle pattern.	42
5.1	A moving object in a scattering medium to be imaged, along with the spatial variables and the optical excitation and detection concept.	48
6.1	Experimental setup. The diffusing object of interest was translated in the transverse plane, along the y axis.	78

Figure	Page
6.2 The averaged correlation over the translation of object decreases at different rate for different analyzer configuration. The more scattering the analyzer is, faster the decorrelation becomes. With a thicker analyzer, we are able to sense sub-wavelength (< 850 nm) translation of the diffusing object.	79
6.3 Experimental configurations other than the analyzer thickness can also affect sensitivity by varying the speckle spot size incident on the analyzer, which is a function of the area of the speckle spread and the distance between the diffusing object and the analyzer [3]. (a) The more-scattering 3 mm thick acrylic slab produces faster decorrelation when compared to 1 moving ground glass (1 GG), as the larger spread of speckle intensity exiting the acrylic slab result in larger speckle spots incident on the analyzer, producing faster decorrelation. (b) The rate of speckle decorrelation increases for a shorter separation between the diffusing moving object (1-ground-glass slab) and the analyzer(3-mm-thick acrylic slab).	80
6.4 Numerical simulation geometry. (a) The overall geometry of the simulations: the center of the domain is the $46\text{-}\mu\text{m}$ -long slab, consisting of 200-nm square scatterers (in blue) randomly distributed in the space with a fill factor of 50%. (b) The zoomed-in view of the geometry, with the detection plane of $42.6\text{ }\mu\text{m}$ labeled by the red line, collecting the total field at half wavelength away from the slab's right side. The wavelength used for the plane wave propagating from the left to the right is chosen as 850 nm.	81
6.5 The collective histogram distribution (plotted as a curve of 30 bins) of the normalized transmission eigenvalues, \tilde{T} , of the transmission matrices for slabs of randomly distributed scatterers of different thickness. Each histogram contains 50 independently generated random configurations of the scattering slab of either $8\text{ }\mu\text{m}$, $6\text{ }\mu\text{m}$, or $4\text{ }\mu\text{m}$. The x-axis rescaled so that 1 is the mean of the transmission eigenvalues of an analyzer, \bar{T} . For a thicker slab, there are more "closed" channels (\tilde{T} close to 0), and the few "open" channels are more transmitting, carrying a larger proportion of the power (maximum \tilde{T} is larger).	83

ABSTRACT

Luo, Qiaoen Ph.D., Purdue University, December 2019. Motion-based Sensing and Imaging in Scattering Media Using Speckle Intensity Correlation. Major Professor: Kevin J. Webb Professor.

Optical sensing and imaging inside heavily scattering media are of intense interest because of their importance in biomedical, environmental, and material inspection applications. When coherent light interacts with scatterers, bright and dark intensity regions form, a phenomenon known as speckle. Often viewed as being detrimental, speckle can be exploited to yield useful information with a correlation analysis.

A coherent method is presented for the imaging of a hidden object moving within thick and randomly scattering media using speckle intensity correlations over object position, with the possibility of accessing super-resolution information. With prior information about the moving object's motion, spatial speckle intensity correlations as a function of object position can reveal the hidden object's relative refractive index distribution. Our experimental evidence shows that it is feasible to image complex aperture-type moving objects and circular patches inside scatter that is a magnitude of order heavier than other comparable imaging modalities. Images of the moving object were obtained from speckle intensity correlation data using phase retrieval. Biological tissue was used to demonstrate the possibility of *in vivo* deep-tissue imaging. Speckle intensity correlations are shown to be sensitive to both the scattering strength of the embedded object and the environment, both of which are useful for sensing. We present a general theory that describes this influence of the background scattering medium and allows for imaging a hidden moving object. Additionally, we present a method to improve the sensitivity of speckle correlography in remote optical metrology. By placing a scattering slab in front of the detector, we demonstrate

enhanced sensitivity, detecting the subwavelength in-plane displacement of a remote diffuse object.

1. INTRODUCTION

Speckle phenomena are the result of the constructive and destructive interference between wavefronts. It been long perceived as detrimental yet inevitable for most conventional coherent optical sensing and imaging approaches when random scatter is involved [1]. Speckle is seen in situations spanning the entire electromagnetic spectrum and other wave types, for example, acoustic waves [2]. While suppression methods can be introduced to alleviate the undesirable random noise associated with speckle [3], researchers have also explored the useful statistical properties of speckle to obtain information previously thought to be lost. Specifically, the correlation over change in laser frequency can be used to image hidden inhomogeneities [4]; the local speckle contrast ratio can be a quantitative indicator of the velocity distribution of blood flow close to the surface [5]; and the temporal decorrelation of speckle patterns forms the basis of diffusing wave spectroscopy, useful for characterizing various dynamic scattering media [6]. The intensity interferometer pioneered by Hanbury Brown and Twiss used correlated intensity measurements with two detectors to access an object's spatial frequency spectrum [7, 8]. The underlying principle can be extended to intensity measurements through a 2D detector array: the van Cittert-Zernike theorem [9] enables the imaging of diffuse object illuminated coherently through averaging intensity correlations and phase retrieval [10], and imaging of an illumination pattern through diffuse surface was achieved using a similar analysis [11]. The memory effect [12, 13] theorizes that the object's spatial information can be retained within a small range of incident angles while the scattering medium is thin. Thus, the auto-correlation of a single speckled measurement can be used to obtain the image of the obscured intensity pattern from fluorescence and patterned apertures [14, 15].

Zero-mean Gaussian field statistics describe a fully developed speckle pattern [3], as shown in Fig. 1.1. A fully developed speckle pattern occurs when light is multiply

scattered. Under such field statistics, Reed’s moment theorem can be used to access second-order field correlations using the fourth-order field correlations obtainable from speckled intensity measurements [16]. This enables the study of speckle correlation over different parameters, yielding interesting information about the unknown system, such as the temporal response of a random medium [17].

For a moving field incident on a heavily scattering static medium, speckle patterns taken at different incident field positions differ solely due to the moving field. If the relative locations of the moving field are known, we can access the hidden incident field from the speckle decorrelation averaged over different scatterer configurations [18,19]. Similarly, speckle intensity correlations over object position can lead to the sensing and imaging of an object moving inside heavily scattering medium with no theoretical limitation of the amount of scatter. This is the focus of this thesis.

Chapter 2 presents the theory for accessing the hidden moving object’s relative refractive index and provides the simulated reconstruction of a pinhole experimentally translated between two scattering slabs [20]. In Chapter 3, it is shown that speckle correlations over object position can be used in combination with phase retrieval for practical image reconstruction of complex aperture-typed objects and an obstructing circular patch, inside fresh chicken breast tissue and thick acrylic slabs [21]. In Chapter 4, it is shown that our approach can be used to image optically absorptive and small objects, and is sensitive to the scattering strength of the surrounding environment as well, which is useful for sensing. Chapter 5 details the general mathematical framework that describes speckle intensity correlations as a function of object position for sensing and imaging moving objects embedded in heavily scattering random media, and its various applications in different length scales and scattering strengths are discussed. Equipped with this understanding, our framework points to the possibility of super-resolution sensing and imaging applications in areas such as semiconductor defect detection.

As an extension of our speckle spatial intensity correlation studies, a simple approach for improving speckle correlography [22,23], a well-established optical metrol-

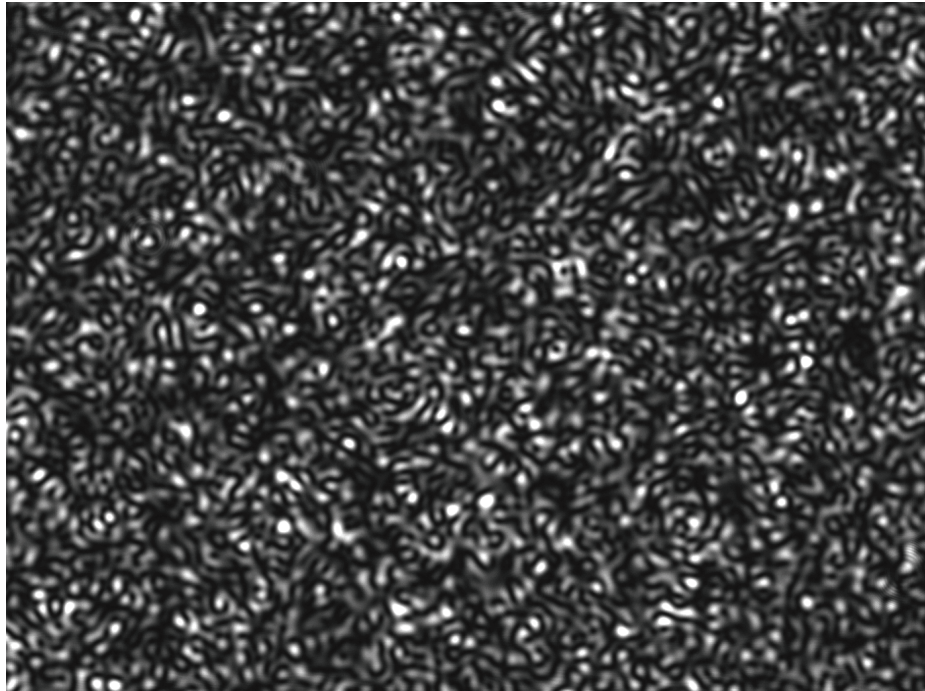


Fig. 1.1. A typical speckle image from an experiment with fully developed speckle statistics. No information about the imaging system is apparent in the image. However, collections of speckle images can be used by correlation analysis to obtain information about the scattering medium, the illumination source, and the objects embedded within the scattering medium.

ogy approach, is presented in Chapter 6. By adding a static scattering material in front of the detector as an analyzer, enhanced sensitivity of speckle correlation to remote subwavelength translation of a diffuse object is observed. The cause of the enhanced sensitivity is discussed in relation to random matrix theory [24]. This simple modification has broad impact and can improve various coherent optical metrology applications, and facilitate temperature sensing and defect detection.

2. REFRACTIVE INDEX DISTRIBUTION OF OBJECT HIDDEN INSIDE HEAVILY SCATTERING MEDIA[†]

The ability to image through scattering media with light has garnered immense interest throughout the last several years [14, 19, 25–29]. However, randomly scattering inhomogeneities in the imaging environment interact with the object of interest and the illumination source and, with sufficient scatter, can completely obscure the object [3]. We provide a new method to coherently image a moving object hidden in heavily scattering media.

The memory effect permits imaging through thin randomly scattering media [12, 14, 30]. Also, using wavefront control, it has been possible to focus through a scattering domain [29], hinting at the future promise with, for instance, ultrasonic guide stars [31]. Wavefront control has been combined with the memory effect to image through thin scattering media [14, 15, 32]. Also, measurement of the transmission matrix for the random medium provides information that can allow for imaging through random scatter [33], but this requires suitable characterization data.

A number of localization methods has been developed. For example, with a stationary point scatterer of interest in a background of moving scatters, the average intensity transmission can yield the position of the stationary scatterer, and transverse localization information exists in the average of the difference of speckle patterns (with and without the stationary scatterer) [34]. Localization can also be accomplished in a diffusion framework, with weakly interacting scatterers, [35, 36]. Control of the coherence in speckle pattern difference images can reveal the presence of hidden inhomogeneities [4].

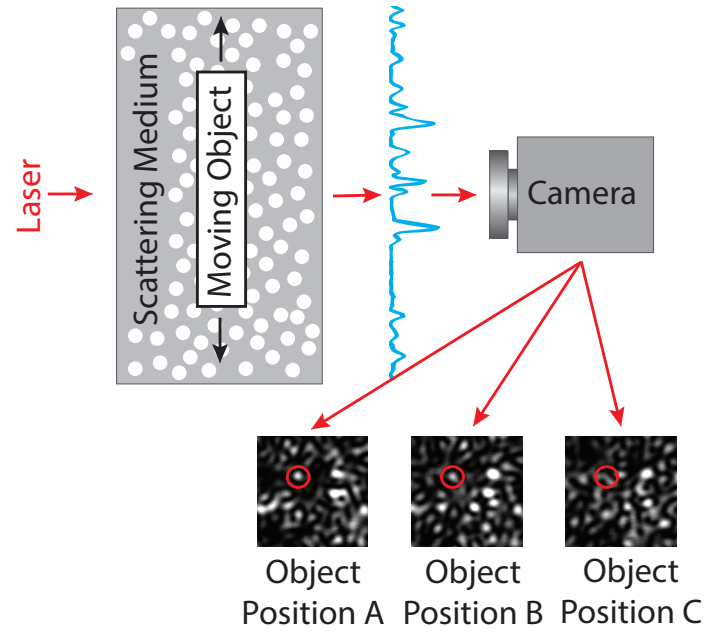
[†] This work is published as J. A. Newman, Q. Luo, and K. J. Webb, “Imaging hidden objects with spatial speckle intensity correlations over object position,” *Phys. Rev. Lett.*, **116**, 073902, 2016 (Ref. [20])

Sophisticated imaging methods have been developed for diffuse optical tomography to achieve geometrical features roughly defined by the transport length, l^* [37,38]. Greater accuracy can be achieved with high energy photons, where ballistic information (that allows back-projection, for instance) provides tracking data in X-ray phase contrast imaging [39] with use of geometrical optics [40]. However, beyond the physics related to multiply scattering light, use of visible infrared light can be desirable to allow various forms of spectroscopy, and for cost, safety and technology reasons.

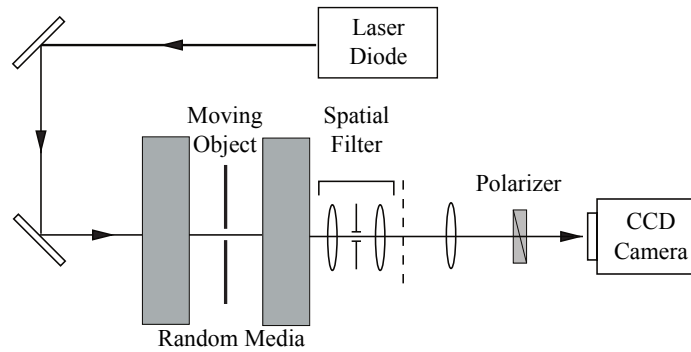
The aforementioned and related prior work leads to the position that imaging with wavelength scale resolution in multiply scattering media has been limited to the degree of scatter where wavefront control (with a guide star) or the memory effect can be applied. We show a means to achieve high resolution optical images with multiply scattered coherent light through essentially arbitrarily thick scattering media, limited only by signal-to-noise requirements at the detector, when speckle images are captured as a function of object position.

2.1 Theory

We demonstrate a method for imaging moving objects embedded within thick, randomly scattering media that applies provided there is enough scatter to have randomized fields that are zero-mean circular Gaussian [1]. In this scattering regime, our method is not limited by the thickness of the scattering medium, making it complementary to existing speckle imaging approaches [41]. The approach, illustrated in Fig. 2.1(a), provides a description of the spatial speckle intensity correlation as a function of object position for a moving object hidden inside of a scattering medium, and allows for the moving hidden object to be imaged. We describe the environment as a static random scattering medium with an embedded object at some position inside the random medium. However, in reality, the randomly scattering medium only needs to be static during a particular span of time. We define the normalized intensity for polarized light exiting a random medium as $\tilde{I} = (I - \langle I \rangle) / \sigma_I$, where $\langle I \rangle$



(a)



(b)

Fig. 2.1. (a) Conceptual for imaging a moving object hidden within a scattering medium by collecting speckle intensity images as a function of object position. (b) Experiment with an 850 nm laser illuminating a pair of scattering slabs. An object was placed between the slabs and scanned using a set of linear stages. Speckle images were collected at each object position using a 4-f spatial filter, magnifying optics, and a polarizer.

is the mean intensity and σ_I is the standard deviation of the intensity. The speckle contrast ratio [3], $\sigma_I/\langle I \rangle$, is unity for polarized coherent light and fully developed speckle statistics. In this case, the intensity statistics are negative exponential and the underlying field statistics, assuming weakly interacting scatterers, are zero-mean circular Gaussian, a property of the field statistics that we will use.

We write the spatial speckle intensity correlation as $\langle \tilde{I}(\mathbf{r}; \mathbf{r}_o) \tilde{I}(\mathbf{r}; \mathbf{r}_o + \Delta \mathbf{r}_o) \rangle$, where $\tilde{I}(\mathbf{r}; \mathbf{r}_o)$ is the normalized intensity at position \mathbf{r} with an object embedded inside the random scattering medium at a reference position described by \mathbf{r}_o , and the object's movement is described by $\Delta \mathbf{r}_o$. Assuming zero-mean circular Gaussian statistics, we can express the normalized intensity correlation in terms of the normalized field correlation using a moment theorem as [16]

$$\langle \tilde{I}(\mathbf{r}; \mathbf{r}_o) \tilde{I}(\mathbf{r}; \mathbf{r}_o + \Delta \mathbf{r}_o) \rangle = \left| \langle \tilde{E}(\mathbf{r}; \mathbf{r}_o) \tilde{E}^*(\mathbf{r}; \mathbf{r}_o + \Delta \mathbf{r}_o) \rangle \right|^2, \quad (2.1)$$

where $\tilde{E} = E/\sigma_E$ is the normalized scalar field and σ_E is the standard deviation of the field. With zero-mean circular Gaussian fields, $\sigma_E = \langle |E|^2 \rangle^{1/2} = \langle I \rangle^{1/2} = \sqrt{\sigma_I}$ [16,42].

In developing an expression for the imaging problem, we use a scalar wave equation to describe the interaction of the speckled optical field with the object of interest (that is being translated). This corresponds to the physical optics approximation, so that the vector field problem associated with the moving scatterer can be treated by the scalar wave equation. This treatment can be generalized for an arbitrary sized object through use of the vector wave equation.

We write the total field, $E(\mathbf{r}; \mathbf{r}_o)$, as

$$E(\mathbf{r}; \mathbf{r}_o) = E_i(\mathbf{r}) + E_s(\mathbf{r}; \mathbf{r}_o), \quad (2.2)$$

where $E_i(\mathbf{r})$ is the field in the scattering medium without the object and $E_s(\mathbf{r}; \mathbf{r}_o)$ is the field scattered by the object. The wave equation for the electric field, assuming constant permeability, can be written as

$$\nabla^2 [E_i(\mathbf{r}) + E_s(\mathbf{r}; \mathbf{r}_o)] + k_0^2 \epsilon_i(\mathbf{r}) [E_i(\mathbf{r}) + E_s(\mathbf{r}; \mathbf{r}_o)] + k_0^2 \epsilon_s(\mathbf{r}; \mathbf{r}_o) [E_i(\mathbf{r}) + E_s(\mathbf{r}; \mathbf{r}_o)] = 0, \quad (2.3)$$

where $k_0^2 = (2\pi/\lambda_0)^2$, λ_0 is the free-space wavelength, $\epsilon_i(\mathbf{r})$ is the spatially-dependent dielectric constant of the random medium, and $\epsilon_s(\mathbf{r}; \mathbf{r}_o)$ is the difference with and without the embedded object centered at \mathbf{r}_o . Knowing that $\nabla^2 E_i(\mathbf{r}) + k_0^2 \epsilon_i(\mathbf{r}) E_i(\mathbf{r}) = 0$, moving all of the terms containing $\epsilon_s(\mathbf{r}; \mathbf{r}_o)$ to the right hand side, and using (2.2), we write (2.3) as

$$\nabla^2 E_s(\mathbf{r}; \mathbf{r}_o) + k_0^2 \epsilon_i(\mathbf{r}) E_s(\mathbf{r}; \mathbf{r}_o) = -k_0^2 \epsilon_s(\mathbf{r}; \mathbf{r}_o) E(\mathbf{r}; \mathbf{r}_o). \quad (2.4)$$

Using the Green's function solution to (2.4), $G(\mathbf{r}', \mathbf{r}; \mathbf{r}_o)$, we write the scattered field as

$$E_s(\mathbf{r}; \mathbf{r}_o) = \int d\mathbf{r}' E(\mathbf{r}'; \mathbf{r}_o) k_0^2 \epsilon_s(\mathbf{r}'; \mathbf{r}_o) G(\mathbf{r}', \mathbf{r}; \mathbf{r}_o). \quad (2.5)$$

With (2.5), the total field at some point, \mathbf{r} , becomes

$$E(\mathbf{r}; \mathbf{r}_o) = E_i(\mathbf{r}) + k_0^2 \int d\mathbf{r}' E(\mathbf{r}'; \mathbf{r}_o) \epsilon_s(\mathbf{r}'; \mathbf{r}_o) G(\mathbf{r}', \mathbf{r}; \mathbf{r}_o). \quad (2.6)$$

We use (2.6) to write the electric field correlation over object position, at detector position \mathbf{r}_d , as

$$\begin{aligned} \langle E(\mathbf{r}_d; \mathbf{r}_o) E^*(\mathbf{r}_d; \mathbf{r}_o + \Delta \mathbf{r}_o) \rangle &= \left\langle \left[E_i(\mathbf{r}_d) + k_0^2 \int d\mathbf{r}' E(\mathbf{r}'; \mathbf{r}_o) \epsilon_s(\mathbf{r}'; \mathbf{r}_o) G(\mathbf{r}', \mathbf{r}_d; \mathbf{r}_o) \right] \right. \\ &\quad \times \left. \left[E_i^*(\mathbf{r}_d) + k_0^2 \int d\mathbf{r}'' E^*(\mathbf{r}''; \mathbf{r}_o + \Delta \mathbf{r}_o) \epsilon_s^*(\mathbf{r}'' + \Delta \mathbf{r}_o; \mathbf{r}_o + \Delta \mathbf{r}_o) G^*(\mathbf{r}'', \mathbf{r}_d; \mathbf{r}_o + \Delta \mathbf{r}_o) \right] \right\rangle. \end{aligned} \quad (2.7)$$

At this point, we recognize the statistical independence of the various terms in (2.7), such as the field without the scattering object and the scattered field, and use this to separate the averaging. In addition, the final term of the expansion of (2.7) is reduced

to a single integral using the assumption that the contributions to the correlation occur only over the joint support [18], giving

$$\begin{aligned}
\langle E(\mathbf{r}_d; \mathbf{r}_o) E^*(\mathbf{r}_d; \mathbf{r}_o + \Delta \mathbf{r}_o) \rangle &= \langle |E_i(\mathbf{r}_d)|^2 \rangle \\
&+ k_0^2 \langle E_i(\mathbf{r}_d) \rangle \langle \int d\mathbf{r}'' E^*(\mathbf{r}''; \mathbf{r}_o + \Delta \mathbf{r}_o) \epsilon_s^*(\mathbf{r}'' + \Delta \mathbf{r}_o; \mathbf{r}_o + \Delta \mathbf{r}_o) G^*(\mathbf{r}'', \mathbf{r}_d; \mathbf{r}_o + \Delta \mathbf{r}_o) \rangle \\
&+ k_0^2 \langle E_i^*(\mathbf{r}_d) \rangle \langle \int d\mathbf{r}' E(\mathbf{r}'; \mathbf{r}_o) \epsilon_s(\mathbf{r}'; \mathbf{r}_o) G(\mathbf{r}', \mathbf{r}_d; \mathbf{r}_o) \rangle \\
&+ k_0^4 \int d\mathbf{r}' \langle E(\mathbf{r}'; \mathbf{r}_o) E^*(\mathbf{r}'; \mathbf{r}_o + \Delta \mathbf{r}_o) G(\mathbf{r}', \mathbf{r}_d; \mathbf{r}_o) G^*(\mathbf{r}', \mathbf{r}_d; \mathbf{r}_o + \Delta \mathbf{r}_o) \rangle \\
&\times \epsilon_s(\mathbf{r}'; \mathbf{r}_o) \epsilon_s^*(\mathbf{r}' + \Delta \mathbf{r}_o; \mathbf{r}_o + \Delta \mathbf{r}_o). \tag{2.8}
\end{aligned}$$

The second and third terms in (2.8) are zero because $\langle E_i(\mathbf{r}_d) \rangle$ has zero mean. These observations allow us to write (2.8) as

$$\begin{aligned}
\langle E(\mathbf{r}_d; \mathbf{r}_o) E^*(\mathbf{r}_d; \mathbf{r}_o + \Delta \mathbf{r}_o) \rangle &= \langle |E_i(\mathbf{r}_d)|^2 \rangle \\
&+ k_0^4 \int d\mathbf{r}' \langle E(\mathbf{r}'; \mathbf{r}_o) E^*(\mathbf{r}'; \mathbf{r}_o + \Delta \mathbf{r}_o) G(\mathbf{r}', \mathbf{r}_d; \mathbf{r}_o) G^*(\mathbf{r}', \mathbf{r}_d; \mathbf{r}_o + \Delta \mathbf{r}_o) \rangle \\
&\times \epsilon_s(\mathbf{r}'; \mathbf{r}_o) \epsilon_s^*(\mathbf{r}' + \Delta \mathbf{r}_o; \mathbf{r}_o + \Delta \mathbf{r}_o). \tag{2.9}
\end{aligned}$$

With sufficient scatter, the average of the field and Green's function in the last term in (2.9) can be reduced to a slowly varying function of space, C , leading to

$$\langle E(\mathbf{r}_d; \mathbf{r}_o) E^*(\mathbf{r}_d; \mathbf{r}_o + \Delta \mathbf{r}_o) \rangle = \langle |E_i(\mathbf{r}_d)|^2 \rangle + C \int d\mathbf{r}' \epsilon_s(\mathbf{r}'; \mathbf{r}_o) \epsilon_s^*(\mathbf{r}' + \Delta \mathbf{r}_o; \mathbf{r}_o + \Delta \mathbf{r}_o), \tag{2.10}$$

with

$$C = \langle E(\mathbf{r}'; \mathbf{r}_o) E^*(\mathbf{r}'; \mathbf{r}_o + \Delta \mathbf{r}_o) G(\mathbf{r}', \mathbf{r}_d; \mathbf{r}_o) G^*(\mathbf{r}', \mathbf{r}_d; \mathbf{r}_o + \Delta \mathbf{r}_o) \rangle. \tag{2.11}$$

With C in (2.10) constant, the statistics are stationary over object position, such that the field mean and variance are independent of embedded object position, \mathbf{r}_o . The field variance at the detector, $\sigma_E^2 = \langle |E|^2 \rangle$, with E from (2.6), becomes

$$\sigma_E^2 = \left\langle \left| E_i(\mathbf{r}_d) + k_0^2 \int d\mathbf{r}' E(\mathbf{r}'; \mathbf{r}_o) \epsilon_s(\mathbf{r}'; \mathbf{r}_o) G(\mathbf{r}', \mathbf{r}_d; \mathbf{r}_o) \right|^2 \right\rangle. \tag{2.12}$$

Expansion of the terms in (2.12) leads to

$$\begin{aligned}
\sigma_E^2 = & \langle |E_i(\mathbf{r}_d)|^2 \rangle \\
& + k_0^2 \langle E_i(\mathbf{r}_d) \rangle \langle \int d\mathbf{r}' E^*(\mathbf{r}'; \mathbf{r}_o) \epsilon_s^*(\mathbf{r}'; \mathbf{r}_o) G^*(\mathbf{r}', \mathbf{r}_d; \mathbf{r}_o) \rangle \\
& + k_0^2 \langle E_i^*(\mathbf{r}_d) \rangle \langle \int d\mathbf{r}' E(\mathbf{r}'; \mathbf{r}_o) \epsilon_s(\mathbf{r}'; \mathbf{r}_o) G(\mathbf{r}', \mathbf{r}_d; \mathbf{r}_o) \rangle \\
& + k_0^4 \langle \int d\mathbf{r}' E(\mathbf{r}'; \mathbf{r}_o) \epsilon_s(\mathbf{r}'; \mathbf{r}_o) G(\mathbf{r}', \mathbf{r}_d; \mathbf{r}_o) \int d\mathbf{r}'' E^*(\mathbf{r}''; \mathbf{r}_o) \epsilon_s^*(\mathbf{r}''; \mathbf{r}_o) G^*(\mathbf{r}'', \mathbf{r}_d; \mathbf{r}_o) \rangle.
\end{aligned} \tag{2.13}$$

Using the same joint support argument that was used to arrive at (2.9), recognizing that the middle two terms in (2.13) are zero, due to $\langle E_i(\mathbf{r}_d) \rangle$ having zero mean, and again treating the average over the field and Green's function to be slowly varying, (2.13) is reduced to

$$\sigma_E^2 = \langle |E_i(\mathbf{r}_d)|^2 \rangle + C \int d\mathbf{r}' |\epsilon_s(\mathbf{r}'; \mathbf{r}_o)|^2. \tag{2.14}$$

The normalized electric field autocorrelation, at detector position \mathbf{r}_d , is written as

$$\langle \tilde{E}(\mathbf{r}_d; \mathbf{r}_o) \tilde{E}^*(\mathbf{r}_d; \mathbf{r}_o + \Delta \mathbf{r}_o) \rangle = \frac{1}{\sigma_E^2} \langle E(\mathbf{r}_d; \mathbf{r}_o) E^*(\mathbf{r}_d; \mathbf{r}_o + \Delta \mathbf{r}_o) \rangle. \tag{2.15}$$

We use (2.9) and (2.14) in (2.15) to obtain an expression for the normalized electric field spatial correlation in terms of the object's autocorrelation as

$$\langle \tilde{E}(\mathbf{r}_d; \mathbf{r}_o) \tilde{E}^*(\mathbf{r}_d; \mathbf{r}_o + \Delta \mathbf{r}_o) \rangle = \frac{\langle |E_i(\mathbf{r}_d)|^2 \rangle + C \int d\mathbf{r}' \epsilon_s(\mathbf{r}'; \mathbf{r}_o) \epsilon_s^*(\mathbf{r}' + \Delta \mathbf{r}_o; \mathbf{r}_o + \Delta \mathbf{r}_o)}{\langle |E_i(\mathbf{r}_d)|^2 \rangle + C \int d\mathbf{r}' |\epsilon_s(\mathbf{r}'; \mathbf{r}_o)|^2}. \tag{2.16}$$

Equation (2.16) shows that information about the object is available in the measured speckle intensity correlation, obtained from (2.15) using a moment theorem [16]. In the case of no embedded moving object, the second terms in both the numerator and the denominator of (2.16) are zero, leaving us with, as expected, a constant correlation of 1. The mean intensity without the object gives $\langle |E_i(\mathbf{r}_d)|^2 \rangle$, and this can be obtained using a model or a prior measurement without the object. The unknowns

in (2.16) are then two constants, C , as given in (2.11), and $\int d\mathbf{r}' |\epsilon_s(\mathbf{r}'; \mathbf{r}_o)|^2$, and the autocorrelation of the object's spatially dependent dielectric constant. With sufficient measurement data, the two constants and the object (defined by its dielectric constant) can in principle be determined. We consider a special case to simplify and demonstrate the result in (2.16).

With a strongly interacting moving embedded object, the second terms in the numerator and denominator in (2.16) will be much larger than the first term. The resulting complete decorrelation of the speckle image occurs when the difference in dielectric constant of the object and the background, ϵ_s , is much greater than zero and/or the object is large, both resulting in large contrast [43]. When the second term is sufficiently large, (2.16) can be reduced to

$$\langle \tilde{E}(\mathbf{r}_d; \mathbf{r}_o) \tilde{E}^*(\mathbf{r}_d; \mathbf{r}_o + \Delta \mathbf{r}_o) \rangle \approx \frac{\int d\mathbf{r}' \epsilon_s(\mathbf{r}'; \mathbf{r}_o) \epsilon_s^*(\mathbf{r}' + \Delta \mathbf{r}_o; \mathbf{r}_o + \Delta \mathbf{r}_o)}{\int d\mathbf{r}' |\epsilon_s(\mathbf{r}'; \mathbf{r}_o)|^2}. \quad (2.17)$$

We use (2.17) in (2.1) to write the normalized intensity correlation in terms of the field correlation as

$$\langle \tilde{I}(\mathbf{r}_d; \mathbf{r}_o) \tilde{I}(\mathbf{r}_d; \mathbf{r}_o + \Delta \mathbf{r}_o) \rangle \approx \frac{|\int d\mathbf{r}' \epsilon_s(\mathbf{r}'; \mathbf{r}_o) \epsilon_s^*(\mathbf{r}' + \Delta \mathbf{r}_o; \mathbf{r}_o + \Delta \mathbf{r}_o)|^2}{|\int d\mathbf{r}' |\epsilon_s(\mathbf{r}'; \mathbf{r}_o)|^2|^2}. \quad (2.18)$$

Equation (2.18) describes the spatial speckle correlation in terms of the normalized autocorrelation of an embedded moving object, where the object is described in terms of its dielectric constant. The averaging can be assumed to be over the scatterer configuration or, due to the statistical independence of the speckle spots, over detectors at different points, such as pixels in a CCD camera. The use of a CCD camera allows a very large number of independent measurements to be made simultaneously while the embedded object moves.

2.2 Simulated Reconstruction

An inversion of (2.18) allows for the imaging of moving objects hidden within scattering media in terms of the object's optical properties. We emphasize that the resolution of the image is then about one wavelength, dictated by use of propagating

waves. This inversion requires a phase retrieval to determine ϵ_s from its correlation. This phase retrieval could be achieved through various means, such as an iterative phase retrieval where known constraints are applied in the real and Fourier domains [44] or even through the use of the bispectral phase obtained from a third-order correlation over space as a dual variable application of previous frequency correlations [17, 45].

Equation (2.18) was experimentally verified for a special case using the setup shown in Fig. 2.1(b). An 850 nm laser diode with a linewidth less than 10 MHz illuminated a 3 mm thick slab placed between the laser source and the object and a 9 mm thick randomly scattering slab was placed between the camera and the object of interest. The two slabs were separated by 3.5 cm. Both slabs, clear acrylic with embedded 50 nm diameter TiO_2 particles, had a reduced scattering coefficient, an inverse measure of the mean free path, of 4 cm^{-1} . A 4-f spatial filter and magnifying lens were used to control the size of the speckle pattern imaged by a CCD camera. The object of interest was a circular hole in an absorbing sheet. The hole was moved in the plane between the scattering slabs and speckle images were taken as a function of position. The imaging arrangement resulted in a spot about 1 mm in diameter on the back of the scattering medium being imaged to the camera, and the heavy scatter resulted in the measured mean intensity being independent of scan position. These speckle images were then used to calculate the spatial speckle intensity correlation as a function of object position. The data from each of the 480,000 pixels were averaged to form an estimate of the spatial speckle correlation. The experimental results for 500 μm and 1000 μm diameter circular apertures along with the expected correlation using (2.18) (assuming that $\epsilon_s(\mathbf{r}; \mathbf{r}_o)$ was zero at the hole and large and imaginary everywhere else) are shown in Fig. 2.2(a). Excellent agreement between the experimental results and theory is shown, forming a strong basis for the validity of (2.18). Note that $l^* = 2.5 \text{ mm}$ for this scattering medium and that the distance scale in Fig. 2.2 makes it clear the accuracy of the inverted image is very high relative to l^* and should be on the order of the optical wavelength. Figure 2.2(b) shows

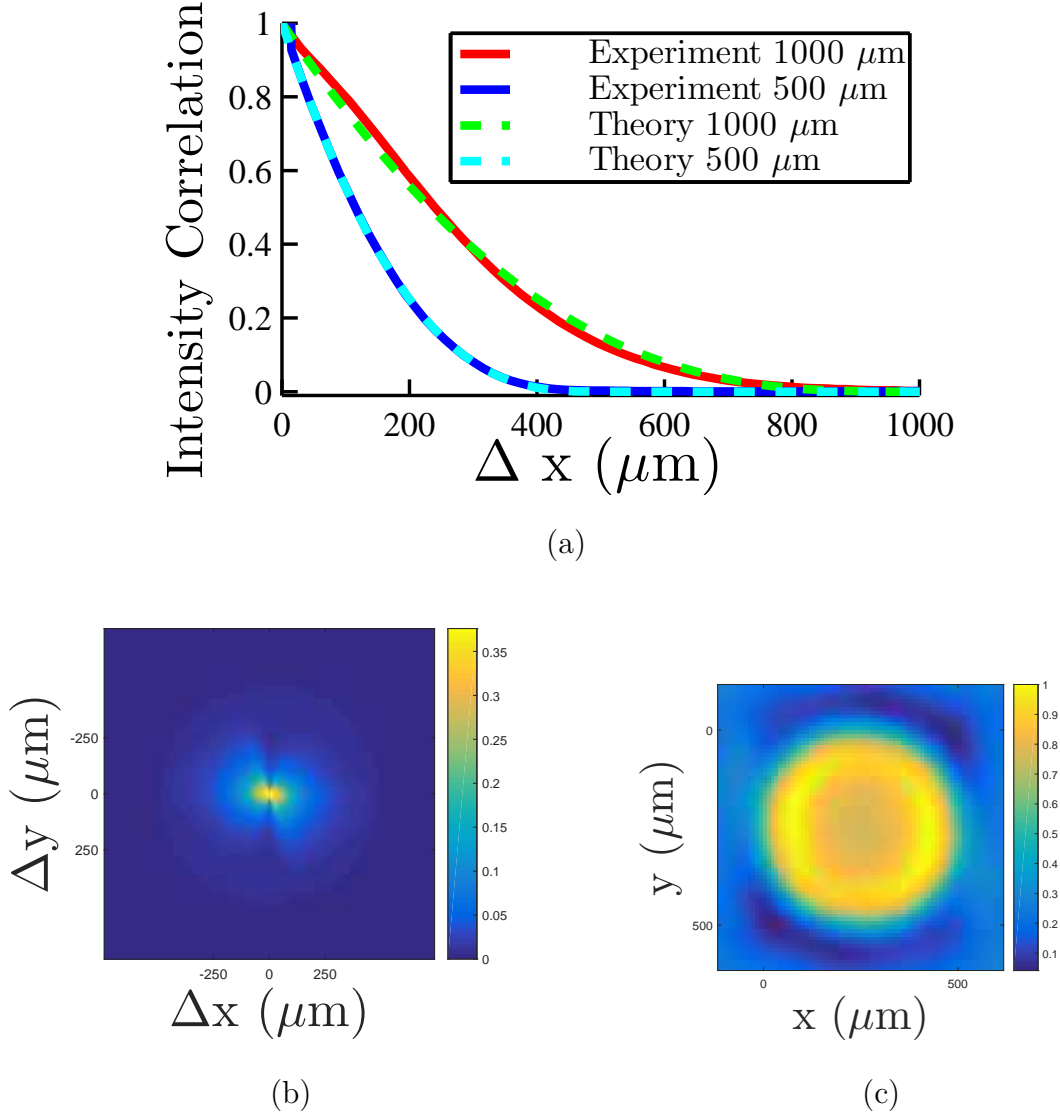
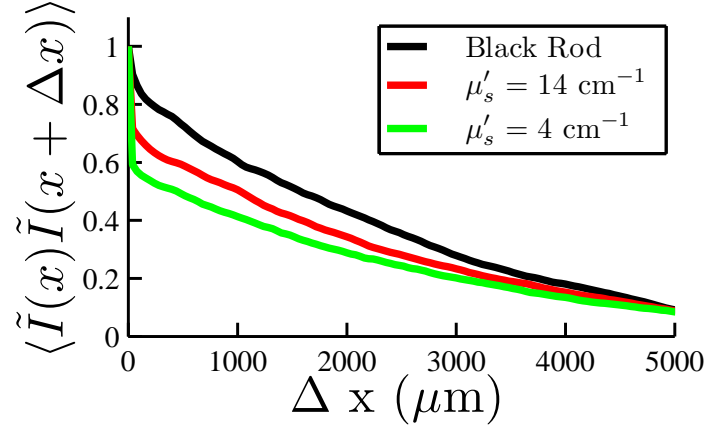


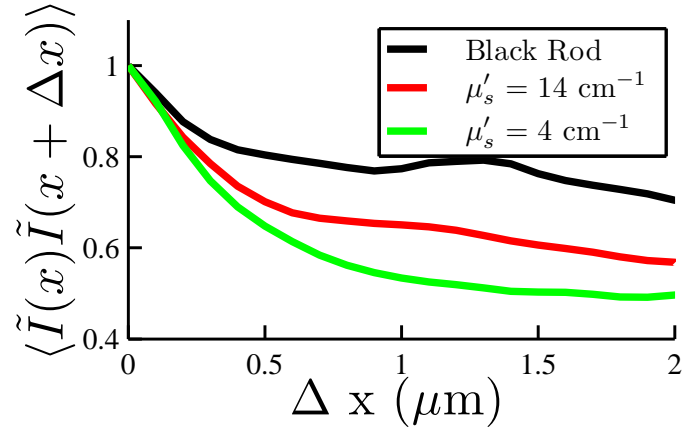
Fig. 2.2. (a) Spatial speckle intensity correlation for a 1000 μm and a 500 μm diameter circular aperture placed between two scattering slabs, a 3 mm thick slab between the laser and aperture and a 9 mm thick slabs between the aperture and camera, with $\mu'_s = 4 \text{ cm}^{-1}$. Our theoretical result for the correlation, (2.18), matches very well to the experimental results. (b) 2D spatial intensity correlation from measured speckle patterns as a function of object position the 500 μm diameter aperture moving between the two scattering slabs. (c) Reconstructed image of the hidden 500 μm circular aperture using the experimental intensity correlation data over object position in (b).

the measured spatial speckle intensity correlation for a $500\ \mu\text{m}$ diameter aperture moving inside the scattering medium. We inverted the measured data to reconstruct an image for the object, as described in (2.18), and obtained the result shown in Fig. 2.2(c). Because the discrete sampling of the correlation was quite coarse in the experiment, the reconstruction selected zero crossings from simulated data. The Fourier domain data was filtered using a 2D Hamming window before the final inverse Fourier transform to arrive at the spatial image shown.

We investigated a set of square cylindrical scattering rods, 8 mm on each side, that were scanned between the same two scattering slabs (3 mm thick on the source side and 9 mm on the detector side, referring to Fig. 2.1(b), with $\mu'_s = 4\ \text{cm}^{-1}$), with camera intensity images captured at each scan position. One rod had the same scattering properties as the slabs, one had a larger reduced scattering coefficient of $\mu'_s = 14\ \text{cm}^{-1}$, and the other was an absorbing black rod. The rods were moved a total distance of 5 mm and speckle images were taken every $40\ \mu\text{m}$. An additional twenty images were taken at $0.1\ \mu\text{m}$ steps. The normalized intensity correlations were calculated from the measured data and the results are shown in Figs. 2.3(a) and (b). The long range correlations in Figure 2.3(a) go to zero at 8 mm, corresponding to the moving object's size. The short range results in Figure 2.3(b) decorrelate on the far-subwavelength scale. This rapid decrease is due to edge movement and the sub-wavelength scale structure of the scattering rods, which are 50 nm diameter TiO_2 spheres. The black rod effectively lets no light pass, so its rough surface movement is the primary contributor to the small decrease, while the $\mu'_s = 14\ \text{cm}^{-1}$ and $\mu'_s = 4\ \text{cm}^{-1}$ rods are increasingly more transmissive, leading to a more significant wavelength-scale decorrelation due to the embedded scatterers. On both length scales, the scatter from the object dictates the decorrelation rate. These correlations are independent of the scattering background because the scatter is heavy enough that the mean intensity measured is independent of object motion over the range used in these experiments. Despite each rod having the same physical dimensions, the spatial speckle correlations are clearly different. This allows us to not only deter-



(a)



(b)

Fig. 2.3. Speckle correlations measured through a total of 12 mm of scattering material with $\mu'_s = 4 \text{ cm}^{-1}$, a 3 mm thick slab between the rod and the laser and a 9 mm slab between the object and the camera, for three square rods, 8 mm on each side: $\mu'_s = 4 \text{ cm}^{-1}$, $\mu'_s = 14 \text{ cm}^{-1}$, and a black absorbing rod. The spatial speckle correlation is able to clearly show their movement and distinguish them one from another. (a) For large movement, the correlation corresponds to the physical size of the objects. (b) For wavelength-scale movement, the decorrelation is primarily due to the sub-wavelength features of the embedded scatterers.

mine that there is an object moving between the slabs, but also to identify the object. For example, these correlations could be used in the classification and identification of objects moving through naturally occurring scattering environments such as tissue, clouds, or other cluttered background. A library of object correlations could be assembled which would allow for the rapid identification of objects without requiring computationally expensive inversions.

2.3 Conclusion

In the imaging method we have described based on the inversion of (2.18) with measured intensity data as a function of object position, the movement of the object does not necessarily have to be controlled and can be due to natural motion. The effective step size would then be determined by the object's velocity and image acquisition time. If the object's motion is not known, then an analogous problem can be described where, assuming that the object is known, the object's motion can be determined and tracked. The speckle intensity correlation can be rewritten in terms of the object's time dependent velocity, $\mathbf{v}(t)$ and time, t , where $\mathbf{r} = \mathbf{r}_0 + \Delta\mathbf{r} = \mathbf{r}_0 + \int_{t_0}^{t_1} \mathbf{v}(t)dt$. This allows for sensing and tracking of hidden objects. Alternatively, if the object's velocity is considered uniform over a time-frame of interest, the resulting correlation could be used to identify the object. We should note that such information related to correlations over object position is distinct from the temporal correlations related to diffusing-wave spectroscopy [6], where a large number of scatterers are producing the decorrelation.

We have presented a theory that allows for imaging (through the inversion of the spatial speckle correlation) moving objects embedded within scattering media at wavelength resolution. This allows for new sensing and imaging opportunities at wavelengths and in scattering regimes that were previously inaccessible. The use of speckle images and various types of correlations, such as the spatial correlations presented here alongside frequency and temporal correlations [14, 17, 27, 28, 46], comprise

a powerful set of tools for the analysis of scattering environments and the ability to sense, track, and image in scattering environments. In tissue, blood cells or contrast agents in vessels could move quickly relative to surrounding tissue that dominates the scatter, conforming to the arrangement assumed. Another relevant situation is a moving object under sea ice or snow, with both the light source and detector above. The work should also impact imaging in various aerosols. Our method applies across a broad range of the electromagnetic spectrum and even for other field-based imaging methods where there is vulnerability to random scatter. All of these applications require methods that can compensate for the subject of interest being embedded inside of a thick scattering environment.

3. MOTION-BASED COHERENT OPTICAL IMAGING IN HEAVILY SCATTERING RANDOM MEDIA[†]

Coherent optical imaging in opaque and randomly scattering material offers the promise of high spatial resolution as well as spectroscopic information. When the scattering medium is thin, the memory effect [12], in which the speckle pattern translates with the incident light angle over a small range, has provided a basis for imaging using fluorescence [14]. Mapping of the field transmission matrix of the scattering medium and its inversion allow contrast-enhanced focusing [47] and point-wise imaging [27]. Wavefront shaping has allowed focusing inside scattering media using measurements with photoacoustic [48] and ultrasound [49] guidestars. Despite such progress, these methods generally become less effective as the amount of scatter or the medium’s thickness increases, a consequence of the underlying principle and increasing experimental and computational complexities. We propose an approach in which heavy scatter is not prohibitive and can actually simplify the theory. Using a physical model combined with phase retrieval, we demonstrate the imaging of absorptive targets and intensity patterns hidden inside a thick scattering domain.

Speckle forms because of the constructive and destructive interference that occurs when coherent light interacts with a random medium. The polarized field statistics due to sufficient scatter with mean scatterer separation large relative to the wavelength, of relevance here, contract to zero-mean circular Gaussian [1, 50]. Previously, with a transmitted field defined by an aperture and a transmission speckle measurement as a function of aperture position, the imaging of a circular aperture scanned between two scattering slabs was demonstrated [20]. We now present a means to image an arbitrary object moving within a scattering medium and show that complex

[†] This work is published as Q. Luo, J. A. Newman, and K. J. Webb, “Motion-based coherent optical imaging in heavily scattering random media,” *Opt. Lett.*, 4(11), 2716-2719, 2019 (Ref. [21])

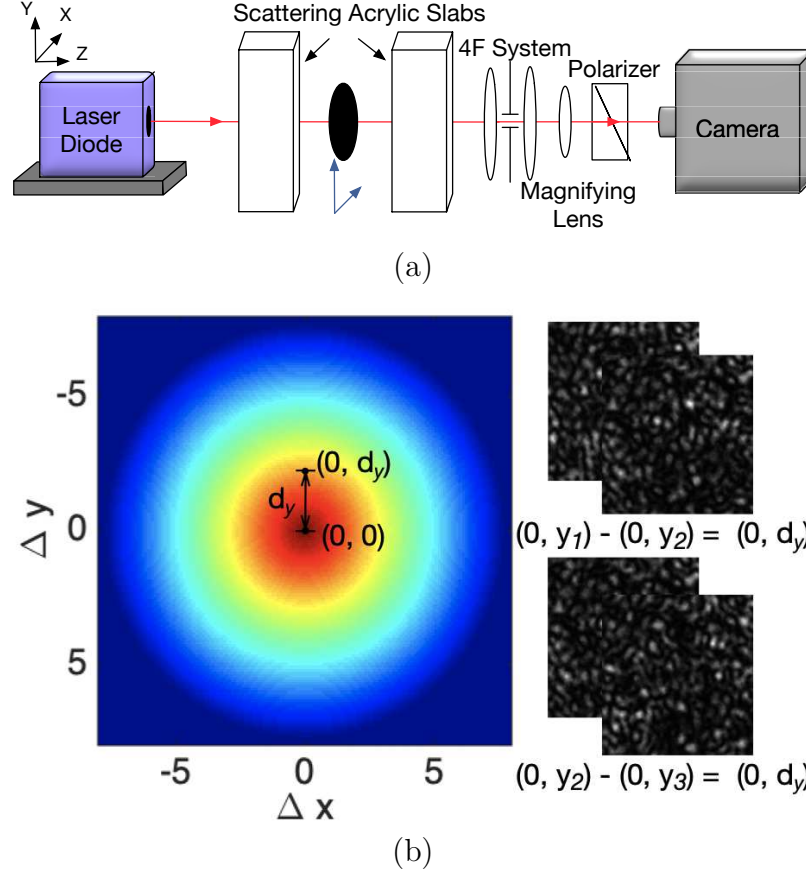


Fig. 3.1. (a) A coherent 850 nm laser diode illuminates a scanned object located between two scattering slabs. A small spot on the back of the right-hand scattering slab was imaged by the camera through a 4-f system, a magnifying lens (so that speckle spots are larger than a pixel), and a polarizer (to provide zero-mean circular Gaussian fields). Speckle patterns were collected as a function of object position in the $x - y$ plane. (b) The normalized speckle correlation for the hidden circular patch is shown as a function of object translation $(\Delta x, \Delta y)$, along with central regions of actual speckle patterns taken at three positions along the y -direction (y_1, y_2, y_3). Using all camera pixels, pairs of normalized speckle patterns taken at different object positions such as $(0, y_1)$ and $(0, y_2)$, are used to compute cross-correlation coefficients with displacements of the object $(0, d_y)$. The cross-correlation coefficients having the same displacement are averaged, then interpolated in a 2D space for reconstruction.

geometries can be imaged in heavy scatter using phase retrieval, further demonstrating the practical utility of the approach.

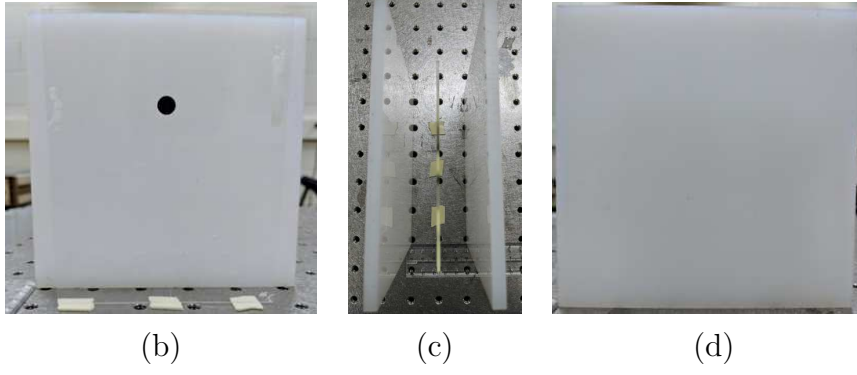


Fig. 3.2. (a) A photograph of a black 7.5 mm diameter patch in front of a scattering slab. Each slab is 6 mm thick with $\mu'_s = 4 \text{ cm}^{-1}$. (b) The two scattering slabs are separated by a distance of 5 cm. (c) The object cannot be seen through the slab.

Figures 3.1(a) and (b) illustrate our approach. Speckle intensity images taken at different object positions in between two scattering slabs constitute the dataset. The spatial scan steps are large relative to the wavelength and short-range correlations are neglected. Cross-correlation coefficients between pairs of speckle patterns are computed as a function of object displacement. Changes in the speckle pattern are due to motion of the object. The averaged and interpolated correlation coefficients, such as in Fig. 3.1(b), contain deterministic information about the object, which is useful for object reconstruction.

3.1 Theory

In the temporal frequency domain, the complex scalar field (detected through a polarizer) at detector position \mathbf{r}_d is written as $\Phi(\mathbf{r}_d; \mathbf{r}, \Delta\mathbf{r}) = \Phi_d(\mathbf{r}, \Delta\mathbf{r}) = \Phi_{db} + \Phi_{ds}(\mathbf{r}, \Delta\mathbf{r})$, where Φ_{db} is the background field without the object of interest and $\Phi_{ds}(\mathbf{r}, \Delta\mathbf{r})$ is the scattered field due to the object, with reference position \mathbf{r} and displacement $\Delta\mathbf{r}$. With the object at a reference position represented by a point

location \mathbf{r} and translated by a movement described by $\Delta\mathbf{r}$, we write the normalized average correlation of the scattered field at \mathbf{r}_d as

$$\begin{aligned}
g_{ss}^{(1)}(\mathbf{r}, \Delta\mathbf{r}) &= \langle \Phi_{ds}^*(\mathbf{r}) \Phi_{ds}(\mathbf{r} + \Delta\mathbf{r}) \rangle \langle I_{ds}(\mathbf{r}) \rangle^{-1/2} \langle I_{ds}(\mathbf{r} + \Delta\mathbf{r}) \rangle^{-1/2} \\
&= \langle \int d\mathbf{r}' O(\mathbf{r}; \mathbf{r}') \Phi(\mathbf{r}; \mathbf{r}') \mathcal{G}(\mathbf{r}_d, \mathbf{r}') \int d\mathbf{r}'' \\
&\quad \times O(\mathbf{r} + \Delta\mathbf{r}; \mathbf{r}'') \Phi(\mathbf{r} + \Delta\mathbf{r}; \mathbf{r}'') \mathcal{G}(\mathbf{r}_d, \mathbf{r}'') \rangle \\
&\quad \langle I_{ds}(\mathbf{r}) \rangle^{-1/2} \langle I_{ds}(\mathbf{r} + \Delta\mathbf{r}) \rangle^{-1/2}, \tag{3.1}
\end{aligned}$$

where $\langle \cdot \rangle$ indicates averaging over scatter configuration for a point detector at \mathbf{r}_d . In (3.1), $I_{ds} = |\Phi_{ds}|^2$, O describes the object contrast (regulating the scattered field from the moving object) with the reference object position \mathbf{r} , and \mathcal{G} is an unknown scalar Green's function accounting for the scattering medium (assumed to be representative for the wave equation describing all scatterers other than the object of interest, with a Dirac delta function source at \mathbf{r}' or \mathbf{r}''), relating the scattered field from the object of interest at the two positions (\mathbf{r} and $\mathbf{r} + \Delta\mathbf{r}$) to that at \mathbf{r}_d .

We write the intensity at \mathbf{r}_d with the object undergoing a variable translation $\Delta\mathbf{r}$ as $I(\mathbf{r}_d; \mathbf{r}, \Delta\mathbf{r}) = I_d$, where in the latter compact notation the argument dependency is implied, and use the normalized intensity $\tilde{I} = (I - \langle I \rangle) / \langle I \rangle$. Because a small spot is imaged by the camera (and the background scatter is significant), the intensity statistics within the speckle images are stationary. This allows us to use a pair of speckle images that correspond to given \mathbf{r} and $\Delta\mathbf{r}$ to form an estimate of the scatterer reconfiguration average $\langle \cdot \rangle$ for a point detector at \mathbf{r}_d . Our approach uses multiple pairs of speckle patterns sharing a given offset. Thus, with the appropriate normalizations, we obtain an improved estimate of the average by averaging over the multiple reference positions represented by different \mathbf{r} . Our approach results in cross-correlation images such as that in Fig. 3.1(b) for a circular patch object. From (3.1), this additional averaging step results in

$$\langle g_{ss}^{(1)}(\mathbf{r}, \Delta\mathbf{r}) \rangle = \bar{g}_{ss}^{(1)}(\Delta\mathbf{r}), \tag{3.2}$$

where only dependence on the displacement of the object is retained. Consequently, we write all subsequent physical quantities with $\langle \cdot \rangle$ as being dependent only on $\Delta\mathbf{r}$.

The average correlation of \tilde{I}_d over object scan position is

$$\langle \tilde{I}_d(\mathbf{r}) \tilde{I}_d(\mathbf{r} + \Delta\mathbf{r}) \rangle = \frac{|\langle \Phi_d^*(\mathbf{r}) \Phi_d(\mathbf{r} + \Delta\mathbf{r}) \rangle|^2}{\langle I_d(\mathbf{r}) \rangle \langle I_d(\mathbf{r} + \Delta\mathbf{r}) \rangle}, \quad (3.3)$$

where we have assumed the fields measured are zero-mean circular Gaussian [1] and hence can apply a theorem to write the fourth-order field moment in terms of the second order moments [16]. The numerator of (3.3) can be expanded as

$$\begin{aligned} & |\langle \Phi_d^*(\mathbf{r}) \Phi_d(\mathbf{r} + \Delta\mathbf{r}) \rangle|^2 \\ &= |\langle [\Phi_{db}^* + \Phi_{ds}^*(\mathbf{r})] [\Phi_{db} + \Phi_{ds}(\mathbf{r} + \Delta\mathbf{r})] \rangle|^2. \end{aligned} \quad (3.4)$$

Substituting (3.4) into (3.3) and with (3.1) and (3.2), we can write

$$\begin{aligned} & \langle \tilde{I}_d(\mathbf{r}) \tilde{I}_d(\mathbf{r} + \Delta\mathbf{r}) \rangle \\ &= C_0(\Delta\mathbf{r}) + \Re \{ C_1^*(\Delta\mathbf{r}) \bar{g}_{ss}^{(1)}(\Delta\mathbf{r}) \} + C_2(\Delta\mathbf{r}) |\bar{g}_{ss}^{(1)}(\Delta\mathbf{r})|^2, \end{aligned} \quad (3.5)$$

where $C_0(\Delta\mathbf{r})$, $C_1(\Delta\mathbf{r})$, and $C_2(\Delta\mathbf{r})$ are spatially-dependent coefficients obtained when grouping terms in the expansion by order of $\bar{g}_{ss}^{(1)}$. The cross correlation terms involving the unknown Φ_{db} and Φ_{ds} are retained in the expansion of (3.4), and the mean intensities in (3.3) are incorporated into C_0 and C_1 .

Referring to Fig. 3.1, macroscopic imaging requires that the scan distance be greater than the size of the object. From our experiments with various circular patches (3.5 - 7.5 mm diameter), with a sufficiently heavily scattering medium on either side, we find $\langle I_d(\mathbf{r} + \Delta\mathbf{r}) \rangle \simeq \langle I_d(\mathbf{r}) \rangle$. Therefore, C_0 , C_1 and C_2 can be approximated as constants over $\Delta\mathbf{r}$. Therefore, in this heavy scatter regime, (3.5) can be approximated as

$$\langle \tilde{I}_d(\mathbf{r}) \tilde{I}_d(\mathbf{r} + \Delta\mathbf{r}) \rangle = C_0 + \Re \{ C_1^* \bar{g}_{ss}^{(1)}(\Delta\mathbf{r}) \} + C_2 |\bar{g}_{ss}^{(1)}(\Delta\mathbf{r})|^2. \quad (3.6)$$

For an aperture-type object, where the aperture forms the source of detected intensity, $\langle I_{bd} \rangle = \langle \Phi_{db}^* \Phi_{db} \rangle = 0$, so $C_0 = 0$ and $C_1 = 0$. Also, by the definitions of the normalized intensity and normalized averaged scattered field correlation, $C_2 = 1$. We thus have

$$\langle \tilde{I}_d(\mathbf{r}) \tilde{I}_d(\mathbf{r} + \Delta\mathbf{r}) \rangle_{\text{ap}} = |\bar{g}_{ss}^{(1)}(\Delta\mathbf{r})|^2. \quad (3.7)$$

Our experimental data for circular absorptive patches of various sizes in a background bright field consistently indicated that $\langle \tilde{I}_d(\mathbf{r}) \tilde{I}_d(\mathbf{r} + \Delta\mathbf{r}) \rangle$ is quadratic in $|\bar{g}_{ss}^{(1)}|$. Using the known object function in these cases suggests that C_1 in (3.6) is sufficiently small to allow the second term to be neglected, giving

$$\langle \tilde{I}_d(\mathbf{r}) \tilde{I}_d(\mathbf{r} + \Delta\mathbf{r}) \rangle_{\text{pa}} = C_0 + C_2 |\bar{g}_{ss}^{(1)}(\Delta\mathbf{r})|^2. \quad (3.8)$$

The minimum of the measured intensity correlation not only indicates the value of C_0 but also reveals the size of the object, allowing us to remove the data points outside the joint spatial support. From (3.1) and (3.2), given that $|\Delta\mathbf{r}|$ is large compared to the wavelength, assuming heavily scattering environment so that we have Gaussian field statistics and only the joint spatial support of the object and the translated object contributes to the average second-order field moment, we have

$$\bar{g}_{ss}^{(1)}(\Delta\mathbf{r}) = \int d\mathbf{r} \tilde{O}^*(\mathbf{r}) \tilde{O}(\mathbf{r} + \Delta\mathbf{r}), \quad (3.9)$$

where \tilde{O} is the object function from (3.1) normalized so that $\int d\mathbf{r} \tilde{O}^*(\mathbf{r}) \tilde{O}(\mathbf{r}) = 1$. From (3.7), and upon subtracting C_0 from (3.8) and rescaling, we can write

$$\langle \tilde{I}_d(\mathbf{r}) \tilde{I}_d(\mathbf{r} + \Delta\mathbf{r}) \rangle = |\bar{g}_{ss}^{(1)}(\Delta\mathbf{r})|^2 = \left| \mathcal{F}^{-1} \left\{ |\tilde{O}(\mathbf{k})|^2 \right\} \right|^2, \quad (3.10)$$

where in the second equality we use the Wiener-Khinchin theorem. With $\bar{g}_{ss}^{(1)}(\Delta\mathbf{r}) = \mathcal{F}^{-1} \left\{ |\tilde{O}(\mathbf{k})|^2 \right\}$, we recognize that $\bar{g}_{ss}^{(1)}$ can be a complex quantity. For our experiments, the continuous nature of the intensity correlation data and the positive and symmetric properties of $|\tilde{O}(\mathbf{k})|^2$ for a real object function indicate that $\bar{g}_{ss}^{(1)}$ is continuous, positive and symmetric. Hence, we can directly obtain $|\tilde{O}(\mathbf{k})|$ and subsequently carry out iterative phase retrieval [51] to reconstruct the embedded object.

3.2 Experiments

We designed three experiments with different objects and scattering materials that used the setup shown in Fig. 3.1(a). A 59-mW 850-nm laser diode with a linewidth

less than 10 MHz was used for illumination. The beam diameter at the scattering material was approximately 0.4 mm. As shown in Figs. 3.2(a)-(c), we used two layers of scattering material separated by a small distance (about 5 cm) and a pair of stages to move the objects of interest in the transverse plane between the layers. An area of approximately 1.8 mm by 1.8 mm on the back of the second scattering layer was imaged by the camera through a polarizer (to obtain Gaussian field statistics) using magnifying optics. A PRIME sCMOS (for "LUX", 500 ms integration time, and for the circular patch, 300 ms) and a CoolSNAP HQ CCD (for " π " with 3 s integration time) were used in the experiment. The intensity statistics of the speckle patterns used were measured to be negative exponential, indicating Gaussian field statistics.

Figure 3.3(a) shows a 7.5-mm-diameter circular absorbing patch object that was placed on a transparent plastic window (10 cm \times 13 cm). This object was translated along the y -axis, referring to Fig. 3.1(a), between two 6-mm-thick acrylic scattering slabs. The scattering slabs (14 cm \times 14 cm) were made of commercial acrylic with negligible optical absorption, embedded with TiO_2 scatterers having a mean diameter of 50 nm. The reduced scattering coefficient ($\mu'_s = 4 \text{ cm}^{-1}$) of the scattering acrylic slabs is comparable to that of human breast tissue *in vivo* [52]. This is the scattering material shown in Figs. 3.2(a)-(c), and the very heavy scatter is evident. As Fig. 3.2(c) illustrates, it is not possible to see the small circular patch behind a 6 mm thick acrylic scattering slab. The background intensity and the object scatter are both significant in this situation. The object was moved in a 1D uniformly-spaced scan of 40 points over 13.16 mm. Averaged intensity correlations were computed using the 40 speckle patterns obtained at these object locations. We extracted C_0 in (3.8) from the minimum of the measured intensity correlation, along with the renormalizing constant C_2 . In Fig. 3.3(b), we compare the speckle intensity correlation over object position with a prediction using (3.8). Note the excellent agreement. The measured correlation increases after the minimum because the speckle patterns become similar to the bright background when the object is displaced farthest away from the center. To reconstruct the circular patch object, we discarded measured data points for $\Delta \mathbf{r} >$

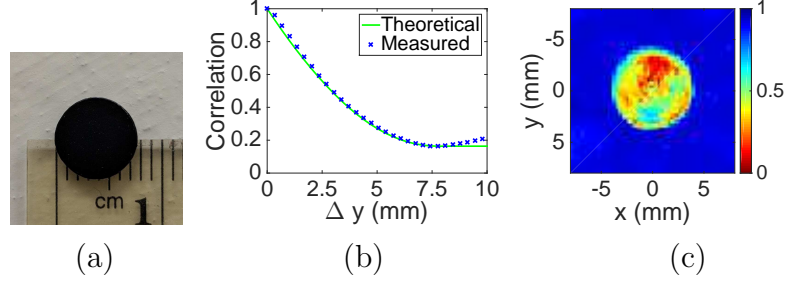


Fig. 3.3. (a) Photograph of a circular black vinyl patch object having a diameter of 7.5 mm that was hidden between two 6 mm-thick acrylic scattering slabs having $\mu'_s = 4 \text{ cm}^{-1}$. (b) Measured (blue) and simulated (green, using (3.8)) normalized intensity speckle correlations, with data collected in the experiment described by Fig. 3.1. (c) The reconstructed image of the circular patch, showing a geometry true to the object size.

7.5 mm, beyond the minimum of the measured intensity correlation and the joint spatial support, and took advantage of rotational symmetry, using the 1D data to form a 2D map. Inversion of (3.10) was achieved using iterative phase retrieval to form the object function [53]. Specifically, 2000 iterations of the hybrid input-output method with a varying spatial frequency filter implemented outside the support area was used to obtain Fig. 3.3(c) [51], which is true to the object size. The inversion procedure conforms to a well-defined phase retrieval problem where the spatial support can be determined by the global minimum of the decorrelation data. We used a loose support about $15 \text{ mm} \times 15 \text{ mm}$. The near-perfect prediction of the correlation suggests that imperfect smoothing at $\Delta \mathbf{r} = 7.5 \text{ mm}$ and a local minimum may be responsible to the noise in phase reconstructing the symmetric object in Fig. 3.3(c).

We describe two experiments and demonstrate the reconstruction of small and complex apertures in Fig. 3.4. In the experiment to image the character "π", we used fresh chicken breast that was 2 mm thick on the source side and 7 mm on the detector side, held between two microscope slides. For the "LUX" aperture, 3-mm and 9-mm-thick acrylic scattering slabs ($\mu'_s = 4 \text{ cm}^{-1}$) were used on the source and detector side, respectively. The two aperture objects were fabricated as reflective metal coatings on rectangular glass substrates, forming the apertures "LUX" and

" π " shown in Figs. 3.4(a) and (d). The apertures were scanned over 20 diagonal lines having a uniform angular increment ($\pi/10$) within a circular region. Each line scan had a length at least 1.5 times the maximum spatial support of the object. Cross-correlation coefficients of speckle images that share the same displacement are averaged if the speckle images involved are acquired on the same line scan. This data was interpolated onto a square 2D Cartesian grid using the *gridfit* function in MATLABTM. The central regions of the interpolated correlations are shown in Figs. 3.4(b) and (e) for the "LUX" and " π " objects, respectively. Note that the correlations approach a minimum when $\Delta\mathbf{r}$ is about the object's size, consistent with the picture of the joint support of the object contributing to the measured correlations. This provides a convenient way to select the data set used in reconstruction, and we did so using a threshold (about 0.05 of the maximum). A Cartesian 2D-tapered cosine (Tukey) window (twice the object's size, selected by $\alpha N/2$, with $\alpha = 0.45$ and N the number of samples along a given dimension), was applied to the data. The filtered data set was zero-padded to four times the object's size before the inversion of (3.10). The reconstructed images are shown in Figs. 3.4(c) and (f). Notice that the "LUX" and " π " can be clearly identified despite being completely hidden inside the equivalent of 9 mm of tissue ("LUX") and 7 mm of chicken breast (" π ").

The reconstruction quality is inevitably affected by instability associated with data acquisition: variations in temperature, illumination, and sample mechanical stability all play a role. We, therefore, expect that the reconstruction quality will be improved by a larger dataset with higher scanning precision, although a larger data set may require faster acquisition to derive full benefit. However, the matching of theoretical and measured intensity correlations, and our investigation of the reconstruction process, suggest that the primary contributor to reconstructed image artifacts is the influence of the spatial windowing of the intensity correlation raw data before the Fourier transform. We thus expect the reconstruction to be improved by employing a windowing method that is based on the minima of the speckle decorrelation (in a 2D space in our case).

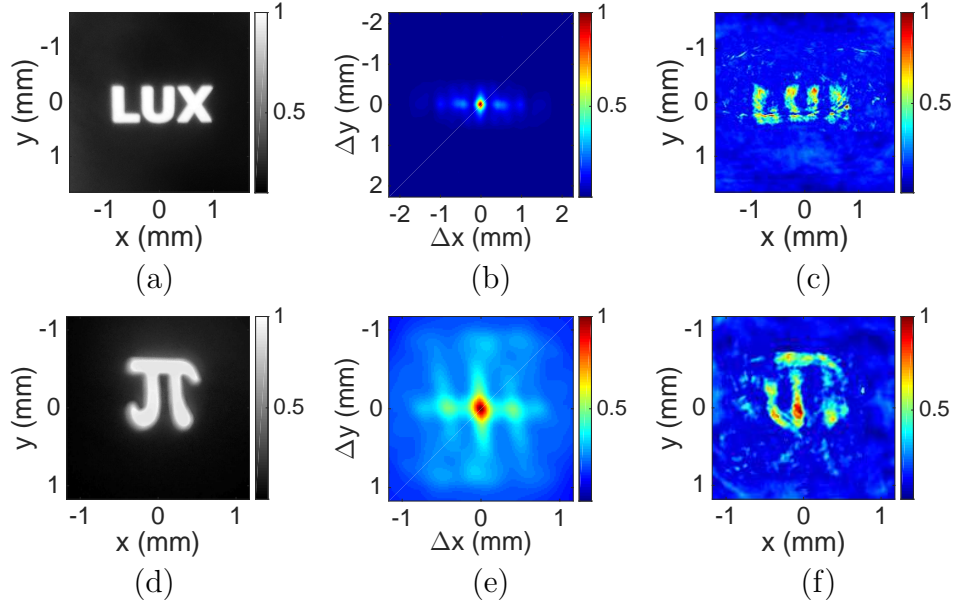


Fig. 3.4. Aperture objects reconstructed from speckle intensity correlations over object position. (a) Photograph of the "LUX" object. (b) Interpolated measured speckle intensity correlation for the LUX object between 3-(source side) and 9-mm (detector side) scattering acrylic slabs ($\mu'_s = 4 \text{ cm}^{-1}$). (c) Reconstructed image for the "LUX" object. (d) Photograph of the " π " object. (e) Interpolated measured intensity correlation for the " π " aperture located between two fresh chicken breast slices, 2 mm thick on the source side and 7 mm thick on the detector side. (f) Reconstructed image for the " π " object.

3.3 Conclusion

The experimental results presented represent special cases of the broader imaging domain where absorption/scatter representing the object are obtained. Of particular note, we have presented a means to image an object in a coherent bright-field regime that is representative of many applications, and the approach applies to thick and very heavily scattering media and is simplified by operating in this regime. This is distinctly different from recent applications of the memory effect, where fluorescence was used [14], which requires a thin scattering medium, and a windowed autocorrelation of speckle image was used, representing a small range of angles [14]. We also note that a generalization for more weakly scattering media can be implemented, where the approximation of the mean intensities in (3.3) as constants is relaxed. The resolution limit is beyond one wavelength, because the short-length correlations have been neglected. However, the resolution is practically limited by the quality of the measurement data and the robustness of the reconstruction approach. While we have neglected short-range correlation, evidence suggests speckle cross-correlation data over object position is sensitive to the microstructure [20].

We have demonstrated that speckle intensity correlations as a function of object position can be used to coherently image arbitrary objects (patches and apertures of various sizes and shapes) moving inside heavily scattering media at a resolution commensurate with the object size. Only the position change of the object is needed. This can be estimated using velocity with established methods. For example, by making measurements as a function of time, one can determine velocity information from either temporal decorrelation or the Doppler shift [54]. Moreover, localization based on the diffusion model [55] can be performed using the mean intensity to estimate the positions of the hidden moving object, including with fluorescence. In the situation we considered, the time frame for the object of interest to move by its dimension needs to be small compared to its rotation and the movement of the environment, or these effects need to be calibrated. Blood cells and labeled biomolecules in capillaries

could satisfy our requirements, where the local velocity is approximately linear and the cell, for example, needs to move a distance equal to its dimension, about $10\text{ }\mu\text{m}$. Our method suggests the possibility to identify and even image circulating melanoma cells [56]. Movement could also be induced by an acoustic wave in tissue to produce controlled motion, and motion of tens of microns has been achieved [57]. Other possible applications include detecting and imaging fast-moving objects through clouds, fog, or other obscuring environments. More generally, spatial speckle correlations allow new sensing, imaging, and communication opportunities in scenarios in which traditional methods are not feasible.

4. SPECKLE INTENSITY CORRELATIONS OVER OBJECT POSITION FOR SENSING AND IMAGING IN A HEAVILY SCATTERING MEDIUM

4.1 Introduction

Coherent optical sensing and imaging methods are desirable because they offer high spatial resolution as well as spectroscopic information. When coherent light interacts with random scattering structures inherent in a myriad of applications, the resultant constructive and destructive interference between the wavefronts of the differently scattered fields forms speckle. While speckle intensity patterns appear random, statistical information can be accessed through correlations over appropriate variables. The intensity interferometer pioneered by Hanbury Brown and Twiss used correlated intensity measurements with two detectors to access an object's spatial frequency spectrum [7, 8]. The underlying principle can be extended to intensity measurements through a 2D detector array where the autocorrelation of an intensity pattern is related to the spatial spectrum of a diffuse object under coherent illumination [10] (in accordance to the van Cittert-Zernike theorem [9]) and the recovery of an illumination pattern through a diffuse surface becomes possible [11]. A correlation over laser frequency can be used to image hidden inhomogeneities [4] and to characterize the scattering medium [58]. The memory effect preserves information of the incident wavefront within a limited range of incident angles [12], and this enabled a series of recent imaging experiments through a physically thin medium [14, 15, 59]. Directly mapping and inverting the transmission matrix [47, 60] and optimizing the incident wavefront [29] have also allowed focusing inside a scattering medium, which can be used for other imaging modalities such as two-photon microscopy [61]. Recently, focusing methods that use the phase conjugate of the field from an embedded

guidestar have become prominent [48]. Notably, field perturbation from a moving object can be used as the guidestar [62, 63]. Another widely utilized application of speckle measurements is speckle contrast imaging [64], and near-surface blood flow images have been obtained [65] by tracking changes in the local temporal speckle contrast ratio. Some of the aforementioned studies have demonstrated focusing or imaging through an amount of scatter typically on the order of one millimeter of biological tissue [15, 62, 63, 65]. When a change in the speckle pattern is only due to the movement of a strongly-interacting object hidden inside a scattering medium, imaging of the object is possible, and an approach suitable for imaging apertures has been presented [20]. Recent results suggest that it may be possible to develop this concept into a general method [21]. However, to date there has not been a general theory nor an evaluation of the relevant parameters.

We present a theory for imaging a moving object in a heavily scattering background and support development this with an experimental study with varying object and background scattering properties. The theory for the speckle intensity correlations over object position is introduced with a practical emphasis necessary for its application to sensing and imaging situations with heavy background scatter. By interpreting the detected field as a superposition of the background scattering field without the moving object and the scattered field due to the object, the spatial intensity correlation can be written in terms of the cross- and auto-correlations of the background and the scattered fields, applicable due to the Gaussian field statistics. With experimental evidence, we show that by grouping terms by the order of power of the scattered field autocorrelation, one can access the object autocorrelation function. It is also shown that the parameters obtained from intensity correlations can also be used to compare the scattering strengths of the object and its surrounding environment, useful for sensing.

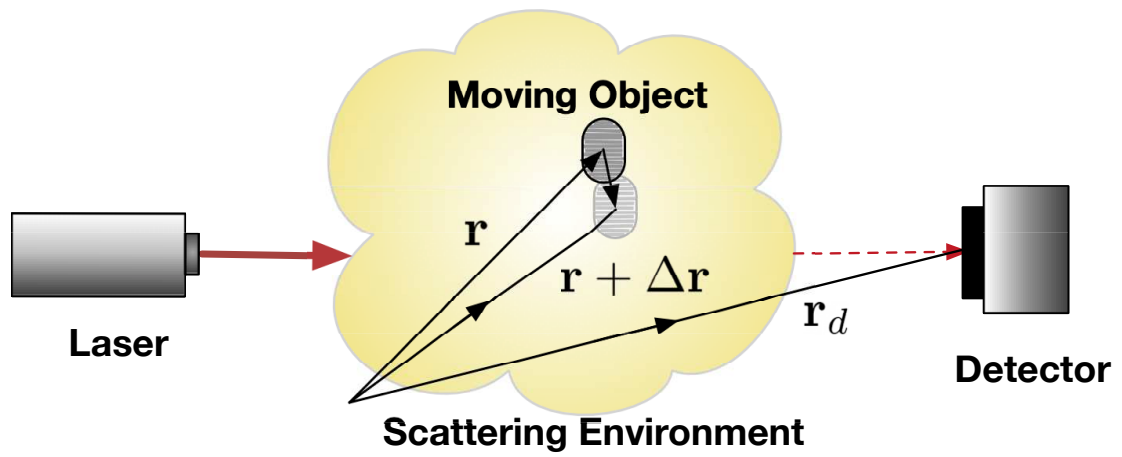


Fig. 4.1. Concept figure for imaging and sensing a moving object in a scattering environment.

4.2 Theory

With reference to Fig. 4.1, the moving object of interest is in a randomly scattering medium that is illuminated by a coherent source. We write the detected field at \mathbf{r}_d measured through a polarizer as Φ_d . As Fig. 4.1 illustrates, $\Delta\mathbf{r}$ is the object displacement from a reference position \mathbf{r} . The second order averaged field correlation over translated position is $\langle\Phi_d^*(\mathbf{r})\Phi_d(\mathbf{r} + \Delta\mathbf{r})\rangle$, where $\langle\cdot\rangle$ is mathematically an average over background scatterer reconfiguration and experimentally an average formed over stationary speckle intensity data captured by a camera. We write Φ_d as the superposition of the scattered field due to the object of interest, Φ_{ds} , and the background speckle field without the object, Φ_{db} , so that $\Phi_d = \Phi_{db} + \Phi_{ds}$. It is noted that Φ_{db} does not change with the object position, and if the object inside the scattering environment is the only source of detected signal, $\Phi_d = \Phi_{ds}$, simplifying the situation. The second-order field correlation can be expanded and written in terms of the background and the scattered intensities ($I_{db} = |\Phi_{db}|^2$ and $I_{ds} = |\Phi_{ds}|^2$, assuming impedance scaling) and the averaged normalized field correlations ($g_{bs}^{(1)}$, $g_{sb}^{(1)}$ and $g_{ss}^{(1)}$, where the s subscript indicates scattered field and b subscript indicates background field), as

$$\begin{aligned} \langle\Phi_d^*(\mathbf{r})\Phi_d(\mathbf{r} + \Delta\mathbf{r})\rangle &= \langle I_{db} \rangle \\ &+ \langle I_{db} \rangle^{1/2} \langle I_{ds}(\mathbf{r} + \Delta\mathbf{r}) \rangle^{1/2} g_{bs}^{(1)}(\Delta\mathbf{r}) \\ &+ \langle I_{ds}(\mathbf{r}) \rangle^{1/2} \langle I_{db} \rangle^{1/2} g_{bs}^{*(1)}(0) \\ &+ \langle I_{ds}(\mathbf{r}) \rangle^{1/2} \langle I_{ds}(\mathbf{r} + \Delta\mathbf{r}) \rangle^{1/2} g_{ss}^{(1)}(\Delta\mathbf{r}). \end{aligned} \quad (4.1)$$

In writing (4.1), we have used the compact notation $g_{sb}^{(1)}(\mathbf{r}, 0) = g_{sb}^{(1)}(0) = g_{bs}^{(1)*}(0)$, $g_{bs}^{(1)}(\mathbf{r}, \mathbf{r} + \Delta\mathbf{r}) = g_{bs}^{(1)}(\Delta\mathbf{r})$, and $g_{ss}^{(1)}(\mathbf{r}, \mathbf{r} + \Delta\mathbf{r}) = g_{ss}^{(1)}(\Delta\mathbf{r})$, where the correlations do not depend on the reference position \mathbf{r} after normalization by the averaged intensities. The normalized field correlation $g_{ss}^{(1)}(\Delta\mathbf{r})$ can be written in terms of the Green's function representation of Φ_{ds} using an object function that describes the object contrast [21]. Given that $|\Delta\mathbf{r}|$ is large compared to the wavelength and assuming

adequate random background scatter, so that only the joint spatial support of the object and the translated object contributes to $g_{ss}^{(1)}$, we can write

$$\begin{aligned} g_{ss}^{(1)}(\Delta\mathbf{r}) &= \frac{\langle \Phi_{ds}^*(\mathbf{r})\Phi_{ds}(\mathbf{r} + \Delta\mathbf{r}) \rangle}{\langle I_{ds}(\mathbf{r}) \rangle^{1/2} \langle I_{ds}(\mathbf{r} + \Delta\mathbf{r}) \rangle^{1/2}} \\ &= \int d\mathbf{r}' \tilde{O}^*(\mathbf{r}') \tilde{O}(\mathbf{r}' + \Delta\mathbf{r}), \end{aligned} \quad (4.2)$$

where \tilde{O} is the normalized object function, so that $\int d\mathbf{r}' \tilde{O}^*(\mathbf{r}') \tilde{O}(\mathbf{r}' + \Delta\mathbf{r}) = 1$ for $\Delta\mathbf{r} = 0$.

The detected intensity at the detector as a function of the position of a displaced object is $I_d = |\Phi_d|^2$. The normalized intensity pattern is computed by $\tilde{I}_d = (I_d - \langle I_d \rangle) / \langle I_d \rangle$, where $\langle I_d \rangle$ is the mean intensity of a speckle pattern. Assuming zero-mean circular Gaussian polarized field statistics as the result of heavy scatter, the normalized intensity correlation over object position averaged over scatterer re-configurations can be expressed using a moment theorem [16] as

$$\langle \tilde{I}_d(0) \tilde{I}_d(\Delta\mathbf{r}) \rangle \equiv \langle \tilde{I}_d(\mathbf{r}) \tilde{I}_d(\mathbf{r} + \Delta\mathbf{r}) \rangle = \frac{|\langle \Phi_d^*(\mathbf{r}) \Phi_d(\mathbf{r} + \Delta\mathbf{r}) \rangle|^2}{\langle I_d(\mathbf{r}) \rangle \langle I_d(\mathbf{r} + \Delta\mathbf{r}) \rangle}, \quad (4.3)$$

where scaling by the means results in a correlation that is independent of \mathbf{r} . Using (4.1), we expand the numerator of (4.3) as

$$|\langle \Phi_d^*(\mathbf{r}) \Phi_d(\mathbf{r} + \Delta\mathbf{r}) \rangle|^2 = D_0(\mathbf{r}, \Delta\mathbf{r}) + 2\Re \{ D_1^*(\mathbf{r}, \Delta\mathbf{r}) g_{ss}^{(1)}(\Delta\mathbf{r}) \} + D_2(\mathbf{r}, \Delta\mathbf{r}) |g_{ss}^{(1)}(\Delta\mathbf{r})|^2 \quad (4.4)$$

where D_0 , D_1 and D_2 are

$$\begin{aligned} D_0(\mathbf{r}, \Delta\mathbf{r}) &= \langle I_{db} \rangle^2 + \langle I_{db} \rangle^{3/2} \langle I_{ds}(\mathbf{r}) \rangle^{1/2} 2\Re \{ g_{bs}^{(1)}(0) \} \\ &\quad + \langle I_{db} \rangle^{3/2} \langle I_{ds}(\mathbf{r} + \Delta\mathbf{r}) \rangle^{1/2} 2\Re \{ g_{bs}^{(1)}(\Delta\mathbf{r}) \} \\ &\quad + \langle I_{db} \rangle \langle I_{ds}(\mathbf{r}) \rangle^{1/2} \langle I_{ds}(\mathbf{r} + \Delta\mathbf{r}) \rangle^{1/2} 2\Re \{ g_{bs}^{(1)}(0) g_{bs}^{(1)}(\Delta\mathbf{r}) \} \\ &\quad + \langle I_{db} \rangle \langle I_{ds}(\mathbf{r}) \rangle |g_{bs}^{(1)}(0)|^2 + \langle I_{db} \rangle \langle I_{ds}(\mathbf{r} + \Delta\mathbf{r}) \rangle |g_{bs}^{(1)}(\Delta\mathbf{r})|^2, \end{aligned} \quad (4.5)$$

$$\begin{aligned} \Re \{ D_1(\mathbf{r}, \Delta\mathbf{r}) \} &= \langle I_{db} \rangle \langle I_{ds}(\mathbf{r}) \rangle^{1/2} \langle I_{ds}(\mathbf{r} + \Delta\mathbf{r}) \rangle^{1/2} \\ &\quad + \langle I_{db} \rangle^{1/2} \langle I_{ds}(\mathbf{r}) \rangle \langle I_{ds}(\mathbf{r} + \Delta\mathbf{r}) \rangle^{1/2} \Re \{ g_{bs}^{(1)}(0) \} \\ &\quad + \langle I_{db} \rangle^{1/2} \langle I_{ds}(\mathbf{r}) \rangle^{1/2} \langle I_{ds}(\mathbf{r} + \Delta\mathbf{r}) \rangle \Re \{ g_{bs}^{(1)}(\Delta\mathbf{r}) \}, \end{aligned} \quad (4.6)$$

$$\begin{aligned} \Im\{D_1(\mathbf{r}, \Delta\mathbf{r})\} &= \langle I_{db} \rangle^{1/2} \langle I_{ds}(\mathbf{r}) \rangle^{1/2} \langle I_{ds}(\mathbf{r} + \Delta\mathbf{r}) \rangle \Im\{g_{bs}^{(1)}(\Delta\mathbf{r})\} \\ &\quad - \langle I_{db} \rangle^{1/2} \langle I_{ds}(\mathbf{r}) \rangle \langle I_{ds}(\mathbf{r} + \Delta\mathbf{r}) \rangle^{1/2} \Im\{g_{bs}^{(1)}(0)\}, \end{aligned} \quad (4.7)$$

$$D_2(\mathbf{r}, \Delta\mathbf{r}) = \langle I_{ds}(\mathbf{r}) \rangle \langle I_{ds}(\mathbf{r} + \Delta\mathbf{r}) \rangle. \quad (4.8)$$

Note that D_0 , D_1 and D_2 contain terms that are not directly obtainable from speckle measurements, for example, I_{ds} and $g_{bs}^{(1)}$. By definition, I_{db} and I_{ds} are non-negative quantities and $g_{bs}^{(1)}$ has a magnitude that is no larger than unity. We can rewrite (4.1) for $\Delta\mathbf{r} = 0$ as

$$\langle I_d \rangle = \langle I_{db} \rangle + \langle I_{ds} \rangle + \langle I_{db} \rangle^{1/2} \langle I_{ds} \rangle^{1/2} 2\Re\{g_{bs}^{(1)}(0)\}. \quad (4.9)$$

From (4.9), we can infer that $g_{bs}^{(1)}(0)$ must exist and it must have a negative real part for an object of interest that is absorbing or occluding speckle background because $\langle I_{db} \rangle$ should always be larger than $\langle I_d \rangle$. Under the assumption of heavy background scatter, we expect that $\langle I_{ds} \rangle$ is slowly varying for $|\Delta\mathbf{r}| \leq d$, where d represents the size of the object. As the result, $\langle I_{ds}(\mathbf{r}) \rangle \approx \langle I_{ds}(\mathbf{r} + \Delta\mathbf{r}) \rangle$. With this insight, we approximate D_0 , D_1 and D_2 as constants in the range $|\Delta\mathbf{r}| \leq d$. Also, from (4.5), we can compare the magnitudes and the signs of the terms to infer that D_0 should be non-negative for both the cases of a large and a small $\langle I_{ds} \rangle$. From (4.6) and (4.7), assuming that the object is large compared to the wavelength and not weakly scattering so that $\langle I_{ds} \rangle$ and $\langle I_{db} \rangle$ are about the same magnitude of order, then D_1 is small when compared to D_0 and D_2 due to the opposite signs and the similar magnitude of the constituting terms. Hence, (4.3) can be rewritten as

$$\langle \tilde{I}_d(0) \tilde{I}_d(\Delta\mathbf{r}) \rangle \simeq \frac{D_0 + 2\Re\{D_1^* g_{ss}^{(1)}(\Delta\mathbf{r})\} + D_2 |g_{ss}^{(1)}(\Delta\mathbf{r})|^2}{\langle I_d(\mathbf{r}) \rangle \langle I_d(\mathbf{r} + \Delta\mathbf{r}) \rangle}. \quad (4.10)$$

where the average of the normalized speckle intensity correlation over object position is expressed by unknown terms that are grouped and approximated as constants (D_0 , D_1 and D_2), the directly measurable averaged detected intensity ($\langle I_d(\mathbf{r}) \rangle$ and

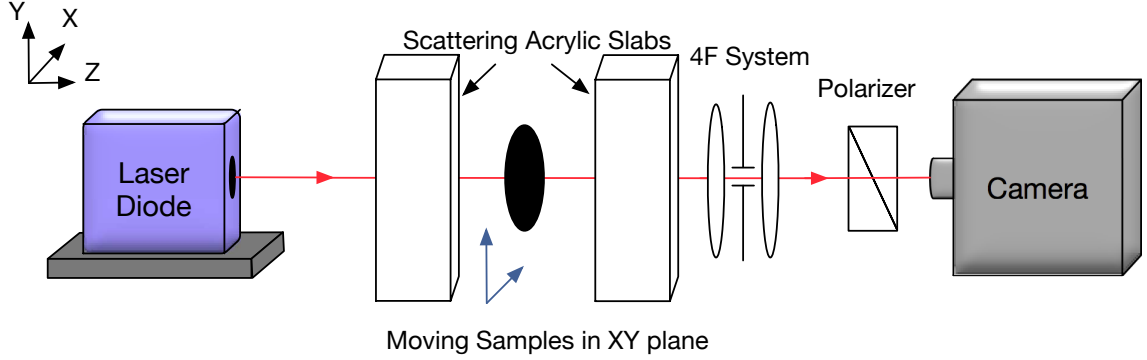


Fig. 4.2. The experimental setup for measuring the speckle intensity correlation of a moving circular patch translated along the y-axis between two scattering layers. Speckle patterns are collected at the camera after passing through a spatial filter and a polarizer.

$\langle I_d(\mathbf{r} + \Delta\mathbf{r}) \rangle$, and the normalized scattered field correlation that contains object function $(g_{ss}^{(1)}(\Delta\mathbf{r}))$.

4.3 Experiments

Our experimental setup is shown in Fig. 4.2. A 59 mW 850 nm laser diode with a linewidth less than 10 MHz was used for illumination. We used two layers of the scattering material separated by a small distance (about 5 cm) and a pair of stages to move the objects of interest in the transverse plane between the layers. A 4f system is used to filter the resultant speckle patterns, so that speckle spots incident on the camera are bigger than a single pixel and a polarizer is used for detecting circular Gaussian scalar field statistics. An area of approximately 1.8 mm by 1.8 mm on the back of the second scattering layer was imaged by the camera using magnifying optics. The speckle images have stationary statistics that are used to form averages. Also, to improve the estimates, multiple intensity correlation coefficients that correspond to the same $\Delta\mathbf{r}$ but different \mathbf{r} are averaged to form an estimation of the ensemble average over many scatterer reconfigurations.

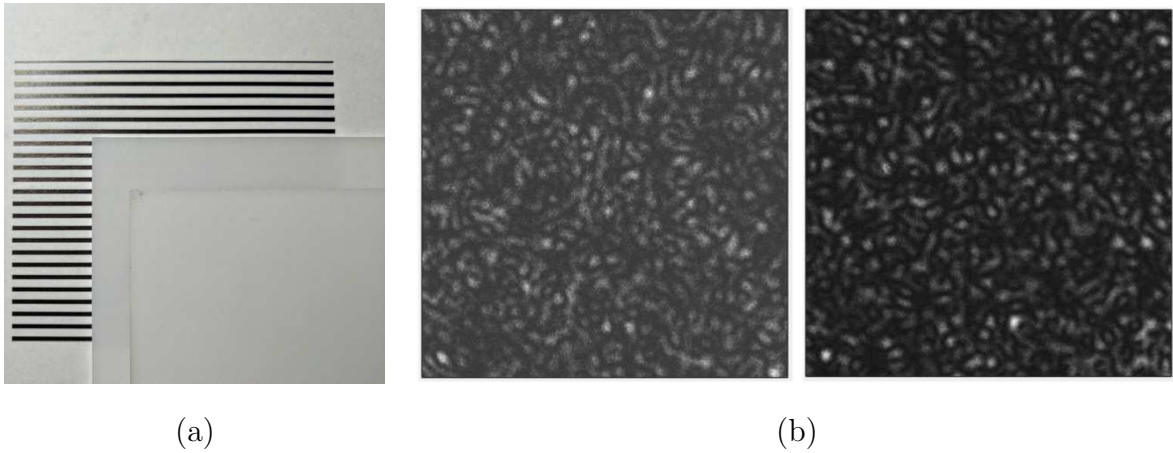


Fig. 4.3. Example heavily scattering material used in our experiments. (a) Two 6 mm, $\mu'_s = 4\text{cm}^{-1}$ slabs of acrylic are placed on top of a page with printed stripes. Through one 6 mm thick slab, one can no longer distinguish individual stripes, and through a total of 12 mm, it is not possible to distinguish the striped area. (b) The centrally cropped speckle patterns for a moving 4 mm circular patch placed between a 4-ground-glass stack and a 6-ground-glass stack are highly-decorrelated over an object displacement of about 2.5 mm.

In our experiments, ground glass diffusers and acrylic slabs (shown in Fig. 4.3(a)) are used as the scattering environment. The acrylic slabs contain TiO_2 scatterers that have a mean diameter of 50 nm, with a reduced scattering coefficient estimated to be 4 cm^{-1} , with negligible absorption at the wavelength used. Stacks of ground glass diffusers provide heavy scatter, evident in Fig. 4.3(b) as the measured speckle patterns become highly-decorrelated over object displacement. The moving objects used are circular patches of different diameters (3.7 mm, 5 mm, and 6 mm). These objects were formed with adhesive black tape attached to transparent plastic windows ($10 \text{ cm} \times 13 \text{ cm} \times 0.15 \text{ cm}$), making for a binary object (either complete absorptive or complete transparent). Five different scattering layers were used: 3 mm and 6 mm thick acrylic slabs ($14 \text{ cm} \times 14 \text{ cm}$), a stack of four ground glass diffusers, a stack of six ground glass diffusers (individual ground glass is of $10 \text{ cm} \times 10 \text{ cm} \times 0.2 \text{ cm}$, stacks are taped together at the edges) as well as a single ground glass of 1500 grit. Specifically, the four-piece stack consists of two 120-grit and two 1500-grit ground glasses and the six-piece stack consists of two 120-grit and four 1500-grit ground glasses.

Our experiments with black circular patches of various sizes (with diameters of 3.7 mm to 7.5 mm) and the scattering acrylic slabs used consistently verified that D_1 is negligibly small, so that (4.10) becomes

$$\langle \tilde{I}_d(0) \tilde{I}_d(\Delta \mathbf{r}) \rangle \simeq \frac{D_0 + D_2 \left| g_{ss}^{(1)}(\Delta \mathbf{r}) \right|^2}{\langle I_d(\mathbf{r}) \rangle \langle I_d(\mathbf{r} + \Delta \mathbf{r}) \rangle}. \quad (4.11)$$

We focus on (4.11) and the impact of how differently scattering object and varying degrees of background scatter impact the normalized intensity correlation over object motion, specifically, the validity of (4.11) and how D_0 and D_2 relate to various situations. The results are shown in Figs. 4.4 and 4.5, where intensity correlations are normalized according to (4.11) and then rescaled to show the variation of $\left| g_{ss}^{(1)}(\Delta \mathbf{r}) \right|^2$.

Figure 4.4(a) shows the measured normalized speckle correlations for varying object (patch) size and hence scattering strength, and fixed scatter on the laser and detector sides. A four-piece stack of ground glass diffusers was used on the laser side

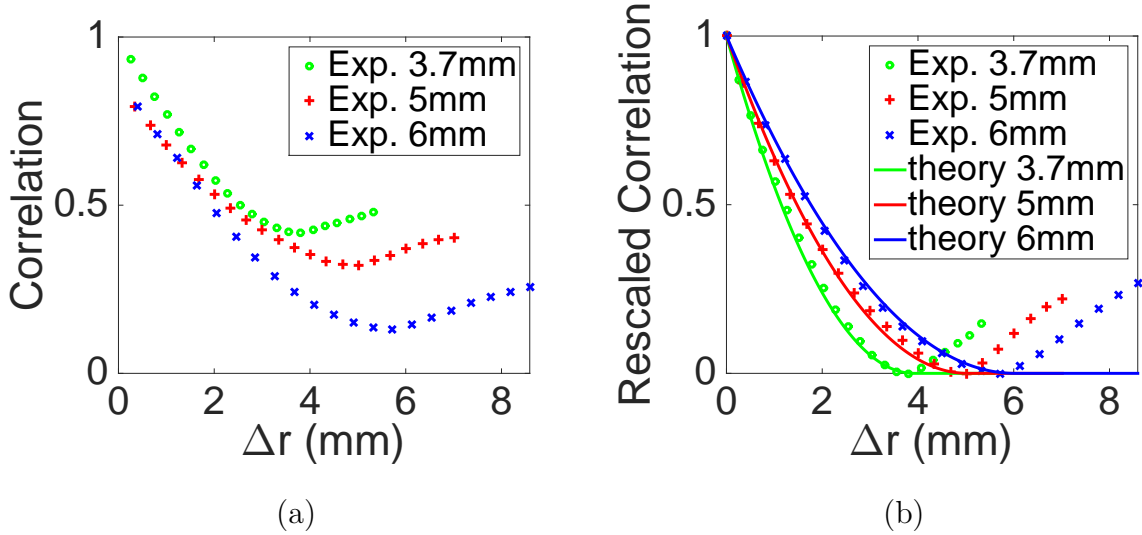


Fig. 4.4. Intensity correlations over object position with various patch size, and hence, varying degree of object scatter. (a) Keeping the same slab configuration (a four-piece ground glass diffuser at the laser side and a 6 mm thick $\mu'_s = 4 \text{ cm}^{-1}$ acrylic slab at the detector side), the measured intensity correlations are shown for circular patches having diameters of 3.7, 5, and 6 mm. The larger the size of the object, the deeper the decorrelation dip. (b) The scaled decorrelation of each circular patch ($|g_{ss}^{(1)}(\Delta \mathbf{r})|^2$) in (4.11)) agrees well with our prediction using (4.2) for $\Delta \mathbf{r}$ smaller than the object's size. The measured correlation increases after the minimum because the speckle patterns become similar to the bright background as the object is displaced away from the center.

and a 6 mm thick acrylic slab on the detector side. The motivation for using the glass diffuser stack on the laser side was to remove decorrelations due to heating, as might occur with the acrylic scattering slabs. As Fig. 4.4(a) indicates, the correlations decrease from unity, reach a minimum, and then increase (ultimately to close to one again). The larger the object the greater the dip in the intensity correlation. This can be understood as the increasing patch size producing larger $\langle I_{ds} \rangle$, and from (4.5) and (4.8), D_2 becomes more dominant in (4.11) relative to D_0 . The minima in the correlations occur at the diameters of each circular patch and this feature provides that information. Computing the numerator of the right hand side of (4.11) from measured data, subtracting D_0 and normalizing so that $D_2 = 1$, we find the data shown in Fig. 4.4(b). Also plotted are solid lines corresponding to $\left| g_{ss}^{(1)}(\Delta \mathbf{r}) \right|^2$ for $|\Delta \mathbf{r}| \leq d$ according to (4.2), obtained from the normalized object function autocorrelation. Note the excellent agreement between the theory and experiment in all cases. For all data we present, the (wavelength scale) short-range intensity correlation has been neglected (see, for example, previous results for this regime [20]) and the macroscopic measurement data has been extrapolated to $\Delta \mathbf{r} = 0$ for normalization. The measured correlations increase after their minima because the speckle patterns become similar to the bright background as the object is displaced distances large relative to the object's size. We note that Fig. 4.4(a) indicates that $\langle I_{ds} \rangle / \langle I_{db} \rangle$ increases with patch size and hence object scattering strength. This is reflected in the increase of D_2/D_0 with increasing patch size.

Figure 4.5 shows experimental intensity correlation results for a fixed patch size (3.7 mm diameter) and varying levels of scatter on the detector side (Figs. 4.5(a) and (c)) and the laser side (Figs. 4.5(b) and (d)). For the results shown in Fig. 4.5(a), the scattering layer on the laser side was fixed (the four-piece glass diffuser stack) while the scattering layer at the detector side was varied (the six-piece diffuser stack, the 3 mm acrylic slab, and the 6 mm acrylic slab, in order of increasing scatter). Increasing the amount of scatter on the detector side increases the spatial spread of the speckle pattern exiting the scattering medium. With the transmission arrangement

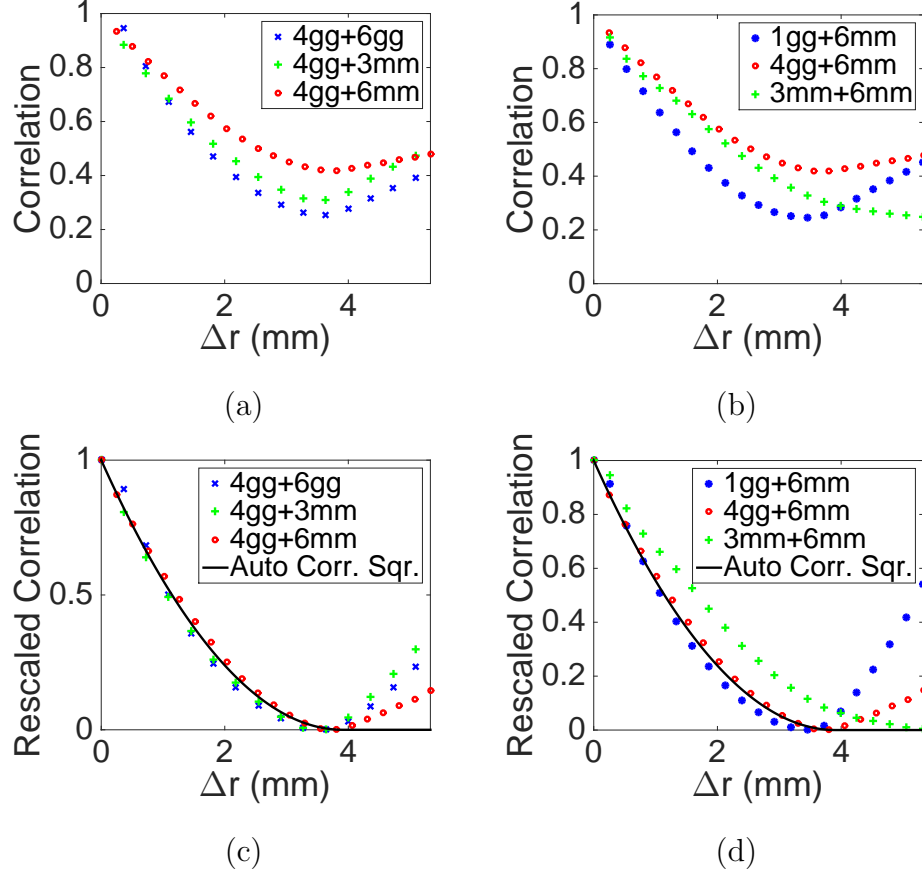


Fig. 4.5. Intensity correlations over object position with various amounts of scatter on either side of the object of interest, which is a circular patch of 3.7 mm in diameter. (a) and (c) show the measured correlation and the rescaled correlation for different amounts of scatter on the detector side (gg represents the number of ground glass used, and mm represents the thickness of acrylic slab). (b) and (d) show the measured correlation and the rescaled correlation for different amounts of scatter on the laser side. The measured correlation decreases at a slower rate to a larger minimum when more environmental scatter is present. The scaled speckle correlation ($|g_{ss}^{(1)}(\Delta \mathbf{r})|^2$) agrees with the magnitude squared of the autocorrelation of the circular patch of 3.7 mm in diameter except for the case of 3 mm acrylic slab at the laser side, for which laser heating dominates the change in speckle pattern.

of Fig. 4.2, where the spot being imaged in transmission is fixed in size, this increase in background scatter will result in smaller $\langle I_{ds} \rangle$ and hence a reduction in D_2/D_0 . For this reason, the minimum of the intensity correlation in Fig. 4.5(a) is increasing (producing a less pronounced dip) with increasing background scatter on the detector side. While $\langle I_d \rangle$ will reduce with increase in the background scatter, Fig. 4.5(a) and (4.11) are scaled by these means. The increase in background scatter will also increase $\langle I_{db} \rangle$, and this is reflected in the diminishing decorrelation dip in Fig. 4.5(a) as the background scatter on the detector side increases. We show, in Fig. 4.5(c) how well the theory given by (4.2) and (4.11) match the experiments for the rescaled data.

In another set of measurements, fixing the scatter on the detector side (6 mm thick acrylic slab) and varying the scatter on the laser side (the single ground glass diffuser, the four-piece stack of diffusers and the 3 mm thick acrylic slab, in order of increasing scatter) produced the results in Fig. 4.5(b). Increasing the amount of scattering on the laser side reduces the proportion of the background speckle scattered by the object. Conversely, with less scatter, the proportion of the background intensity scattered (absorbed) by the object increases, because the mean intensity is more peaked. As a result, the ratio $\langle I_{ds} \rangle / \langle I_{db} \rangle$ decreases with increasing background scatter on the laser side, and a small D_2/D_0 is expected based on (4.5) and (4.8). This is confirmed by the experimental results shown in Fig. 4.5(b), where the speckle intensity correlation decreases at a slower rate to a higher minimum as the medium on the laser side becomes more heavily scattering. The exception is the 3 mm thick acrylic slab, for which heating becomes the dominant source of change in the system, overshadowing the displacement of the small circular patch. We show in Fig. 4.5(d) that the prediction by (4.2) and (4.11) again match the experimental results accurately except for the case of the 3 mm thick acrylic slab on the laser side.

The impact of changing the scattering strength of the moving object and the surrounding environment, predicted by our theory in (4.5) and (4.8), are verified experimentally through the results shown in Fig. 4.4(a) and Fig. 4.5(a)(b), demonstrating quantitative and predictive character. Moreover, the agreement between our exper-

imental results and the predictions using (4.2) and (4.11), shown in Fig. 4.4(b) and in Fig. 4.5(c)(d), suggests that our key assumption, that D_0 and D_2 can be treated as constants and D_1 is negligibly small in these situations, has been validated.

4.4 Conclusion

Our sensing and imaging method using speckle intensity correlation over object position works well in a regime where the relatively static environmental scatter and the hidden object interacts so that the moving object is the main source of change in the system. When the detected field exhibits circular zero-mean Gaussian statistics and the object moves by its length within the measurement time-frame, our approach can lead to the reconstruction of the object function by fitting the values of the constants (D_0 , D_1 and D_2) and perform phase retrieval using the Fourier magnitude of the object obtained from the object's autocorrelation function. With D_0 , D_1 and D_2 containing the only unknown terms, and the denominator $\langle I_d(\mathbf{r}) \rangle \langle I_d(\mathbf{r} + \Delta \mathbf{r}) \rangle$ directly measurable, (4.11) represents an accurate model that leads to the excellent agreement with our experimental results. The dimension of the reconstruction is commensurate with the dimension of the object movement. The ratio between the constants D_0 and D_2 , once obtained, represents the relative strengths of the scattering environment and the moving object. This could lead to interesting applications in which the scattering strength of an unknown scattering environment can be sensed with a calibrated measurement, and direct comparison of the scattering strengths of different hidden objects is also feasible. It is noted that the measurement can be adapted into a reflection geometry for a wider range of practical applications. The velocity or the relative position of the moving object could be estimated by some established methods such as speckle temporal contrast or the Doppler shift [54] and the diffusion-based method [55].

We presented a general model that relates the averaged intensity correlation over the hidden object's position to the autocorrelation of the hidden object moving inside

heavily scattering environment. It not only enables imaging of hidden object inside an unprecedented heavily scattering medium, but also provides a way to probe the amount of environmental scatter and quantify the scattering strength of the hidden moving object in the system. While fluorescent imaging has proven useful in biological samples, our theory allows for coherent imaging at high resolution and without the need to introduce fluorescent reporters. By combining the accuracy of localization by emission [55] and coherent imaging based on motion, complementary and supporting information becomes available. For example, one could track a moving cellular cluster tagged with quantum dots inside deep tissue using emitted diffusive light and form an image of the tagged tissue using intensity correlations over object position that reflects absorption at a different wavelength *in vivo*. Experimental evidence is presented showing the general theory is in good agreement with the intensity decorrelation of various circular patches and that the speckle intensity images are sensitive to the size of the object and the amount of scatter in the surrounding environment. The capability of quantitatively sensing scattering strengths of a system greatly expands the scope of the possible applications of speckle intensity correlation over object position to expand prior capabilities for imaging in and through randomly scattering media.

5. THE THEORY OF SPECKLE INTENSITY CORRELATIONS OVER OBJECT POSITION

5.1 Introduction

Electromagnetic waves are of broad consequence in the natural and engineered world. Notably, photonics is pervasive in communications, optical sensing, and imaging, providing capacity by virtue of the carrier frequency and the transmission media, and information through spectroscopy, leading to the expanding presence of optical methods in medical research and medicine. Throughout the application spaces in science and technology, random scatter generally presents difficulties. For example, atmospheric scatter has long limited earth-based astronomy. Tissue scatter of light has precluded *in vivo* coherent imaging beyond the near-surface regime. Therefore, while there are fluorescent optical reporters for calcium channels, function and health in the mammalian brain remains largely a mystery because of tissue scatter. Even in single mode optical fibers, polarization mode dispersion results from scatter.

The scatter of coherent light from randomly arranged scatterers in bulk material or rough surfaces results in speckle, the granular intensity patterns from the interference between the wavefronts of the differently scattered fields, and if the scatterers move, the speckle pattern changes accordingly. Therefore, in principle, information about a scattering medium or the light impinging on such a medium is available. However, the challenge is to find a means to extract such information. Because of the difficulty associated with describing deterministic light propagation in the multiply-scattered regime, a statistical treatment becomes important [1]. Changes in speckle patterns are used in diffusing wave spectroscopy [6] and laser speckle contrast imaging [66], where motion reduces the local granular nature of the speckle pattern during the image collection window. The local speckle contrast ratio can thus be an indicator of the

velocity of blood flow under thin skin [65]. Decreasing the coherence (increasing the bandwidth of laser light) reduces the speckle contrast ratio (the ratio of the speckle intensity standard deviation to the mean), effectively reducing the graininess. There is thus a relationship between speckle decorrelation over scanned frequency and the transport of light through the scattering medium [17, 67]. The ensemble-averaged temporal response of a random medium, useful in characterizing random media and imaging, can be obtained using third-order correlations of speckle patterns over frequency, providing access to the Fourier phase, when the field is described by circular complex Gaussian statistics [17], allowing use of a moment theorem [16]. Control of the coherence of the light source provides a means to image hidden objects [4]. Practically, fixing the light source while increasing the scatter also reduces the contrast ratio. Speckle contrast can be reduced by reducing spatial coherence using, for example, random lasers, allowing full-field imaging [26]. Speckle intensity patterns can also be tailored to have artificial statistics, non-existing in naturally occurring speckle, using a spatial light modulator, and this has been considered for applications [68]. The presence of scatter can also increase communication capacity because of access to multiple independent channels [69, 70], as well as provide enhanced security [71, 72]. Characterization of the transmission properties of a random medium also the extraction the spectral properties of light incident on the scattering medium [73].

Imaging using coherent light offers high resolution, but increasing random scatter, such as occurs with biological tissue, eventually precludes direct observation. Consequently, coherent imaging of an object through a thick scattering medium is extremely difficult. The transmission of coherent light through a scattering medium has been studied intensely (see, for example, [41, 67, 74]). The memory effect (where the speckle pattern moves with the incident wave vector) [12] allows imaging through a scattering medium, as long as the thickness is small [12, 14, 15, 30, 32]. Wavefront control using a spatial light modulator and feedback control (based on a sensing arrangement at the point of interest) allows focusing through scatter [29, 48], facilitating point-wise imaging. While calculation as a basis for separating background random

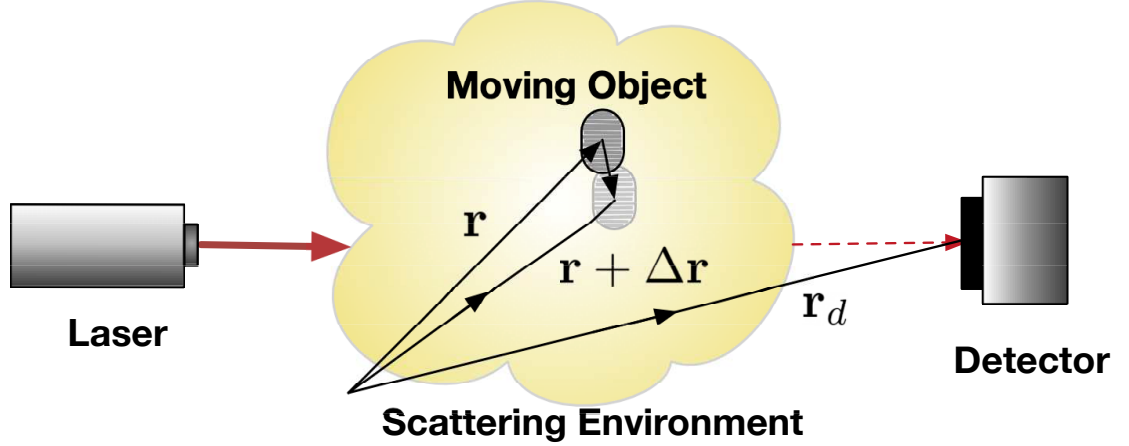


Fig. 5.1. A moving object in a scattering medium to be imaged, along with the spatial variables and the optical excitation and detection concept.

scatter is generally not viable because of computational complexity and the unknown location and precise character of the scatter, measurement of the field transmission matrix can facilitate imaging. This requires sensing within or on the other side of the scattering medium or guidestar control of a small volume [75–77]. The enhanced contrast is directly related to the effective number of the contributing transmission matrix eigenchannels based on random matrix calculations [47].

We develop a general statistical treatment that allows sensing and imaging of a moving object hidden inside a heavily scattering random background in a manner that is limited only by the number of photons detected. The imaging concept is presented in Fig. 5.1. Notably, the random background provides a structured field that also allows access to the far-subwavelength spatial information, along the lines of a proposal for super-resolution imaging with motion in prepared structured fields [78]. In this sense, the random scatter facilitates information that would otherwise be unavailable at a remote detector. The mathematical development generalizes earlier work showing the extraction of the incident field from correlations of intensity speckle patterns over translated field position [18, 19], the imaging of aperture-type objects

between scattering slabs [20], and recent experimental evidence that general objects can be imaged [21]. The new theory provides a means to image and motivation for a series of experiments to evaluate new aspects of the the information that can be accessed.

We treat the moving object parameterization in the context of the wave equation in Sect. 5.2. Intensity speckle patterns that can be measured as a function of object position are expanded as moments of the detected field in Sect. 5.3. Section 5.4 develops the relationship between the second order field moments and the object(s) to be imaged. The theory has short-range, subwavelength-scale information, and for macroscopic objects, information on the length scale commensurate with the object that can be used as a basis for sensing and imaging. Section 5.5 considers the physical basis of the normalized field correlation functions. The detector intensity correlation expression is developed in Sect. 5.6, where we arrive at a key relationship that is subsequently studied in Sect. 5.7 in terms length scale and the amount of the scatter from the moving object. Section 5.9 presents a discussion of issues related to the theory, the experimental studies, and key applications, and Sect. 5.10 projects the potential impact.

5.2 Object Parameterization

We treat the problem of imaging a moving object in a background randomly scattering medium (Fig. 5.1) as one where the background field without the object is considered as the incident field and the scattered field is that due to the object or objects of interest. This neglects possible displacement of background scatterers as the object of interest moves. Assuming a linear and locally time-invariant system during each measurement, the total field is exactly the superposition of the incident and scattered field everywhere. For scattering dielectric problems, it is convenient to use the electric field representation. The total field is $\mathbf{E} = \mathbf{E}_b + \mathbf{E}_s$, the sum of the background field (\mathbf{E}_b) and the scattered field (\mathbf{E}_s) due to the moving object. Our

interest here is in extracting information about the object from \mathbf{E}_s , but the challenge is that the associated field is heavily scattered by the background medium. Our treatment will use a Green's function for the wave equation, but this will remain unknown throughout the development we present, and is hence a formality that is presented for completeness.

The source-free Maxwell curl equations in the temporal frequency domain ($\exp(-i\omega t)$) and for non-magnetic media are

$$\nabla \times \mathbf{H} = -i\omega\epsilon_0\epsilon\mathbf{E} \quad (5.1)$$

$$\nabla \times \mathbf{E} = i\omega\mu_0\mathbf{H}, \quad (5.2)$$

where we have assumed that a complex, isotropic dielectric constant $\epsilon(\mathbf{r})$ describes the scattering problem, and \mathbf{H} is the magnetic field, μ_0 the free space permeability, and ϵ_0 the free space permittivity. From (5.1) and (5.2), the vector wave equation for \mathbf{E} becomes

$$\nabla \times \nabla \times \mathbf{E} - k_0^2\epsilon\mathbf{E} = 0. \quad (5.3)$$

Let

$$\epsilon(\mathbf{r}) = \epsilon_b(\mathbf{r}) + \epsilon_s(\mathbf{r}), \quad (5.4)$$

where $\epsilon_b(\mathbf{r})$ is the spatially dependent background dielectric constant that describes the random medium without the moving object(s) of interest and $\epsilon_s(\mathbf{r})$ is the contrast due to the moving scattering object to be imaged. Therefore, with use of (5.4), (5.3) becomes

$$\nabla \times \nabla \times \mathbf{E} - k_0^2\epsilon_b\mathbf{E} = k_0^2\epsilon_s\mathbf{E}. \quad (5.5)$$

Recognizing that $\nabla \times \nabla \times \mathbf{E}_b - k_0^2\epsilon_b\mathbf{E}_b = 0$, (5.5) can be written as

$$\nabla \times \nabla \times \mathbf{E}_s - k_0^2\epsilon_b\mathbf{E}_s = k_0^2\epsilon_s\mathbf{E}. \quad (5.6)$$

The Green's function wave equation corresponding to (5.6) is

$$\nabla \times \nabla \times \mathbf{G}(\mathbf{r}, \mathbf{r}') - k_0^2\epsilon_b(\mathbf{r})\mathbf{G}(\mathbf{r}, \mathbf{r}') = -\delta(\mathbf{r} - \mathbf{r}')\hat{\mathbf{p}}, \quad (5.7)$$

where the position vectors are now included for clarity, \mathbf{r}' is the (equivalent) source location and $\hat{\mathbf{p}}$ is drawn from the set of orthogonal unit vectors to produce the tensor \mathbf{G} . Using (5.7) and superposition to write the solution to (5.6), and with $\mathbf{E} = \mathbf{E}_b + \mathbf{E}_s$, we have

$$\mathbf{E}(\mathbf{r}) = \mathbf{E}_b(\mathbf{r}) - \int k_0^2 \epsilon_s(\mathbf{r}') \mathbf{G}(\mathbf{r}, \mathbf{r}') \mathbf{E}(\mathbf{r}') d\mathbf{r}' \quad (5.8)$$

as the exact representation for the scattering problem. Implicit in the following development is the dependence of measurable intensities on the incident field, and assuming a laser excitation, on the specifics of the illumination.

In an experiment [19, 20], polarized light is detected. Consequently, the electric field with direction $\hat{\mathbf{d}}$ is sifted, so (5.8) assumes the scalar form

$$\begin{aligned} E(\mathbf{r}) &= E_b(\mathbf{r}) + \int O(\mathbf{r}') \hat{\mathbf{d}} \cdot [\mathbf{G}(\mathbf{r}, \mathbf{r}') \mathbf{E}(\mathbf{r}')] d\mathbf{r}' \\ &= E_b(\mathbf{r}) + E_s(\mathbf{r}). \end{aligned} \quad (5.9)$$

Without loss of generality, we can define a simplified scalar object function as

$$O(\mathbf{r}') = -k_0^2 \epsilon_s(\mathbf{r}'). \quad (5.10)$$

The development of the imaging formulation exploits this simplified scalar picture with the exact interpretation that the vector field is being sampled at the detector through a polarizer. Note also that with application of (5.8) we assume a homogenized description of the object. However, the local homogenized picture could represent length scales down to the nanometer regime.

5.3 Detected Field Moments

Consider a point detector located at $\mathbf{r} = \mathbf{r}_d$, as in Fig. 5.1, and define the field at this point by $E(\mathbf{r}_d) \equiv E_d$, where the spatial argument is represented as a subscript for compactness. We assume measurements that reflect E_d at a sequence of object positions defined by a reference position \mathbf{r} and a translation vector $\Delta\mathbf{r}$. We can thus

describe the field at the detector as $E_d(\mathbf{r})$ with the object at some reference position and $E_d(\mathbf{r} + \Delta\mathbf{r})$ with the object at the displaced position defined by $\Delta\mathbf{r}$.

The background scattering process is treated as random, and the fields at some \mathbf{r}_d can be considered as a random phasor sum with developed statistics so that E_d is zero-mean circular Gaussian [1]. This also provides access to a moment theorem made widely known by Reed [16], and with stationary statistics the special cases of the second and fourth moments are related in a manner presented earlier by Siegert [79]. We define the statistical average $\langle \cdot \rangle$ as being over background scatterer configuration. Section 5.8 considers the practical aspects of how the average is determined experimentally with speckle intensity data obtained by a camera.

The intensity is assumed to be measured, and we write the intensity at the detector as $I_d = |E_d|^2$, where a normalized impedance is assumed that is ultimately irrelevant because of scaling. The fourth order field moment provides the measured intensity correlation over object position as [16]

$$\begin{aligned} \langle I_d(\mathbf{r}) I_d(\mathbf{r} + \Delta\mathbf{r}) \rangle &= \langle E_d(\mathbf{r}) E_d^*(\mathbf{r}) E_d(\mathbf{r} + \Delta\mathbf{r}) E_d^*(\mathbf{r} + \Delta\mathbf{r}) \rangle \\ &= \langle I_d(\mathbf{r}) \rangle \langle I_d(\mathbf{r} + \Delta\mathbf{r}) \rangle + \langle E_d^*(\mathbf{r}) E_d(\mathbf{r} + \Delta\mathbf{r}) \rangle \langle E_d^*(\mathbf{r} + \Delta\mathbf{r}) E_d(\mathbf{r}) \rangle \\ &= \langle I_d(\mathbf{r}) \rangle \langle I_d(\mathbf{r} + \Delta\mathbf{r}) \rangle + |\langle E_d^*(\mathbf{r}) E_d(\mathbf{r} + \Delta\mathbf{r}) \rangle|^2. \end{aligned} \quad (5.11)$$

Equation (5.11) will be used throughout our development.

It is convenient to define a normalized field

$$\tilde{E} = \frac{E}{\langle I \rangle^{1/2}}, \quad (5.12)$$

with $I = |E|^2$, and a normalized intensity

$$\tilde{I} = \frac{(I - \langle I \rangle)}{\langle I \rangle}. \quad (5.13)$$

The normalization for field (giving \tilde{E}) in (5.12) is consistent with that for intensity (\tilde{I}) in (5.13). For a Gaussian field [16], $\langle I^2 \rangle = 2\langle I \rangle^2$, so the intensity variance is

$$\begin{aligned} \sigma_I^2 &= \langle I^2 \rangle - \langle I \rangle^2 \\ &= \langle I \rangle^2. \end{aligned} \quad (5.14)$$

The contrast ration is thus $\sigma_I/\langle I \rangle = 1$ [1].

The second order field correlation over object position, measured at the detector, is

$$G^{(1)}(\mathbf{r}_d; \mathbf{r}, \mathbf{r} + \Delta\mathbf{r}) = \langle E_d^*(\mathbf{r}) E_d(\mathbf{r} + \Delta\mathbf{r}) \rangle \equiv G^{(1)}(\mathbf{r}, \mathbf{r} + \Delta\mathbf{r}), \quad (5.15)$$

where we use a common notation for the second order field moment ($G^{(1)}(\cdot)$) and a compact argument to simplify the form of subsequent expressions, where the implication is a measurement at a single detector point (\mathbf{r}_d). With the use of normalizations involving the mean intensity, $\langle \tilde{E}_d^*(\mathbf{r}) \tilde{E}_d(\mathbf{r} + \Delta\mathbf{r}) \rangle \rightarrow \langle \tilde{E}_d^*(0) \tilde{E}_d(\Delta\mathbf{r}) \rangle$, and the normalized field (and intensity) correlations become independent of the object reference position \mathbf{r} . The normalized averaged field correlation measured at the detector point as the object is scanned is then

$$\begin{aligned} g^{(1)}(\Delta\mathbf{r}) &= \langle \tilde{E}_d^*(0) \tilde{E}_d(\Delta\mathbf{r}) \rangle \\ &= \frac{G^{(1)}(\mathbf{r}, \mathbf{r} + \Delta\mathbf{r})}{\langle I_d(\mathbf{r}) \rangle^{1/2} \langle I_d(\mathbf{r} + \Delta\mathbf{r}) \rangle^{1/2}}. \end{aligned} \quad (5.16)$$

Use of (5.12) or (5.13) and (5.16) with (5.11) gives

$$\begin{aligned} \langle \tilde{I}_d(\mathbf{r}) \tilde{I}_d(\mathbf{r} + \Delta\mathbf{r}) \rangle &= \langle \tilde{I}_d(0) \tilde{I}_d(\Delta\mathbf{r}) \rangle \\ &= |g^{(1)}(\Delta\mathbf{r})|^2 \\ &\equiv g^{(2)}(\Delta\mathbf{r}). \end{aligned} \quad (5.17)$$

While object information is in principle embedded in (5.17), this interpretation of normalized measured data does not provide for imaging. We present a theory that provides a clear path to a method to invert measured data and form an image.

5.4 Relationship Between Object and Detected Field Moments

Returning to (5.9), we write the field at the detector as a superposition of that due to the background random scatter (E_{db}) and that due to the object (defined as the scattered field, E_{ds}), under the assumption that this distinction will become

meaningful. Expanding the second-order field correlation with this field superposition, we have

$$\begin{aligned}
\langle E_d^*(\mathbf{r})E_d(\mathbf{r} + \Delta\mathbf{r}) \rangle &= \langle E_{db}^*(\mathbf{r})E_{db}(\mathbf{r} + \Delta\mathbf{r}) \rangle + \langle E_{db}^*(\mathbf{r})E_{ds}(\mathbf{r} + \Delta\mathbf{r}) \rangle \\
&+ \langle E_{ds}^*(\mathbf{r})E_{db}(\mathbf{r} + \Delta\mathbf{r}) \rangle + \langle E_{ds}^*(\mathbf{r})E_{ds}(\mathbf{r} + \Delta\mathbf{r}) \rangle \\
&= \langle I_{db} \rangle + \langle E_{db}^*E_{ds}(\mathbf{r} + \Delta\mathbf{r}) \rangle + \langle E_{ds}^*(\mathbf{r})E_{db} \rangle \\
&+ \langle E_{ds}^*(\mathbf{r})E_{ds}(\mathbf{r} + \Delta\mathbf{r}) \rangle.
\end{aligned} \tag{5.18}$$

Note that $E_{db}(\mathbf{r}) = E_{db}(\mathbf{r} + \Delta\mathbf{r}) = E_{db}$, because the background field is that without the object (the incident field), so $\langle E_{db}^*(\mathbf{r})E_{db}(\mathbf{r} + \Delta\mathbf{r}) \rangle = \langle E_{db}^*E_{db} \rangle = \langle I_{db} \rangle$, dictated by the optical excitation, the scattering medium, and the detector location, but independent of the moving object.

In (5.18), referring to (5.9) and (5.10), $E_{ds} = E_s(\mathbf{r}_d)$, so with the object at the reference position \mathbf{r} ,

$$E_{ds}(\mathbf{r}) = \int O(\mathbf{r}'; \mathbf{r}) \hat{\mathbf{d}} \cdot [\mathbf{G}(\mathbf{r}_d, \mathbf{r}')\mathbf{E}(\mathbf{r}')] d\mathbf{r}', \tag{5.19}$$

where $O(\mathbf{r}')$ defines the object through (5.10). This allows us to build expressions for each of the three remaining terms in (5.18).

First, from (5.19) and with a shift in object position of $\Delta\mathbf{r}$,

$$\begin{aligned}
\langle E_{ds}^*(\mathbf{r})E_{ds}(\mathbf{r} + \Delta\mathbf{r}) \rangle &= \left\langle \int O^*(\mathbf{r}'; \mathbf{r}) \hat{\mathbf{d}} \cdot [\mathbf{G}(\mathbf{r}_d, \mathbf{r}')\mathbf{E}(\mathbf{r}')]^* d\mathbf{r}' \right. \\
&\quad \left. \int O(\mathbf{r}'; \mathbf{r} + \Delta\mathbf{r}) \hat{\mathbf{d}} \cdot [\mathbf{G}(\mathbf{r}_d, \mathbf{r}')\mathbf{E}(\mathbf{r}')] d\mathbf{r}' \right\rangle \\
&= \left\langle \int d\mathbf{r}' \int d\mathbf{r}'' O^*(\mathbf{r}'; \mathbf{r}) \hat{\mathbf{d}} \cdot [\mathbf{G}(\mathbf{r}_d, \mathbf{r}')\mathbf{E}(\mathbf{r}')]^* \right. \\
&\quad \left. O(\mathbf{r}''; \mathbf{r} + \Delta\mathbf{r}) \hat{\mathbf{d}} \cdot [\mathbf{G}(\mathbf{r}_d, \mathbf{r}'')\mathbf{E}(\mathbf{r}'')] \right\rangle \\
&= \langle I_{ds}(\mathbf{r}) \rangle^{1/2} \langle I_{ds}(\mathbf{r} + \Delta\mathbf{r}) \rangle^{1/2} g_{ss}^{(1)}(\Delta\mathbf{r})
\end{aligned} \tag{5.20}$$

$$= G_{ss}^{(1)}(\mathbf{r}, \mathbf{r} + \Delta\mathbf{r}), \tag{5.21}$$

so

$$\begin{aligned}
g_{ss}^{(1)}(\Delta \mathbf{r}) &= \langle I_{ds}(\mathbf{r}) \rangle^{-1/2} \langle I_{ds}(\mathbf{r} + \Delta \mathbf{r}) \rangle^{-1/2} \\
&\quad \langle \int d\mathbf{r}' \int d\mathbf{r}'' O^*(\mathbf{r}'; \mathbf{r}) \hat{\mathbf{d}} \cdot [\mathbf{G}(\mathbf{r}_d, \mathbf{r}') \mathbf{E}(\mathbf{r}')]^* O(\mathbf{r}''; \mathbf{r} + \Delta \mathbf{r}) \hat{\mathbf{d}} \cdot [\mathbf{G}(\mathbf{r}_d, \mathbf{r}'') \mathbf{E}(\mathbf{r}'')] \rangle \\
&= \langle \tilde{E}_{ds}^*(0) \tilde{E}_{ds}(\Delta \mathbf{r}) \rangle \\
&= a_{ss}(\Delta \mathbf{r}) e^{i\phi_{ss}(\Delta \mathbf{r})}.
\end{aligned} \tag{5.22}$$

We note from (5.22) that the normalization results in $|g_{ss}^{(1)}(0)| = 1$, so that $a_{ss}(0) = 1$ and $\phi_{ss}(0) = 0$. Notice that $g_{ss}^{(1)}$ in principle provides access to a measure of the spatial correlation of the object, something we pursue later. The challenge is to relate $g_{ss}^{(1)}$ to a measurable quantity, because I_{ds} is not directly available.

Like (5.21), using (5.19), we have

$$\begin{aligned}
\langle E_{db}^*(\mathbf{r}) E_{ds}(\mathbf{r} + \Delta \mathbf{r}) \rangle &= \langle E_{db}^* \int O(\mathbf{r}'; \mathbf{r} + \Delta \mathbf{r}) \hat{\mathbf{d}} \cdot [\mathbf{G}(\mathbf{r}_d, \mathbf{r}') \mathbf{E}(\mathbf{r}')] d\mathbf{r}' \rangle \\
&= \langle I_{db} \rangle^{1/2} \langle I_{ds}(\mathbf{r} + \Delta \mathbf{r}) \rangle^{1/2} g_{bs}^{(1)}(\Delta \mathbf{r}).
\end{aligned} \tag{5.23}$$

Hence,

$$\begin{aligned}
g_{bs}^{(1)}(\Delta \mathbf{r}) &= \langle \tilde{E}_{db}^* \tilde{E}_{ds}(\Delta \mathbf{r}) \rangle \\
&= a_{bs}(\Delta \mathbf{r}) e^{i\phi_{bs}(\Delta \mathbf{r})},
\end{aligned} \tag{5.24}$$

and $|g_{bs}^{(1)}(0)| = 0$.

The final term in (5.18) is thus

$$\begin{aligned}
\langle E_{ds}^*(\mathbf{r}) E_{db} \rangle &= \langle I_{ds}(\mathbf{r}) \rangle^{1/2} \langle I_{db} \rangle^{1/2} g_{sb}^{(1)}(0) \\
&\equiv \langle I_{ds}(\mathbf{r}) \rangle^{1/2} \langle I_{db} \rangle^{1/2} g_{bs}^{(1)*}(0),
\end{aligned} \tag{5.25}$$

where we have

$$\begin{aligned}
g_{sb}^{(1)}(0) &= \langle \tilde{E}_{ds}^*(\mathbf{r}) \tilde{E}_{db} \rangle \\
&= a_{sb}(0) e^{\phi_{sb}(0)} \\
&= e^{\phi_{sb}(0)} \\
&= e^{-\phi_{bs}(0)} \\
&\equiv g_{bs}^{(1)*}(0).
\end{aligned} \tag{5.26}$$

Collecting the various terms, we can thus write the field correlation over object position measured at the detector point, from (5.18), as

$$\begin{aligned}
\langle E_d^*(\mathbf{r})E_d(\mathbf{r} + \Delta\mathbf{r}) \rangle &= \langle E_{db}^*E_{db} \rangle + \langle E_{db}^*(\mathbf{r})E_{ds}(\mathbf{r} + \Delta\mathbf{r}) \rangle \\
&\quad + \langle E_{ds}^*(\mathbf{r})E_{db}(\mathbf{r} + \Delta\mathbf{r}) \rangle + \langle E_{ds}^*(\mathbf{r})E_{ds}(\mathbf{r} + \Delta\mathbf{r}) \rangle \\
&= \langle I_{db} \rangle + \langle I_{db} \rangle^{1/2} \langle I_{ds}(\mathbf{r} + \Delta\mathbf{r}) \rangle^{1/2} g_{bs}^{(1)}(\Delta\mathbf{r}) \\
&\quad + \langle I_{ds}(\mathbf{r}) \rangle^{1/2} \langle I_{db} \rangle^{1/2} g_{bs}^{(1)*}(0) \\
&\quad + \langle I_{ds}(\mathbf{r}) \rangle^{1/2} \langle I_{ds}(\mathbf{r} + \Delta\mathbf{r}) \rangle^{1/2} g_{ss}^{(1)}(\Delta\mathbf{r}). \tag{5.27}
\end{aligned}$$

Interpretations of (5.27) will prove useful in imaging based on motion in scattering media.

5.5 Physical Basis of $g_{ss}^{(1)}(\Delta\mathbf{r})$ and $g_{bs}^{(1)}(\Delta\mathbf{r})$

Referring to (5.22), experimental evidence indicates that correlations of the scattered field from the object and the translated object survive the averaging process [19–21]. Macroscopically, referring to Fig. 5.1, this situation is when the object and the translated object share a joint spatial support. Therefore, $g_{ss}^{(1)}(\Delta\mathbf{r})$ has correlated scattered field contributions from the object and the shifted object when they share a common spatial support. We will separate $g_{ss}^{(1)}(\Delta\mathbf{r})$ into short range and long range terms. The short range decorrelation is sensitive to the microstructure and sub-wavelength features, and the long range to macroscopic object information.

The autocorrelation of the object function is

$$\Gamma(\Delta\mathbf{r}) = \int d\mathbf{r}' O^*(\mathbf{r}') O(\mathbf{r}' + \Delta\mathbf{r}). \tag{5.28}$$

A comparison of (5.22) and (5.28), under conditions of sufficient random scatter for developed statistics, suggests

$$\begin{aligned}
g_{ss}^{(1)}(\Delta\mathbf{r}) &= \gamma(\Delta\mathbf{r}) \\
&= \int d\mathbf{r}' \tilde{O}^*(\mathbf{r}') \tilde{O}(\mathbf{r}' + \Delta\mathbf{r}), \tag{5.29}
\end{aligned}$$

where γ is the normalized autocorrelation and \tilde{O} is the normalized object function. With (5.29), information related to $g_{ss}^{(1)}(\Delta\mathbf{r})$ leads to a means to retrieve \tilde{O} , as we will describe.

Possibly less obvious is the role of $g_{bs}^{(1)}(\Delta\mathbf{r})$ and its character, upon observation of the average field correlation in (5.23). It is insightful to consider the Gedanken experiment of a detected field correlation without displacement. Based on (5.18), the mean intensity at the detector point with the object at the reference position is

$$\begin{aligned}\langle I_d(\mathbf{r}) \rangle &= \langle E_d^*(\mathbf{r}) E_d(\mathbf{r}_0) \rangle \\ &= \langle I_{db} \rangle + 2\Re\{\langle E_{db}^* E_{ds}(\mathbf{r}) \rangle\} + \langle I_{ds}(\mathbf{r}) \rangle \\ &= \langle I_{db} \rangle + \langle I_{ds}(\mathbf{r}) \rangle + \langle I_{db} \rangle^{1/2} \langle I_{ds}(\mathbf{r}) \rangle^{1/2} 2\Re\{g_{bs}^{(1)}(0)\},\end{aligned}\quad (5.30)$$

with $\Re\{\cdot\}$ the real part. The term $\langle E_{db}^* E_{ds} \rangle$ is captured by $g_{bs}^{(1)}(0)$. This is the only way to describe a decrease in mean intensity with the introduction of an object that reduces the background intensity. Therefore, in general, $g_{bs}^{(1)}$ must be retained in the intensity correlation expressions. Also, clear from (5.30), $g_{bs}^{(1)}(0)$ has negative real part for situations where $\langle I_{db} \rangle > \langle I_d \rangle$. From (5.24), we anticipate that $g_{bs}^{(1)}(\Delta\mathbf{r})$ will reduce to zero when the object translation is large compared to λ . This position rests on substantial uncorrelated scattering centers in the moving object in relation to the background random scatter.

Note from (5.23) that $g_{bs}^{(1)}(0)$ is normalized by $\langle I_{ds} \rangle$, which provides the scattering strength. If $\langle I_{ds} \rangle^{1/2} g_{bs}^{(1)}(0)$ were available, this could provide object information that could in principle be used in conjunction with or instead of $g_{ss}^{(1)}(\Delta\mathbf{r})$ for sensing and imaging the moving object.

In addition to information about the microstructure, the small distance decorrelation is influenced by a statistical field decorrelation. By analogy with field correlations over frequency [80], a random phasor sum description in the Gaussian field limit indicates a pathlength distribution with a differential phase shift $k\Delta x < \lambda$ can result from the statistical average, leading to a decorrelation over $|\Delta\mathbf{r}| \sim \lambda$. Irrespective of the details of the moving object, we therefore expect a contribution from point scatterer

motion on this length scale, and that this will influence $g_{ss}^{(1)}$ and $g_{bs}^{(1)}$. Embedded in this will be nanostructure information about the object.

5.6 Detector Intensity Correlation

From (5.11), the intensity correlation at the detector point measured over object position is

$$\langle I_d(\mathbf{r})I_d(\mathbf{r} + \Delta\mathbf{r}) \rangle = \langle I_d(\mathbf{r}) \rangle \langle I_d(\mathbf{r} + \Delta\mathbf{r}) \rangle + |\langle E_d^*(\mathbf{r})E_d(\mathbf{r} + \Delta\mathbf{r}) \rangle|^2. \quad (5.31)$$

Using (5.27), we have

$$\begin{aligned} |\langle E_d^*(\mathbf{r})E_d(\mathbf{r} + \Delta\mathbf{r}) \rangle|^2 &= \langle I_{db} \rangle^2 + \langle I_{db} \rangle^{3/2} \langle I_{ds}(\mathbf{r} + \Delta\mathbf{r}) \rangle^{1/2} g_{bs}^{(1)*}(\Delta\mathbf{r}) \\ &\quad + \langle I_{db} \rangle^{3/2} \langle I_{ds}(\mathbf{r}) \rangle^{1/2} g_{bs}^{(1)}(0) \\ &\quad + \langle I_{db} \rangle \langle I_{ds}(\mathbf{r}) \rangle^{1/2} \langle I_{ds}(\mathbf{r} + \Delta\mathbf{r}) \rangle^{1/2} g_{ss}^{(1)*}(\Delta\mathbf{r}) \\ + \quad &\langle I_{db} \rangle^{3/2} \langle I_{ds}(\mathbf{r} + \Delta\mathbf{r}) \rangle^{1/2} g_{bs}^{(1)}(\Delta\mathbf{r}) + \langle I_{db} \rangle \langle I_{ds}(\mathbf{r} + \Delta\mathbf{r}) \rangle |g_{bs}^{(1)}(\Delta\mathbf{r})|^2 \\ &\quad + \langle I_{db} \rangle \langle I_{ds}(\mathbf{r}) \rangle^{1/2} \langle I_{ds}(\mathbf{r} + \Delta\mathbf{r}) \rangle^{1/2} g_{bs}^{(1)}(\Delta\mathbf{r}) g_{bs}^{(1)}(0) \\ &\quad + \langle I_{db} \rangle^{1/2} \langle I_{ds}(\mathbf{r}) \rangle^{1/2} \langle I_{ds}(\mathbf{r} + \Delta\mathbf{r}) \rangle g_{bs}^{(1)}(\Delta\mathbf{r}) g_{ss}^{(1)*}(\Delta\mathbf{r}) \\ + \quad &\langle I_{db} \rangle^{3/2} \langle I_{ds}(\mathbf{r}) \rangle^{1/2} g_{bs}^{(1)*}(0) + \langle I_{db} \rangle \langle I_{ds}(\mathbf{r}) \rangle^{1/2} \langle I_{ds}(\mathbf{r} + \Delta\mathbf{r}) \rangle^{1/2} g_{bs}^{(1)*}(0) g_{bs}^{(1)*}(\Delta\mathbf{r}) \\ &\quad + \langle I_{db} \rangle \langle I_{ds}(\mathbf{r}) \rangle |g_{bs}^{(1)}(0)|^2 \\ &\quad + \langle I_{db} \rangle^{1/2} \langle I_{ds}(\mathbf{r}) \rangle \langle I_{ds}(\mathbf{r} + \Delta\mathbf{r}) \rangle^{1/2} g_{bs}^{(1)*}(0) g_{ss}^{(1)*}(\Delta\mathbf{r}) \\ + \quad &\langle I_{db} \rangle \langle I_{ds}(\mathbf{r}) \rangle^{1/2} \langle I_{ds}(\mathbf{r} + \Delta\mathbf{r}) \rangle^{1/2} g_{ss}^{(1)}(\Delta\mathbf{r}) \\ &\quad + \langle I_{db} \rangle^{1/2} \langle I_{ds}(\mathbf{r}) \rangle^{1/2} \langle I_{ds}(\mathbf{r} + \Delta\mathbf{r}) \rangle g_{ss}^{(1)}(\Delta\mathbf{r}) g_{bs}^{(1)*}(\Delta\mathbf{r}) \\ &\quad + \langle I_{db} \rangle^{1/2} \langle I_{ds}(\mathbf{r}) \rangle \langle I_{ds}(\mathbf{r} + \Delta\mathbf{r}) \rangle^{1/2} g_{ss}^{(1)}(\Delta\mathbf{r}) g_{bs}^{(1)}(0) \\ &\quad + \langle I_{ds}(\mathbf{r}) \rangle \langle I_{ds}(\mathbf{r} + \Delta\mathbf{r}) \rangle |g_{ss}^{(1)*}(\Delta\mathbf{r})|^2. \end{aligned} \quad (5.32)$$

Rearranging (5.32) according to the increasing order of $\langle I_{db} \rangle$ gives

$$\begin{aligned}
|\langle E_d^*(\mathbf{r})E_d(\mathbf{r} + \Delta\mathbf{r}) \rangle|^2 &= \langle I_{db} \rangle^2 \\
&+ \langle I_{db} \rangle^{3/2} \left[\langle I_{ds}(\mathbf{r} + \Delta\mathbf{r}) \rangle^{1/2} 2\Re\{g_{bs}^{(1)}(\Delta\mathbf{r})\} + \langle I_{ds}(\mathbf{r}) \rangle^{1/2} 2\Re\{g_{bs}^{(1)}(0)\} \right] \\
&+ \langle I_{db} \rangle \left\{ \langle I_{ds}(\mathbf{r}) \rangle^{1/2} \langle I_{ds}(\mathbf{r} + \Delta\mathbf{r}) \rangle^{1/2} [2\Re\{g_{ss}^{(1)}(\Delta\mathbf{r})\} + 2\Re\{g_{bs}^{(1)}(0)g_{bs}^{(1)}(\Delta\mathbf{r})\}] \right. \\
&+ \langle I_{ds}(\mathbf{r}) \rangle |g_{bs}^{(1)}(0)|^2 + \langle I_{ds}(\mathbf{r} + \Delta\mathbf{r}) \rangle |g_{bs}^{(1)}(\Delta\mathbf{r})|^2 \left. \right\} \\
&+ \langle I_{db} \rangle^{1/2} \left[\langle I_{ds}(\mathbf{r}) \rangle^{1/2} \langle I_{ds}(\mathbf{r} + \Delta\mathbf{r}) \rangle 2\Re\{g_{bs}^{(1)}(\Delta\mathbf{r})g_{ss}^{(1)*}(\Delta\mathbf{r})\} \right. \\
&\quad \left. + \langle I_{ds}(\mathbf{r}) \rangle \langle I_{ds}(\mathbf{r} + \Delta\mathbf{r}) \rangle^{1/2} 2\Re\{g_{bs}^{(1)}(0)g_{ss}^{(1)}(\Delta\mathbf{r})\} \right] \\
&+ \langle I_{ds}(\mathbf{r}) \rangle \langle I_{ds}(\mathbf{r} + \Delta\mathbf{r}) \rangle |g_{ss}^{(1)}(\Delta\mathbf{r})|^2. \tag{5.33}
\end{aligned}$$

We note that (5.33) is informative for situations where $\langle I_{db} \rangle$ is large or small, thereby allowing discrimination based on significant amplitudes at the detector. However, our interest is in imaging a moving object. Therefore, we distill (5.32) into terms involving orders of $g_{ss}^{(1)}$, giving

$$\begin{aligned}
|\langle E_d^*(\mathbf{r})E_d(\mathbf{r} + \Delta\mathbf{r}) \rangle|^2 &= \left\{ \langle I_{db} \rangle^2 \right. \\
&+ \langle I_{db} \rangle^{3/2} \left[\langle I_{ds}(\mathbf{r} + \Delta\mathbf{r}) \rangle^{1/2} 2\Re\{g_{bs}^{(1)}(\Delta\mathbf{r})\} + \langle I_{ds}(\mathbf{r}) \rangle^{1/2} 2\Re\{g_{bs}^{(1)}(0)\} \right] \\
&+ \langle I_{db} \rangle \langle I_{ds}(\mathbf{r}) \rangle^{1/2} \langle I_{ds}(\mathbf{r} + \Delta\mathbf{r}) \rangle^{1/2} 2\Re\{g_{bs}^{(1)}(0)g_{bs}^{(1)}(\Delta\mathbf{r})\} \\
&+ \langle I_{db} \rangle \langle I_{ds}(\mathbf{r}) \rangle |g_{bs}^{(1)}(0)|^2 + \langle I_{db} \rangle \langle I_{ds}(\mathbf{r} + \Delta\mathbf{r}) \rangle |g_{bs}^{(1)}(\Delta\mathbf{r})|^2 \left. \right\} \\
&+ \left\{ \langle I_{db} \rangle^{1/2} \left[\langle I_{ds}(\mathbf{r}) \rangle^{1/2} \langle I_{ds}(\mathbf{r} + \Delta\mathbf{r}) \rangle 2\Re\{g_{bs}^{(1)}(\Delta\mathbf{r})g_{ss}^{(1)*}(\Delta\mathbf{r})\} \right. \right. \\
&\quad \left. \left. + \langle I_{ds}(\mathbf{r}) \rangle \langle I_{ds}(\mathbf{r} + \Delta\mathbf{r}) \rangle^{1/2} 2\Re\{g_{bs}^{(1)}(0)g_{ss}^{(1)}(\Delta\mathbf{r})\} \right] \right. \\
&+ \langle I_{db} \rangle \langle I_{ds}(\mathbf{r}) \rangle^{1/2} \langle I_{ds}(\mathbf{r} + \Delta\mathbf{r}) \rangle^{1/2} 2\Re\{g_{ss}^{(1)}(\Delta\mathbf{r})\} \left. \right\} \\
&+ \langle I_{ds}(\mathbf{r}) \rangle \langle I_{ds}(\mathbf{r} + \Delta\mathbf{r}) \rangle |g_{ss}^{(1)}(\Delta\mathbf{r})|^2. \tag{5.34}
\end{aligned}$$

It is convenient to convert raw measured speckle intensity data into normalized form (\tilde{I}) using (5.13). This step also simplifies the mathematical representation. In normalized form, (5.31) becomes

$$\langle \tilde{I}_d(0)\tilde{I}_d(\Delta\mathbf{r}) \rangle = \langle \tilde{I}_d(\mathbf{r})\tilde{I}_d(\mathbf{r} + \Delta\mathbf{r}) \rangle = \left| \langle \tilde{E}_d^*(\mathbf{r})\tilde{E}_d(\mathbf{r}_0 + \Delta\mathbf{r}) \rangle \right|^2, \tag{5.35}$$

where

$$\tilde{E}_d(\mathbf{r}) = \frac{E_d(\mathbf{r})}{\langle I_d(\mathbf{r}_0) \rangle^{1/2}} = \tilde{E}_d(0) \quad (5.36)$$

$$\tilde{E}_d(\mathbf{r} + \Delta\mathbf{r}) = \frac{E_d(\mathbf{r} + \Delta\mathbf{r})}{\langle I_d(\mathbf{r} + \Delta\mathbf{r}) \rangle^{1/2}} = \tilde{E}_d(\Delta\mathbf{r}), \quad (5.37)$$

and, as before, the normalized fields depend only on the translation, $\Delta\mathbf{r}$. Drawing on (5.34) - (5.37), we can write

$$\begin{aligned} \langle \tilde{I}_d(0) \tilde{I}_d(\Delta\mathbf{r}) \rangle &= C_0(\Delta\mathbf{r}) \\ &+ C_{11}(\Delta\mathbf{r}) 2\Re\{g_{bs}^{(1)}(\Delta\mathbf{r}) g_{ss}^{(1)*}(\Delta\mathbf{r})\} + C_{12}(\Delta\mathbf{r}) 2\Re\{g_{bs}^{(1)}(0) g_{ss}^{(1)}(\Delta\mathbf{r})\} \\ &+ C_{13}(\Delta\mathbf{r}) 2\Re\{g_{ss}^{(1)}(\Delta\mathbf{r})\} + C_2(\Delta\mathbf{r}) |g_{ss}^{(1)}(\Delta\mathbf{r})|^2, \end{aligned} \quad (5.38)$$

where, referring to (5.34),

$$\begin{aligned} C_0(\Delta\mathbf{r}) &= \langle I_d(\mathbf{r}) \rangle^{-1} \langle I_d(\mathbf{r} + \Delta\mathbf{r}) \rangle^{-1} \left\{ \langle I_{db} \rangle^2 \right. \\ &+ \langle I_{db} \rangle^{3/2} \left[\langle I_{ds}(\mathbf{r} + \Delta\mathbf{r}) \rangle^{1/2} 2\Re\{g_{bs}^{(1)}(\Delta\mathbf{r})\} + \langle I_{ds}(\mathbf{r}) \rangle^{1/2} 2\Re\{g_{bs}^{(1)}(0)\} \right] \\ &+ \langle I_{db} \rangle \langle I_{ds}(\mathbf{r}) \rangle^{1/2} \langle I_{ds}(\mathbf{r} + \Delta\mathbf{r}) \rangle^{1/2} 2\Re\{g_{bs}^{(1)}(0) g_{bs}^{(1)}(\Delta\mathbf{r})\} \\ &\left. + \langle I_{db} \rangle \langle I_{ds}(\mathbf{r}) \rangle + \langle I_{db} \rangle \langle I_{ds}(\mathbf{r} + \Delta\mathbf{r}) \rangle |g_{bs}^{(1)}(\Delta\mathbf{r})|^2 \right\} \\ C_{11}(\Delta\mathbf{r}) &= \langle I_d(\mathbf{r}) \rangle^{-1} \langle I_d(\mathbf{r} + \Delta\mathbf{r}) \rangle^{-1} \langle I_{db} \rangle^{1/2} \langle I_{ds}(\mathbf{r}) \rangle^{1/2} \langle I_{ds}(\mathbf{r} + \Delta\mathbf{r}) \rangle \\ C_{12}(\Delta\mathbf{r}) &= \langle I_d(\mathbf{r}) \rangle^{-1} \langle I_d(\mathbf{r} + \Delta\mathbf{r}) \rangle^{-1} \langle I_{db} \rangle^{1/2} \langle I_{ds}(\mathbf{r}) \rangle \langle I_{ds}(\mathbf{r} + \Delta\mathbf{r}) \rangle^{1/2} \\ C_{13}(\Delta\mathbf{r}) &= \langle I_d(\mathbf{r}) \rangle^{-1} \langle I_d(\mathbf{r} + \Delta\mathbf{r}) \rangle^{-1} \langle I_{db} \rangle \langle I_{ds}(\mathbf{r}) \rangle^{1/2} \langle I_{ds}(\mathbf{r} + \Delta\mathbf{r}) \rangle^{1/2} \\ C_2(\Delta\mathbf{r}) &= \langle I_d(\mathbf{r}) \rangle^{-1} \langle I_d(\mathbf{r} + \Delta\mathbf{r}) \rangle^{-1} \langle I_{ds}(\mathbf{r}) \rangle \langle I_{ds}(\mathbf{r} + \Delta\mathbf{r}) \rangle. \end{aligned} \quad (5.39)$$

We can sift $g_{ss}^{(1)}$ from (5.38), with use of (5.39), by separating the real (\Re) and imaginary (\Im) parts of the field correlations associated with C_{1j} as

$$\begin{aligned}
& \langle \tilde{I}_d(0) \tilde{I}_d(\Delta \mathbf{r}) \rangle \\
&= C_0(\Delta \mathbf{r}) \\
&+ 2 \left[C_{11}(\Delta \mathbf{r}) \Re\{g_{bs}^{(1)}(\Delta \mathbf{r})\} + C_{12}(\Delta \mathbf{r}) \Re\{g_{bs}^{(1)}(0)\} + C_{13}(\Delta \mathbf{r}) \right] \Re\{g_{ss}^{(1)}(\Delta \mathbf{r})\} \\
&+ 2 \left[C_{11}(\Delta \mathbf{r}) \Im\{g_{bs}^{(1)}(\Delta \mathbf{r})\} - C_{12}(\Delta \mathbf{r}) \Im\{g_{bs}^{(1)}(0)\} \right] \Im\{g_{ss}^{(1)}(\Delta \mathbf{r})\} \\
&+ C_2(\Delta \mathbf{r}) |g_{ss}^{(1)}(\Delta \mathbf{r})|^2 \\
&\equiv C_0(\Delta \mathbf{r}) + 2C_{1r}(\Delta \mathbf{r}) \Re\{g_{ss}^{(1)}(\Delta \mathbf{r})\} + 2C_{1i}(\Delta \mathbf{r}) \Im\{g_{ss}^{(1)}(\Delta \mathbf{r})\} \\
&+ C_2(\Delta \mathbf{r}) |g_{ss}^{(1)}(\Delta \mathbf{r})|^2,
\end{aligned} \tag{5.40}$$

where the C coefficients in general vary with $\Delta \mathbf{r}$ and

$$\begin{aligned}
C_{1r}(\Delta \mathbf{r}) &= \Re\{C_1(\Delta \mathbf{r})\} = C_{11}(\Delta \mathbf{r}) \Re\{g_{bs}^{(1)}(\Delta \mathbf{r})\} + C_{12}(\Delta \mathbf{r}) \Re\{g_{bs}^{(1)}(0)\} + C_{13}(\Delta \mathbf{r}) \\
C_{1i}(\Delta \mathbf{r}) &= \Im\{C_1(\Delta \mathbf{r})\} = C_{11}(\Delta \mathbf{r}) \Im\{g_{bs}^{(1)}(\Delta \mathbf{r})\} - C_{12}(\Delta \mathbf{r}) \Im\{g_{bs}^{(1)}(0)\}.
\end{aligned} \tag{5.41}$$

Equation (5.40) can thus be written as

$$\boxed{\langle \tilde{I}_d(0) \tilde{I}_d(\Delta \mathbf{r}) \rangle = C_0(\Delta \mathbf{r}) + 2\Re\{C_1^*(\Delta \mathbf{r})g_{ss}^{(1)}(\Delta \mathbf{r})\} + C_2(\Delta \mathbf{r})|g_{ss}^{(1)}(\Delta \mathbf{r})|^2.} \tag{5.42}$$

Equation (5.42) is our key result, and this will be used to consider various object and scatter regimes. While (5.42) is a compact expression relating measured intensity correlations to $g_{ss}^{(1)}$ and hence the object through (5.29), I_{ds} and $g_{bs}^{(1)}$ are not directly obtained from any measurement. Therefore, a tractable path requires approximations or assumptions to access the object function, O .

5.7 Correlation Length Scales, Object Scattering Regimes and Experimental Evidence

There are two important field correlations in (5.42) that carry information about the moving object, $g_{bs}^{(1)}(\Delta \mathbf{r})$ (that appears in $C_0(\Delta \mathbf{r})$ and $C_1(\Delta \mathbf{r}) = C_{1r}(\Delta \mathbf{r}) + iC_{1i}(\Delta \mathbf{r})$) and $g_{ss}^{(1)}(\Delta \mathbf{r})$. At this point, we understand little about $g_{bs}^{(1)}(\Delta \mathbf{r})$ other

than an expectation that it would reduce from unit magnitude to zero on the length scale of λ . From (5.21), there will also be a wavelength-scale decorrelation in $g_{ss}^{(1)}(\Delta\mathbf{r})$, supported by experimental data [20]. There is also a long range correlation where the light interacts with the object and a translated version at shared points, as Fig. 5.1 shows, and this forms a representation for macroscopic imaging. Therefore, we write

$$g_{ss}^{(1)}(\Delta\mathbf{r}) = g_{ss}^{(1)s}(\Delta\mathbf{r}) + g_{ss}^{(1)l}(\Delta\mathbf{r}), \quad (5.43)$$

where $g_{ss}^{(1)s}$ is the short-range correlation, with $\Delta\mathbf{r} \sim \lambda$, and $g_{ss}^{(1)l}$ is the long-range correlation that exists because the deterministic moving object modifies the background field at each point in space within the joint spatial support of the scatterer and the translated scatterer. We have experimental evidence that both $g_{ss}^{(1)s}(\Delta\mathbf{r})$ and $g_{ss}^{(1)l}(\Delta\mathbf{r})$ can be obtained with heavily scattered light [20].

We consider now forms of (5.42) in the large and small translation distance regimes, relative to λ , and in the weak and strong scatter contrast domains. This set of delineations relates to application domains for the theory.

5.7.1 $\Delta\mathbf{r} \gg \lambda$

With $|\Delta\mathbf{r}| \gg \lambda$, and from (5.23), we assume that $g_{bs}^{(1)}(\Delta\mathbf{r}) = 0$ and $g_{ss}^{(1)s}(\Delta\mathbf{r}) = 0$. The normalization yields $g_{ss}^{(1)}(0) = 1$ but $g_{ss}^{(1)l}(0) \neq 1$. In this situation of large object translation, relative to λ , we have from (5.42)

$$\langle \tilde{I}_d(0) \tilde{I}_d(\Delta\mathbf{r}) \rangle = C_0^l(\Delta\mathbf{r}) + 2\Re \{ C_1^{l*}(\Delta\mathbf{r}) g_{ss}^{(1)l}(\Delta\mathbf{r}) \} + C_2(\Delta\mathbf{r}) |g_{ss}^{(1)l}(\Delta\mathbf{r})|^2, \quad (5.44)$$

with

$$C_0^l(\Delta\mathbf{r}) = \langle I_d(\mathbf{r}) \rangle^{-1} \langle I_d(\mathbf{r} + \Delta\mathbf{r}) \rangle^{-1} \left\{ \langle I_{db} \rangle^2 + \langle I_{db} \rangle^{3/2} \langle I_{ds}(\mathbf{r}) \rangle^{1/2} 2\Re \{ g_{bs}^{(1)}(0) \} + \langle I_{db} \rangle \langle I_{ds}(\mathbf{r}) \rangle \right\} \quad (5.45)$$

$$\begin{aligned} C_{1r}^l(\Delta\mathbf{r}) &= C_{12}(\Delta\mathbf{r}) \Re \{ g_{bs}^{(1)}(0) \} + C_{13}(\Delta\mathbf{r}) \\ C_{1i}^l(\Delta\mathbf{r}) &= -C_{12}(\Delta\mathbf{r}) \Im \{ g_{bs}^{(1)}(0) \}, \end{aligned} \quad (5.46)$$

with $C_{12}(\Delta\mathbf{r})$ and $C_{13}(\Delta\mathbf{r})$ from (5.39).

5.7.2 $\Delta \mathbf{r} < \lambda$

Given the small scan distance, we assume that stationarity holds, leading to $\langle I_d(\mathbf{r}_0) \rangle \approx \langle I_d(\mathbf{r} + \Delta \mathbf{r}) \rangle$ and $\langle I_{ds}(\mathbf{r}_0) \rangle \approx \langle I_{ds}(\mathbf{r} + \Delta \mathbf{r}) \rangle$. The implication is that there is sufficient scatter. Therefore, in conjunction with (5.42), we have

$$\begin{aligned}
C_0(\Delta \mathbf{r}) &= \langle I_d(\mathbf{r}) \rangle^{-2} \left\{ \langle I_{db} \rangle^2 \right. \\
&\quad + 2 \langle I_{db} \rangle^{3/2} \langle I_{ds}(\mathbf{r}) \rangle^{1/2} \left[\Re\{g_{bs}^{(1)}(\Delta \mathbf{r})\} + \Re\{g_{bs}^{(1)}(0)\} \right] \\
&\quad + \langle I_{db} \rangle \langle I_{ds}(\mathbf{r}) \rangle 2 \Re\{g_{bs}^{(1)}(0) g_{bs}^{(1)}(\Delta \mathbf{r})\} \\
&\quad \left. + \langle I_{db} \rangle \langle I_{ds}(\mathbf{r}) \rangle \left[1 + |g_{bs}^{(1)}(\Delta \mathbf{r})|^2 \right] \right\} \\
C_{1r}(\Delta \mathbf{r}) &= C_{11} \Re\{g_{bs}^{(1)}(\Delta \mathbf{r})\} + C_{12} \Re\{g_{bs}^{(1)}(0)\} + C_{13} \\
C_{1i}(\Delta \mathbf{r}) &= C_{11} \Im\{g_{bs}^{(1)}(\Delta \mathbf{r})\} - C_{12} \Im\{g_{bs}^{(1)}(0)\} \\
C_2 &= \langle I_d(\mathbf{r}) \rangle^{-2} \langle I_{ds}(\mathbf{r}) \rangle^2,
\end{aligned} \tag{5.47}$$

where C_{11} , C_{12} , C_{13} and C_2 , defined in (5.39), are now assumed independent of scan distance over the scale of one wavelength. Consequently,

$$\begin{aligned}
C_{11} &= C_{12} \\
&= \langle I_d(\mathbf{r}) \rangle^{-2} \langle I_{db} \rangle^{1/2} \langle I_{ds}(\mathbf{r}) \rangle^{3/2} \\
C_{13} &= \langle I_d(\mathbf{r}) \rangle^{-2} \langle I_{db} \rangle \langle I_{ds}(\mathbf{r}) \rangle
\end{aligned} \tag{5.48}$$

With weak scatter, such as with a very small object, enforcing $\langle I_{ds} \rangle \ll \langle I_{db} \rangle$ and $\langle I_d \rangle \approx \langle I_{db} \rangle$. This approximation leads to

$$\begin{aligned}
C_0(\Delta \mathbf{r}) &= 1 + 2 \langle I_{db} \rangle^{1/2} \langle I_{ds}(\mathbf{r}) \rangle^{1/2} \left[\Re\{g_{bs}^{(1)}(\Delta \mathbf{r})\} + \Re\{g_{bs}^{(1)}(0)\} \right] \\
C_{11} &= C_{12} \\
&= \langle I_{db} \rangle^{-3/2} \langle I_{ds}(\mathbf{r}) \rangle^{3/2} \simeq 0 \\
C_{13} &= \langle I_{db} \rangle^{-1} \langle I_{ds}(\mathbf{r}) \rangle \simeq 0 \\
C_2 &= \langle I_{db} \rangle^{-2} \langle I_{ds}(\mathbf{r}) \rangle^2 \simeq 0.
\end{aligned} \tag{5.49}$$

Therefore, from (5.42),

$$\langle \tilde{I}_d(0) \tilde{I}_d(\Delta \mathbf{r}) \rangle \simeq 1 + 2 \langle I_{db} \rangle^{1/2} \langle I_{ds}(\mathbf{r}) \rangle^{1/2} \left[\Re \{ g_{bs}^{(1)}(\Delta \mathbf{r}) \} + \Re \{ g_{bs}^{(1)}(0) \} \right]. \quad (5.50)$$

Thus, this development provides access to the character of $g_{bs}^{(1)}(\Delta \mathbf{r})$ by allowing the extraction of $\langle I_{ds}(\mathbf{r}) \rangle^{1/2} \Re \{ g_{bs}^{(1)}(\Delta \mathbf{r}) \}$ from a series of measurements providing the left side of (5.50) and with a measurement of $\langle I_{db} \rangle$, without the moving object.

We note that it is of significance that measurements in this regime with heavy background random scatter could result in far-subwavelength information. This could be obtained from $g_{bs}^{(1)}(\Delta \mathbf{r})$, which varies with the object function. It is also available from $g_{ss}^{(1)s}$ and from (5.42).

5.7.3 $\langle I_{db} \rangle \gg \langle I_{ds} \rangle$

If the scattering object, large or small, is weakly scattering so that $\langle I_{db} \rangle \gg \langle I_{ds} \rangle$, we can approximate (5.42) as

$$\langle \tilde{I}_d(0) \tilde{I}_d(\Delta \mathbf{r}) \rangle = C_0(\Delta \mathbf{r}), \quad (5.51)$$

with

$$C_0(\Delta \mathbf{r}) = 1 + \frac{\left[\langle I_{ds}(\mathbf{r} + \Delta \mathbf{r}) \rangle^{1/2} 2 \Re \{ g_{bs}^{(1)}(\Delta \mathbf{r}) \} + \langle I_{ds}(\mathbf{r}) \rangle^{1/2} 2 \Re \{ g_{bs}^{(1)}(0) \} \right]}{\langle I_{db} \rangle^{1/2}}. \quad (5.52)$$

For $\Delta \mathbf{r} = 0$, (5.52) becomes

$$C_0(0) = 1 + \frac{\langle I_{ds}(\mathbf{r}) \rangle^{1/2} 4 \Re \{ g_{bs}^{(1)}(0) \}}{\langle I_{db} \rangle^{1/2}}. \quad (5.53)$$

Note that from (5.51) and (5.53), for an object that is weakly scattering, we can again access $\langle I_{ds}(\mathbf{r}) \rangle^{1/2} \Re \{ g_{bs}^{(1)}(0) \}$. However, this does not separate $\langle I_{ds}(\mathbf{r}) \rangle$ and $\Re \{ g_{bs}^{(1)}(0) \}$.

5.7.4 $\langle I_{db} \rangle \ll \langle I_{ds} \rangle$

With $\langle I_{db} \rangle \ll \langle I_{ds} \rangle$ and (5.42), we have the approximation

$$\langle \tilde{I}_d(0) \tilde{I}_d(\Delta \mathbf{r}) \rangle = C_2(\Delta \mathbf{r}) |g_{ss}^{(1)}(\Delta \mathbf{r})|^2. \quad (5.54)$$

5.8 Sensing and Imaging Methodology

5.8.1 Formation of Averages ($\langle \cdot \rangle$) with Experimental Data

The averaging process in our theory, $\langle \cdot \rangle$, is mathematically an average over scatterer reconfiguration. This means in forming $\langle \tilde{I}_d(0) \tilde{I}_d(\Delta \mathbf{r}) \rangle$ that the intensity is measured at the detector point (\mathbf{r}_d) with the object at \mathbf{r} (giving the p -th measurement as $I_{dp}(0)$) and at $\mathbf{r} + \Delta \mathbf{r}$ (resulting in $I_{dp}(\Delta \mathbf{r})$). Upon rearranging the background scatters according to a relevant density function, a set of sample products are obtained. Thus, the average with P measurements is formed as $\langle \tilde{I}_d(0) \tilde{I}_d(\Delta \mathbf{r}) \rangle = \frac{1}{P} \sum_{p=1}^P \tilde{I}_{dp}(0) \tilde{I}_{dp}(\Delta \mathbf{r})$, with P suitably large. It is not practical to form such averages experimentally. Even with moving background scatterers, the object of interest would need to be in two locations for each measurement with the background scatterer configuration being identical.

Experimentally, one can estimate $\langle \cdot \rangle$ using a camera image of the speckle intensity where the image domain is small enough for stationary statistics to hold [17,20,21,81]. In this case, each speckle spot needs to be adequately resolved, there needs to be a sufficient number of spots, and the regions imaged onto the camera should be small enough for the mean to be independent of position within a given image (but not necessarily as $\Delta \mathbf{r}$ is varied). Thus, the average is formed over the pixels of a camera. The requirement for independent samples can be met with a sufficient number of speckle spots. The sampling can be enhanced by using multiple reference positions (\mathbf{r}_p) and equivalent offsets ($\Delta \mathbf{r}$) [21]; this has also been done to form average over frequency [17]. The normalized intensity images associated with each measurement can thus be formed.

5.8.2 $\langle I_{db} \rangle = 0$: Aperture in a Screen

The simplest case corresponds to an aperture in a screen, where, with the object absent, there is no field on the detector side for a transmission measurement. From (5.42) or (5.54) we have

$$\langle \tilde{I}_d(0) \tilde{I}_d(\Delta \mathbf{r}) \rangle_{\text{ap}} = C_2(\Delta \mathbf{r}) |g_{ss}^{(1)}(\Delta \mathbf{r})|^2. \quad (5.55)$$

The subscript ap refers to the situation of an aperture in a screen [19]. With heavy background scatter or small total scan distance, $C_2(\Delta \mathbf{r}) = C_2$ is independent of $\Delta \mathbf{r}$. Through a renormalization, $|g_{ss}^{(1)}(\Delta \mathbf{r})|^2$ is then directly available from measured speckle intensity data. This has been the basis of imaging results presented using experimental data [20].

5.8.3 $\langle I_{db} \rangle \neq 0$: General Object

We consider the heavy scatter regime where the statistics are stationary over $\Delta \mathbf{r} \gg \lambda$, allowing us to write (5.44) as

$$\langle \tilde{I}_d(0) \tilde{I}_d(\Delta \mathbf{r}) \rangle = C_0^l + 2\Re \{ C_1^{l*} g_{ss}^{(1)l}(\Delta \mathbf{r}) \} + C_2 |g_{ss}^{(1)l}(\Delta \mathbf{r})|^2, \quad (5.56)$$

where within a scan distance corresponding to the joint support of the object and its translated self, it has been found that C_0^l , C_1^{l*} , and C_2 can be treated as constants [21]. The measured intensity data as a function of object position is then related to four real numbers and $g_{ss}^{(1)l}$, the object autocorrelation function. In principle, (5.56) can be solved and $g_{ss}^{(1)l}(\Delta \mathbf{r})$ obtained. Then, through a phase reconstruction process, the object function \tilde{O} can be retrieved from $g_{ss}^{(1)l}(\Delta \mathbf{r})$ based on (5.29). Experiments with macroscopic opaque patch elements have found C_1 to be small [21]. Consequently, in such situations, the second term in (5.56) can be ignored, C_0^l can be extracted from measured data, and (5.56) can be renormalized to scale $|g_{ss}^{(1)l}(0)| = 1$. These steps therefore provide access the normalized object autocorrelation function from (5.29).

5.9 Applications and Perspectives

Our compact, central result in (5.42) provides a new and fundamental description of intensity correlations over (moving object) space that persist over infinite length scales. In practice, the distances and levels of scatter become limited by the laser source energy and detector noise. Previous investigations into second order intensity correlations (see Refs. [67, 82–85] for a review) have identified contributors to the measured intensity correlation of $C_I(\Delta x) = \langle I(x_0)I(x_0 + \Delta x) \rangle$, where Δx represents the change in the correlation variable (e.g., frequency or wave-vector direction) and the brackets $\langle \dots \rangle$ represent the ensemble average. $C_I(\Delta x)$ has been decomposed into three terms, short-range correlations $C_1(\Delta x)$, long-range correlations $C_2(\Delta x)$, and infinite-range correlations $C_3(\Delta x)$ [41]. Note that we have preserved the notation in the references indicated for consistency [41], and that the definition of C_1 and C_2 is not the same as in the development given in this work. Each of these correlations may contribute to the measured correlation, and they have been weighted by the dimensionless quantity g (dimensionless conductance) according to $C_I(\Delta x) = C_1(\Delta x) + g^{-1}C_2(\Delta x) + g^{-2}C_3(\Delta x)$. For most optical experiments involving a slab geometry, $g \gg 1$ is typical [86], thus making the contribution of the long- and infinite-range correlations negligible. Our work provides another dimension for the infinite range correlations for situations that pertains to a randomly scattering slab where the thickness can in principle approach infinity.

A number of fundamental assumptions were made in the development of our theory that impact applications: we assume that the statistics from a set of camera images will be a good indicator of an average formed from rearrangements of the environmental scatterers; there is natural or controlled motion of the object of interest; the background scattering environment is assumed to be static within the acquisition of speckle images; and, most importantly, we have required the statistics of the detected speckle field to exhibit a circular Gaussian distribution, required for use of Reed’s moment theorem [16]. We address each of these requirements.

In an experiment, averages would be formed with camera speckle images that access random intensity information over space (or angle). The statistics from the camera image are expected to be a good representation provided each speckle is spatially resolved and there are enough independent samples. Our experience with reasonably heavily scattering media is that a spot of about 1 mm can have approximately a constant mean intensity, thereby providing stationary statistics in the camera image [4, 17–20, 46, 87]. A 4-F lens system with an aperture in the Fourier domain provides separate control of the speckle size. There is obviously a trade-off between speckle size and number of speckle spots. Measurements are made through a polarizer. Negative exponential intensity statistics indicate that the speckle images are satisfactory, and that the fields are zero-mean-circular Gaussian. Laser light with adequate coherence is also required (to achieve satisfactory statistics), and this requirement is a function of the amount of background scatter.

Various physical situations involve an object that is moving naturally. One example is *in vivo* blood vessel constituents. In other applications, motion could be induced using a translational stage. This may be appropriate in material inspection, for instance. Regardless, prior information on the motion of the object during the acquisition of speckle images is needed to apply this approach which means the positional or velocity information of the unknown moving object needs to be inferred through some complimentary method, such as temporal decorrelation or the Doppler shift [54], or localization based on the diffusion model [55]. The dimensionality of any sensing and imaging result is commensurate with that of the object motion. For motion other than linear translation, we foresee that a similar type of theory may be possible. Given enough prior information about the motion of the object, the experimentally-measured correlation could potentially be separated to different types of object motion, such as translation and rotation, and analyzed for useful sensing and imaging.

The need for stationary (static) background scatterer positions is perhaps the most severe restriction. Natural settings may involve motion of the scatterers, such as with

aerosols. It is assumed that displacement of background scatterers with the motion of the object of interest can be neglected. Generally, the stationary background scatterer requirement implies that this motion is negligible during the measurement period over which the object is moving. Alternatively, the implication is that intensity decorrelation due to the motion of the randomly located background scatterers can be accounted for in a calibration and hence known from prior information. This constraint also relates to object size or speed, which has a detector signal-to-noise ratio implication.

An amount of scatter producing developed Gaussian field statistics is assumed. This can be met with a random medium having a thickness of one transport length, the distance for photon momentum randomization, or more. Heavier scatter, such that the mean intensity does not vary appreciably with object position over the measurement provides a simplification, and can lead to approximating C_0 , C_1 and C_2 as constant for $\Delta \mathbf{r}$ about the moving object's size in our development in Sect. 5.8.

We have been able to reconstruct images of macroscopic (mm-scale) objects, both apertures of rather complex shapes and also black patches by obtaining speckle images as a function of translated object position and applying the theory of Sect. 5.8(A) [21]. This is achieved by assuming that C_0 , C_1 , and C_2 are constants, which allows them to be determined by fitting the measured data [21]. This provided access to $g_{ss}^{(1)l}$ and hence the object autocorrelation, from which phase retrieval yielded the object to quite high precision. The principle is that correlations exist within the joint support and the wavelength-scale correlation, $g_{ss}^{(1)s}$, is neglected. In the general situation where these coefficients are spatially dependent, inversion becomes ill-posed. Consequently, prior information would be needed or constraints imposed. Recently, we have also obtained experimental results that support using the ratio between C_0^l and C_2^l in (5.56) to qualitatively compare the relative scattering strengths of the moving object and the scattering environment. This suggests that various measures based on our general result in (5.42) could be of practical importance. While the resolution could in principle approach wavelength scale in this macroscopic regime,

in practice it is limited by scanning precision and other practical aspects of making such measurements.

The experimental evidence for super-resolution sensitivity in a speckled field is compelling [20]. This subwavelength length-scale information is contained within $g_{ss}^{(1)}$, specifically $g_{ss}^{(1)s}(\Delta\mathbf{r})$, and likely $g_{bs}^{(1)}(\Delta\mathbf{r})$ (although there is currently no experimental information relevant to the character of $g_{bs}^{(1)}(\Delta\mathbf{r})$). A combined numerical field study and experiments with nanoparticles could shed light on these functions and may provide a means to extract object parameters of relevance, hence providing sensing and perhaps even imaging on this length scale. The achievement of far-subwavelength object information with motion in a speckled field is analogous to an earlier proposal for motion in structured illumination achieved by two interfering beams [78]. The distinction in the case of the speckled field is that the field is generally unknown and hence a forward model and conventional computational imaging approaches cannot be applied.

More generally, our method could allow communication in a cluttered environment. Consider a moving transmitter that sends an identical set of signals from a series of spatial positions. This information could be in principle extracted in a manner similar to how imaging is accomplished. Again, the principle is correlated information that survives the averaging process with multiply-scattered light. In this case, temporal or multiple frequency data would be extracted. There are of course details to be investigated as to how a protocol for this communication arrangement would be implemented, but the principle we have described should be applicable. This may also carry over to quantum key distribution in the presence of clutter [88].

Ghost imaging involves entangled or correlated photons [89]. Speckle can occur [90] and achieving high contrast to noise control is important [91, 92]. It may be possible to utilize object motion to enhance the robustness of ghost imaging in a scattering environment. In fact, moving objects have been considered in ghost imaging [93] and this could be extended to heavily scattering media with our approach. With regard to energy-time entangled photons in scattering media, correlated detection

(in the Hanbury Brown and Twiss sense) or detection with a nonlinear crystal [94] provides temporal gating that could be useful in scattering media. With a moving entangled photon source in a scattering medium, information can be added by position control that could be interesting in applications.

Finally, fluorescence (or Förster) resonance energy transfer (FRET) is a non-radiative energy transfer process between donor and acceptor molecules spatially separated by a distance usually between 1-10 nm that results in a decrease in the lifetime and quantum yield of the donor in the presence of the acceptor [95]. Measurement of FRET through lifetime modification has become important in molecular biology [96] and has been shown possible for *in vivo* applications [97,98]. With suitable labeling, FRET can provide key information about protein folding, relevant for many major diseases. Generally, the change of lifetime is represented as a donor-acceptor distance using classical dipole-dipole coupling theory [95]. It may be possible to use a coherent method based on absorption and motion along the lines we have described to separately determine the distance (which is typically several nanometers).

5.10 Conclusion

We have presented a rigorous theory for imaging based on speckle pattern correlations over object position. This leads to various sensing and imaging opportunities using coherent light in scattering media. It may be possible to exploit natural motion in environmental sensing situations where multiple scatter occurs. If the motion of the object of interest were fast relative to the background scattering media, then the situation would conform to the theory described. It may also be possible to calibrate for decorrelation due to the background, provided there is adequate sensitivity to the moving object to be imaged. An important application domain is *in vivo* imaging without contrast agents, such as of blood cells in capillaries. In this case, the local velocity may be constant over the micron length scales required. While the corresponding translation is 1D, 3D imaging may be possible with constraints. Accessing

far-subwavelength information is an intriguing direction. This is relevant in finding defects in semiconductor device processing using optical inspection. The wafer can be precisely positioned but traditional methods are diffraction-limited and hindered by speckle produced due to surface roughness and complicated 3D structures. It is possible that the presence of defects may be determined by using speckle intensity correlation over the wafer position. In weakly scattering situations, such as in microscopy where super-resolution would be value, the speckle could be created by a diffusing screen and the object of interest, cells for example, translated in this structured field, allowing intensity images to be captured as a function of object position.

6. ENHANCED COHERENT SENSING USING A SCATTERING ANALYZER VIA SPECKLE CORRELOGRAPHY

6.1 Introduction

While speckle can be a nuisance in many coherent applications, metrology methods that exploit naturally occurring speckle patterns, such as those from optically rough surfaces, are able to access useful information about remote objects. For example, speckle interferometry and electronic speckle pattern interferometry [99–102] employ a fringe analysis of interferograms to measure the displacement of a rough surface, and can be used in stress, strain, and vibration measurement [103]. However, its high sensitivity is achieved by intricate interferometric setup and sophisticated phase unwrapping post-processing. Speckle image correlation algorithms are able to detect the object’s deformation and displacement using the cross-correlation or the difference between speckle images [23] because the recorded speckle patterns are sensitive to displacement and deformation gradients. This correlation-based metrology approach is not limited to electromagnetic waves: the correlation between ultrasonic speckle patterns can also be used to detect remote displacement [104].

By adding a ground glass diffuser or an acrylic slab (filled with embedded TiO_2 scatterers) between the subject and the detector, we found greater sensitivity to the subject’s in-plane displacement in the cross correlation between speckle images, and the enhancement in sensitivity increases as the analyzer’s scattering strength increases.

In the diffusive regime, where there is enough scatter to fully randomize the multiply scattered photons, the detected electric fields exhibit zero-mean circular Gaussian statistics [3]. We have previously shown that, in this heavily scattering regime, it is

possible to reconstruct an obscured field [18] or an embedded object [20, 21] by forming correlations over the positions of the moving field or the moving object averaged over scatterer configurations. Random aperiodic structures, such as the scattering analyzers used in our study, exhibit interesting field control properties that are dependent on the macroscopic features of the structure [105]. For a slab of multiply scattering material, the distribution of the eigenvalues of its transmission matrix has been described as bimodal by random matrix theory (RMT) [24, 106, 107] where most eigenchannels are either fully “closed” or fully “open”. According to RMT, the distribution becomes more bimodal as the thickness of the scattering medium increases. Realistic setups that involve a finite-sized detector imply an incomplete capture of all eigenchannels, so that the bimodal description is only accurate for the relatively small eigenvalues [108], so that there are more modes concentrated around eigenvalues close to zero for a thicker slab. Simulations have verified that and as a result, the few “open” eigenchannels account for a bigger proportion of the total transmittance for a thicker scattering slab [106].

We show that the averaged speckle intensity correlation over subject movement decorrelates faster in the presence of the scattering analyzer and that the more strongly scattering the analyzer, the faster the decorrelation. To understand the enhanced sensitivity, we relate speckle intensity correlation to the normalized transmission eigenvalues of the scattering analyzer and provide finite-element-method (FEM) simulation results as corroborating evidence.

6.2 Theory

Assuming zero-mean circular Gaussian statistics for the detected field, we can apply Reed’s moment theorem [16], and write the ensemble-averaged intensity correlation in terms of the correlation of the detected fields (through a polarizer) Φ_d at different object positions \mathbf{r} and $\mathbf{r} + \Delta\mathbf{r}$,

$$\begin{aligned} & \langle \tilde{I}(\mathbf{r}_d; \mathbf{r}) \tilde{I}(\mathbf{r}_d; \mathbf{r} + \Delta \mathbf{r}) \rangle \\ &= \frac{|\langle \Phi_d^*(\mathbf{r}_d; \mathbf{r}) \Phi_d(\mathbf{r}_d; \mathbf{r} + \Delta \mathbf{r}) \rangle|^2}{\langle I(\mathbf{r}_d; \mathbf{r}) \rangle \langle I(\mathbf{r}_d; \mathbf{r} + \Delta \mathbf{r}) \rangle}, \end{aligned} \quad (6.1)$$

where \mathbf{r}_d is the detector position which is fixed, and the intensities are normalized so that $\tilde{I} = (I - \langle I \rangle) / \langle I \rangle$. It is noted that the correlation computed inside $\langle \cdot \rangle$ is the inner product between two intensity measurements or two complex fields involving all of the spatial detector pixels. Hence, statistically, $\langle \cdot \rangle$ represents an averaging process. Moreover, we average the correlation coefficients associated with the same $\Delta \mathbf{r}$. As a result, the ensemble-averaged correlation depends only on $\Delta \mathbf{r}$, and \mathbf{r} is just a reference object position. In this particular study, the mean intensity does not change much over different object position, so $\langle I(\mathbf{r}_d; \mathbf{r} + \Delta \mathbf{r}) \rangle \approx \langle I(\mathbf{r}_d; \mathbf{r}) \rangle$. If the variation in intensity over $\Delta \mathbf{r}$ is significant (for a very weakly scattering analyzer), $\langle I(\mathbf{r}_d; \mathbf{r} + \Delta \mathbf{r}) \rangle$ can be easily computed and incorporated in the analysis. It is noted that using averaged cross-correlations is our default choice from our previous speckle intensity correlation studies, which will result in a monotonic decreasing correlation given enough averaging samples, easier for comparison.

Through the Fourier transform, we can write any $\Phi_d(\mathbf{r}_d)$ in k-space as $\phi_d(\mathbf{k}_d)$, where \mathbf{k}_d represents the corresponding k-space Fourier pair of \mathbf{r}_d . Given that the discrete Fourier transform is represented by a unitary matrix operator, the ensemble-averaged correlation is preserved when represented in k-space, so that

$$\langle \phi_d^*(\mathbf{k}_d; \mathbf{r}) \phi_d(\mathbf{k}_d; \mathbf{r} + \Delta \mathbf{r}) \rangle = \langle \Phi_d^*(\mathbf{r}_d; \mathbf{r}) \Phi_d(\mathbf{r}_d; \mathbf{r} + \Delta \mathbf{r}) \rangle. \quad (6.2)$$

ϕ_d is related by the transmission matrix, \mathbf{t} , in k-space, to the plane wave decomposition of the field incident on the speckle analyzer, ϕ_i (Φ_i in the space domain). The singular value decomposition of the transmission matrix of the scattering analyzer, \mathbf{t} , gives

$$\mathbf{t} = \mathbf{U} \Sigma \mathbf{V}^*, \quad (6.3)$$

where Σ is a diagonal matrix with non-negative real numbers on the diagonal, which are the singular values, σ_i , for i -th eigenchannel. \mathbf{V}^* and \mathbf{U} are unitary operators mapping the input wavevector channels (\mathbf{k}_i) to eigenchannels (\mathbf{k}'_i) and eigenchannels (\mathbf{k}'_d) to output wavevector channels (\mathbf{k}_d), respectively. The transmission eigenvalues described by RMT are $T_i = \sigma_i^2$, and their corresponding diagonal matrix is \mathbf{T} . Hence, we can then write,

$$\begin{aligned}\phi_d(\mathbf{k}_d) &= \mathbf{t}\phi_i(\mathbf{k}_i) \\ \phi_d(\mathbf{k}_d) &= \mathbf{U}\Sigma\mathbf{V}^*\phi_i(\mathbf{k}_i) \\ \phi'_d(\mathbf{k}'_d) &= \Sigma\phi'_i(\mathbf{k}'_i),\end{aligned}\tag{6.4}$$

where $\phi'_d = \mathbf{U}^{-1}\phi_d(\mathbf{k}_d)$ and $\phi'_i = \mathbf{V}^*\phi_i(\mathbf{k}_i)$ are the detected field and the incident field represented in the eigenspace.

We write the spatial field correlation in the wavevector eigen space,

$$\begin{aligned}\langle\Phi_d^*(\mathbf{r}_d; \mathbf{r})\Phi_d(\mathbf{r}_d; \mathbf{r} + \Delta\mathbf{r})\rangle &= \langle\phi_d^*(\mathbf{k}_d; \mathbf{r})\phi_d(\mathbf{k}_d; \mathbf{r} + \Delta\mathbf{r})\rangle \\ &= \langle\phi_d'^*(\mathbf{k}'_d; \mathbf{r})\phi_d'(\mathbf{k}'_d; \mathbf{r} + \Delta\mathbf{r})\rangle \\ &= \langle(\Sigma\phi'_i(\mathbf{k}'_i; \mathbf{r}))^*\Sigma\phi'_i(\mathbf{k}'_i; \mathbf{r} + \Delta\mathbf{r})\rangle \\ &= \langle\phi_i'^*(\mathbf{k}'_i; \mathbf{r})\mathbf{T}\phi_i'(\mathbf{k}'_i; \mathbf{r} + \Delta\mathbf{r})\rangle.\end{aligned}\tag{6.5}$$

Submitting (6.5) in to (6.1), we have

$$\begin{aligned}\langle\tilde{I}(\mathbf{r}_d; \mathbf{r})\tilde{I}(\mathbf{r}_d; \mathbf{r} + \Delta\mathbf{r})\rangle &= \frac{|\langle\phi_i'^*(\mathbf{k}'_i; \mathbf{r})\mathbf{T}\phi_i'(\mathbf{k}'_i; \mathbf{r} + \Delta\mathbf{r})\rangle|^2}{\langle I(\mathbf{r}_d; \mathbf{r})\rangle\langle I(\mathbf{r}_d; \mathbf{r} + \Delta\mathbf{r})\rangle} \\ &= \frac{|\langle\phi_i'^*(\mathbf{k}'_i; \mathbf{r})\tilde{\mathbf{T}}\phi_i'(\mathbf{k}'_i; \mathbf{r} + \Delta\mathbf{r})\rangle|^2}{\langle I_i(\mathbf{r}_d; \mathbf{r})\rangle\langle I_i(\mathbf{r}_d; \mathbf{r} + \Delta\mathbf{r})\rangle},\end{aligned}\tag{6.6}$$

where $\tilde{\mathbf{T}} = \frac{\mathbf{T}}{\bar{T}}$ is the diagonal matrix of the normalized transmission eigenvalues with \bar{T} representing the mean transmission eigenvalue. In (6.6), we have expressed the detected intensity cross-correlation as a function of the cross-correlation of the field and the intensity incident on the scattering analyzer at different positions of the

remote diffusive object of interest. For free space, the eigenchannels are all open so the matrix $\tilde{\mathbf{T}}$ can be treated as the identity matrix \mathbf{I} .

Therefore, the averaged speckle intensity correlation is directly linked to the normalized transmission eigenvalues of the transmission matrix of the analyzer. According to RMT, for a slab-geometry scattering medium and a finite-sized detector, the thicker the scattering slab, the few “open” eigenchannels account for a bigger proportion of the total transmittance, and there are more “closed” channels [106]. Hence, with a smaller number of propagating eigenchannels for the thicker analyzer slab, the change in speckle pattern will be dominated by a few “open” channels only, which will result in a faster averaged decorrelation, enhancing the cross-correlation’s sensitivity to any small system change.

6.3 Experiment

The experimental setup is shown in Fig. 6.1, where a fixed scattering analyzer is placed between the moving diffusing object of interest and the camera. A 59-mW, 850-nm laser diode with a linewidth less than 10 MHz is used for illumination, producing a laser beam on the moving diffusing object that is about 0.4 mm in diameter. Referring to Fig. 6.1, the moving object used is a diffusive acrylic slab, and a stage is used to move the slab in the y direction at sub-wavelength step of 476 nm. The scattering analyzers used are a single ground glass of 1500 grit (10 cm \times 10 cm \times 0.2 cm), a 3-mm-thick acrylic slab and a 6-mm-thick acrylic slab. The scattering slabs (14 cm \times 14 cm), are made of commercial clear acrylic with negligible optical absorption and embedded with TiO_2 scatterers having a mean diameter of 50 nm. The reduced scattering coefficient of the scattering acrylic slabs is about 4 cm⁻¹. The moving slab and the scattering analyzer are separated by a distance about 5 cm. An area of approximately 1.8 mm by 1.8 mm on the back of the second scattering layer is imaged by a Photometrics Prime sCMOS (2048 \times 2048 pixels) using magnifying optics. The 4f system is used to regulate speckle size at the camera so that it is sufficiently

large relative to the camera pixel size and the polarizer is used so that we only collect light that is polarized in one direction.

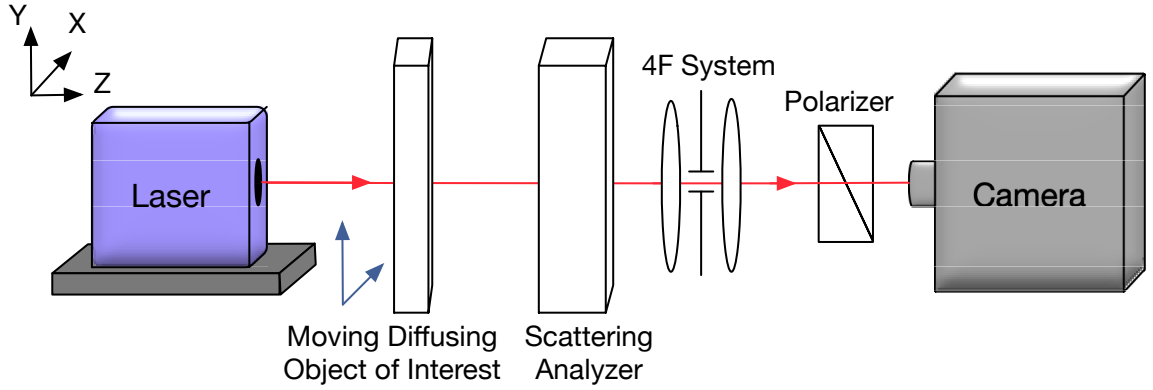


Fig. 6.1. Experimental setup. The diffusing object of interest was translated in the transverse plane, along the y axis.

The averaged speckle intensity correlation is plotted in Fig. 6.2 for the cases of using no analyzer, 1 ground glass, a 3-mm-thick acrylic slab and a 6-mm-thick acrylic slab, while keeping the rest of experimental configuration the same. The moving object used is a 3-mm-thick acrylic slab. We see that, as the scattering strength of the analyzer increases, the intensity correlation decorrelates faster. In other words, a thicker analyzer is able to detect subwavelength displacement (Δy) with greater sensitivity. To illustrate, we tabulate the first two correlation data points for each case in Table. 6.1 for comparison. We see that, by using a thicker analyzer, the decorrelation is drastically faster, even for sub-pixel and subwavelength displacement.

The sizes of the speckles exiting the analyzer are estimated to be consistent throughout our experiments, around 15 pixels in diameter, measured using the full-width-at-half-maximum of the main peak of the autocorrelation of example speckle patterns.

It is noted that the incident field correlation can also be influenced by the configuration of the experiment, such as the scattering strength of the moving diffuser

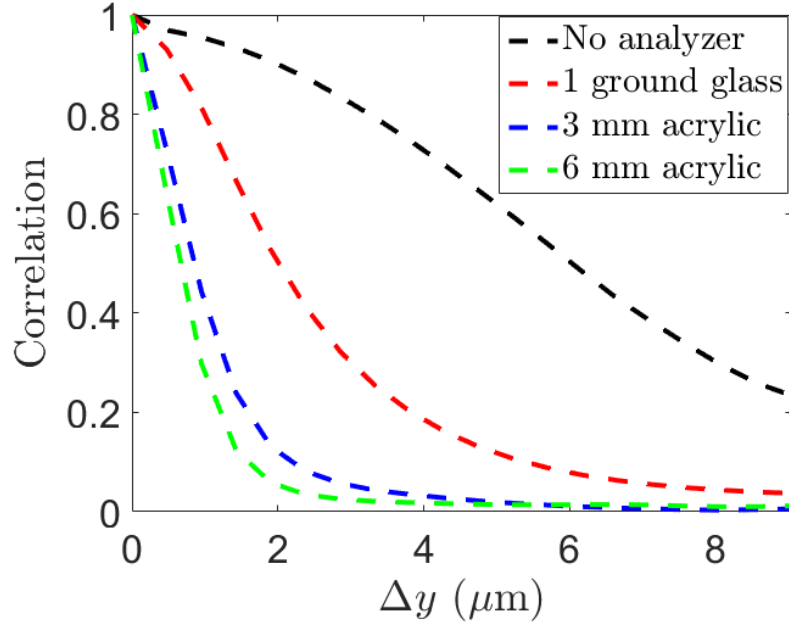


Fig. 6.2. The averaged correlation over the translation of object decreases at different rate for different analyzer configuration. The more scattering the analyzer is, faster the decorrelation becomes. With a thicker analyzer, we are able to sense sub-wavelength (< 850 nm) translation of the diffusing object.

and the separation distance between the analyzer and the moving object. Referring to Fig. 6.3(a), while the correlation over the translation of object decreases faster for

Table 6.1.

Tabulation of the first two data points in Fig. 6.2, for translations of 476 nm and 952 nm.

Correlation at $\Delta y =$	476 nm	952 nm
No Analyzer	0.9694	0.9550
1 Ground Glass	0.9305	0.8134
3 mm Acrylic	0.7273	0.4431
6 mm Acrylic	0.6401	0.2978

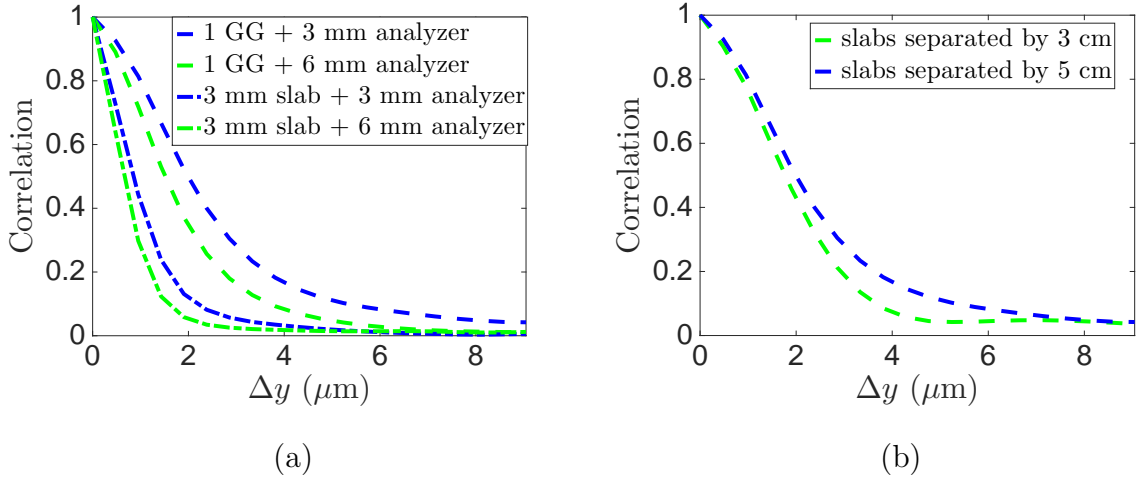


Fig. 6.3. Experimental configurations other than the analyzer thickness can also affect sensitivity by varying the speckle spot size incident on the analyzer, which is a function of the area of the speckle spread and the distance between the diffusing object and the analyzer [3]. (a) The more-scattering 3 mm thick acrylic slab produces faster decorrelation when compared to 1 moving ground glass (1 GG), as the larger spread of speckle intensity exiting the acrylic slab result in larger speckle spots incident on the analyzer, producing faster decorrelation. (b) The rate of speckle decorrelation increases for a shorter separation between the diffusing moving object (1-ground-glass slab) and the analyzer(3-mm-thick acrylic slab).

the more strongly scattering analyzer, the scattering strength of the diffusing object also plays a factor. The more-scattering 3 mm thick acrylic slab produces faster decorrelation when compared to 1-ground-glass (1 GG) as the moving diffuser. In Fig. 6.3(b), the rate of speckle decorrelation increases for a shorter separation between the diffusing moving object (1 ground glass slab) and the analyzer(3-mm-thick acrylic slab). These observations can be explained using the different sizes of the speckle spots incident on the scattering analyzer, which increase when the speckle intensity spread exiting the diffusive object increases and when the distance between the object and the analyzer increases [3]. The smaller the size of the speckle spots incident on the scattering analyzer, a larger change in speckle pattern is expected given the same amount of object translation.

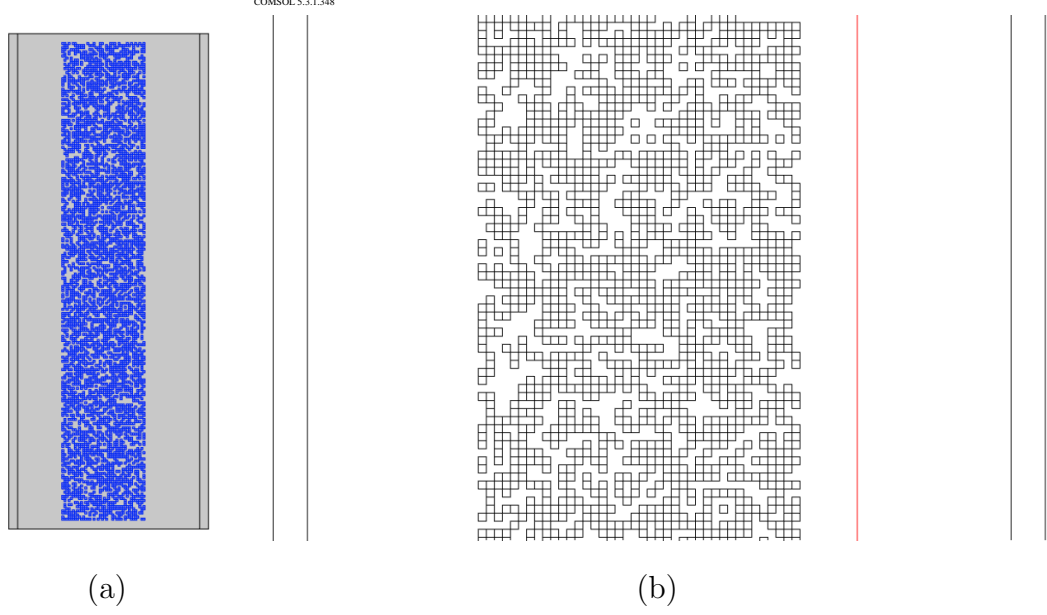


Fig. 6.4. Numerical simulation geometry. (a) The overall geometry of the simulations: the center of the domain is the $46\text{-}\mu\text{m}$ -long slab, consisting of 200-nm square scatterers (in blue) randomly distributed in the space with a fill factor of 50%. (b) The zoomed-in view of the geometry, with the detection plane of $42.6\text{ }\mu\text{m}$ labeled by the red line, collecting the total field at half wavelength away from the slab's right side. The wavelength used for the plane wave propagating from the left to the right is chosen as 850 nm .

6.4 Simulation

In our simulation, we focus on analyzing the distribution of the normalized eigenvalues of the transmission matrices for scattering layers of the same material but different thickness. The simulated analyzer is of a slab geometry and is made of randomly distributed small square scatterers ($200\text{ nm} \times 200\text{ nm}$), with a fill factor of 50%. The scatterer material has a dielectric constant of 5. The slab's vertical length is fixed at $46\text{ }\mu\text{m}$ and the thickness is varied ($4\text{ }\mu\text{m}$, $6\text{ }\mu\text{m}$, $8\text{ }\mu\text{m}$). The geometry for the $8\text{ }\mu\text{m}$ thick slab can be seen in Fig. 6.4(a) and (b). The left and right of the simulation domain are perfect matched layers while the top and bottom follow period boundary condition.

Referring Fig. 6.4(a), a plane wave with the wavelength of 850 nm (TE field that only has y component, which is perpendicular to the plane of Fig. 6.4) is incident onto the scattering slab from the left. A detector plane is chosen to be at half wavelength away from the right side of the slab (red line on Fig. 6.4(b)), where the total field is recorded. For the 46 μm -long slab, only the central section of 42.6 μm -long is used to mitigate edge effect associated with the slab geometry. The data collected are at 100 points, uniformly spread along evenly over the 42.6 μm long detector plane. There are 100 incident angles for the plane waves spanning from -1.0429 rad (-59.75 degree) to 1.0429 rad (59.75 degree). The range of incident angles are chosen so that the associated wavevectors are within the propagating spectrum given the wavelength.

Each of the 100 incident fields (each has its own wavevector, \mathbf{k}_{in}) produces the output field. The output field collected in space is then Fourier transformed to spatial frequency space (\mathbf{k}_{out}), where only the propagating spectrum (also 100 wavevectors) is selected. A transmission matrix (100 \times 100) relating \mathbf{k}_{in} and \mathbf{k}_{out} can be then mapped out. However, due to total internal reflection, evident in the very large imaginary component of the output field in the spatial frequency space, the largest angles close to the two extremes are discarded, we end up having a 67 \times 67 transmission matrix, \mathbf{t} .

In order to study how analyzer thickness impacts transmission eigenvalue distribution, we generate 50 independent instances of random analyzer for each thickness (150 transmission matrices in total), and compute each analyzer's normalized eigenvalues, \tilde{T} . Combining all 50 collection of \tilde{T} , we observe the collective histogram for each analyzer thickness. In Fig. 6.5, we plot the curves formed using the histogram data of the collective normalized transmission eigenvalues for different slabs in curves of 30 bins for comparison. The normalization is against the mean transmittance of each slab, so that the unity on the x-axis equals to the mean of all transmission eigenvalues of the corresponding slab, \bar{T} . When the slab is thicker, there are more “closed” channels with \tilde{T} close to zero, and the “open” channels carry a larger proportion of

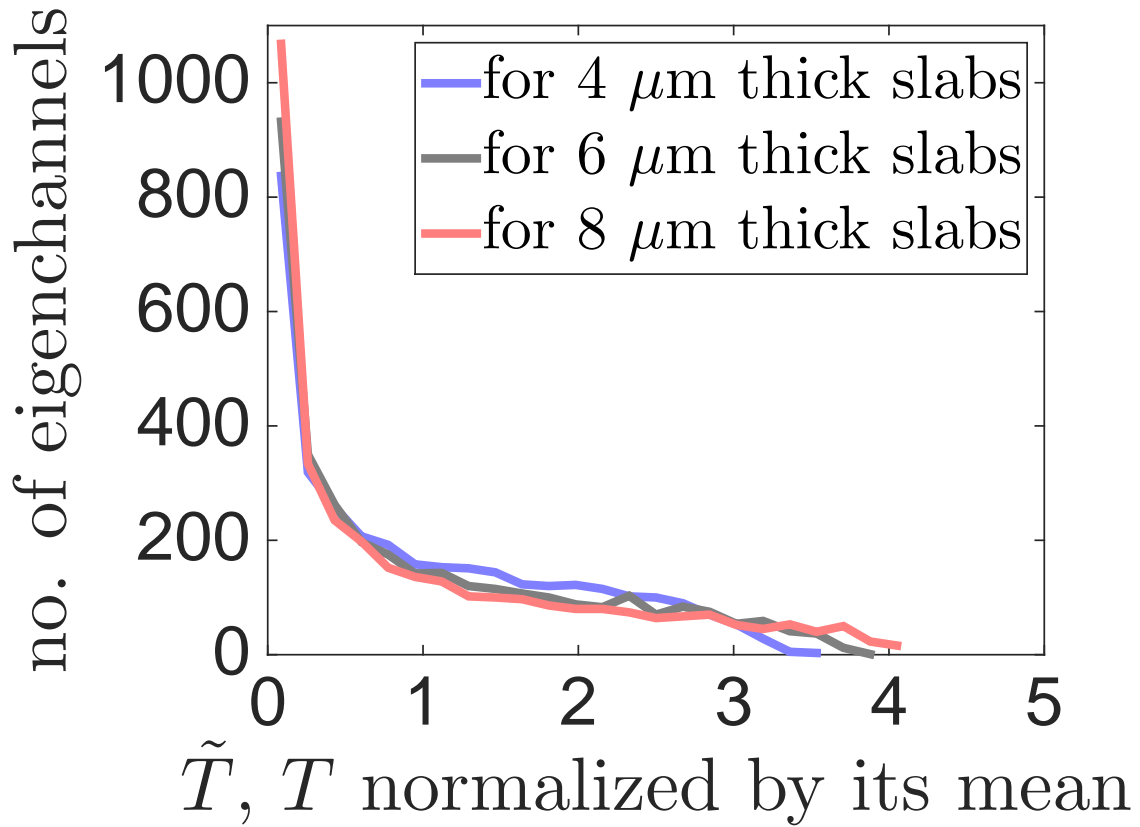


Fig. 6.5. The collective histogram distribution (plotted as a curve of 30 bins) of the normalized transmission eigenvalues, \tilde{T} , of the transmission matrices for slabs of randomly distributed scatterers of different thickness. Each histogram contains 50 independently generated random configurations of the scattering slab of either 8 μm , 6 μm , or 4 μm . The x-axis rescaled so that 1 is the mean of the transmission eigenvalues of an analyzer, \bar{T} . For a thicker slab, there are more “closed” channels (\tilde{T} close to 0), and the few “open” channels are more transmitting, carrying a larger proportion of the power (maximum \tilde{T} is larger).

the transmitted signal as indicated by the larger maximum \tilde{T} value, in agreement with existing theory [108] and simulation [106].

6.5 Conclusion

Using averaged speckle intensity correlation as a metric to detect displacement of diffuse object, we have demonstrated experimentally adding a scattering analyzer in front of the detector greatly enhances the rate of decorrelation, improving sensitivity, capable of detecting subwavelength in-plane displacement of a remote diffuse object. The more strongly scattering the analyzer is, the higher the sensitivity. We have shown that the speckle intensity correlation is directly related to the normalized transmission eigenvalues of the scattering analyzer’s transmission matrix. Through simulations, we have shown that, when the scattering analyzer is thicker, the normalized transmission eigenvalues have more “closed” channels and a few “open” channels that carry a larger proportion of the transmitted signal.

This novel remote sensing approach by adding a scattering analyzer can be applied to the measurement of properties such as displacement and thermal expansion. It is cheap and simple to implement, and also offers comparable if not superior remote sensitivity that is at least an order of magnitude below wavelength scale. The analysis we provided relates the normalized eigenvalues of the transmission matrix of the scattering analyzer to the intensity correlation metric used opening up opportunities in the design and calibration of a better-performing scattering analyzer.

7. SUMMARY

Methods for sensing and imaging a hidden object moving inside a heavily scattering environment have been presented. Through the use of spatial speckle intensity correlations over object position, a significant amount of information about the object can be obtained despite the presence of heavy scatter. A theory was developed that describes the spatial speckle intensity correlation over object position in terms of the embedded object's relative refractive index, with a simulated image reconstruction using measurements from an experiment. The theory was then expanded to accommodate a more-weakly-scattering and absorptive object. Biological tissue was used as a scattering material, and phase retrieval was used for image reconstruction to demonstrate the feasibility and wide applicability of our approach for practical imaging. Equipped with experimental insights on speckle intensity correlation over object motion, including its sensitivity to the relative scattering strengths of the moving object and the surrounding environment, a general mathematical model was developed that can lead to the sensing and imaging of a small object or features with super-resolution. This general theory forms the basis of a method to pursue imaging applications based on spatial speckle intensity correlations with complicated object motion such as rotation and deformation, as similar theoretical treatment is expected to apply. For the approach, information about the object motion is required, and this can be obtained by some other complementary methods. Generally, speckle intensity correlation over object position provides a way to access the optical properties of moving objects embedded within heavily scattering media that would not be accessible otherwise, and possibly capable of revealing super-resolution features, beyond the limit of conventional optical methods.

Related to the study of speckle intensity correlation over object motion, a technique that can enhance the sensitivity of optical metrology was introduced. By placing

a static scattering layer in front of the detector, we showed improved remote sensitivity, capable of detecting subwavelength in-plane displacement of a remote diffuse object. This simple and inexpensive modification can be used as the design principle for a wide range of optical sensors, useful for high-sensitivity temperature sensing and for remote sensing, such as in material inspection.

REFERENCES

REFERENCES

- [1] J. W. Goodman, *Statistical Optics*. New York, Wiley-Interscience, 1985.
- [2] J. G. Abbott and F. L. Thurstone, “Acoustic speckle: Theory and experimental analysis,” *Ultrasonic Imaging*, vol. 1, no. 4, pp. 303–324, 1979.
- [3] J. W. Goodman, *Speckle Phenomena in Optics: Theory and Applications*. Roberts and Company Publishers, 2007.
- [4] J. D. McKinney, M. A. Webster, K. J. Webb, and A. M. Weiner, “Characterization and imaging in optically scattering media by use of laser speckle and a variable-coherence source,” *Opt. Lett.*, vol. 25, no. 1, pp. 4–6, Jan 2000.
- [5] A. B. Parthasarathy, W. J. Tom, A. Gopal, X. Zhang, and A. K. Dunn, “Robust flow measurement with multi-exposure speckle imaging,” *Opt. Express*, vol. 16, no. 3, pp. 1975–1989, Feb. 2008.
- [6] D. J. Pine, D. A. Weitz, P. M. Chaikin, and E. Herbolzheimer, “Diffusing-wave spectroscopy,” *Phys. Rev. Lett.*, vol. 60, no. 12, pp. 1134–1137, Mar. 1988.
- [7] R. H. Brown and R. Q. Twiss, “Correlation between photons in two coherent beams of light,” *Nature*, vol. 177, no. 4497, pp. 27–29, 1956.
- [8] ———, “A test of a new type of stellar interferometer on sirius,” *Nature*, vol. 178, no. 4541, pp. 1046–1048, 1956.
- [9] J. Goodman, “Some effects of target-induced scintillation on optical radar performance,” *Proc. IEEE*, vol. 53, no. 11, pp. 1688–1700, 1965.
- [10] P. S. Idell, J. R. Fienup, and R. S. Goodman, “Image synthesis from nonimaged laser-speckle patterns,” *Opt. Lett.*, vol. 12, no. 11, pp. 858–860, Nov 1987.
- [11] L. I. Goldfischer, “Autocorrelation function and power spectral density of laser-produced speckle patterns,” *J. Opt. Soc. Am.*, vol. 55, no. 3, pp. 247–253, 1965.
- [12] I. Freund, M. Rosenbluh, and S. Feng, “Memory effects in propagation of optical waves through disordered media,” *Phys. Rev. Lett.*, vol. 61, no. 20, pp. 2328–2331, 1988.
- [13] I. Freund, “Correlation imaging through multiply scattering media,” *Phys. Lett. A*, vol. 147, no. 8, pp. 502–506, 1990.
- [14] J. Bertolotti, E. G. van Putten, C. Blum, A. Lagendijk, W. Vos, and A. P. Mosk, “Non-invasive imaging through opaque scattering layers,” *Nature*, vol. 491, pp. 232 – 234, Nov 2012.

- [15] O. Katz and S. Gigan, “Non-invasive single-shot imaging through scattering layers and around corners via speckle correlations,” *Nat. Photon.*, vol. 8, no. 10, pp. 784–790, aug 2014.
- [16] I. S. Reed, “On a moment theorem for complex Gaussian processes,” *IRE Trans. Inform. Theory*, vol. 8, no. 3, pp. 194–195, April 1962.
- [17] M. A. Webster, K. J. Webb, and A. M. Weiner, “Temporal response of a random medium from third-order laser speckle frequency correlations,” *Phys. Rev. Lett.*, vol. 88, p. 033901, Jan 2002.
- [18] J. A. Newman and K. J. Webb, “Fourier magnitude of the field incident on a random scattering medium from spatial speckle intensity correlations,” *Opt. Lett.*, vol. 37, no. 7, pp. 1136–1138, Apr 2012.
- [19] J. A. Newman, Y. Chen, and K. J. Webb, “Zero-mean circular bessel statistics and anderson localization,” *Phys. Rev. E*, vol. 90, p. 022119, Aug 2014.
- [20] J. A. Newman, Q. Luo, and K. J. Webb, “Imaging hidden objects with spatial speckle intensity correlations over object position,” *Phys. Rev. Lett.*, vol. 116, no. 7, p. 73902, feb 2016.
- [21] Q. Luo, J. A. Newman, and K. J. Webb, “Motion-based coherent optical imaging in heavily scattering random media,” *Opt. Lett.*, vol. 44, no. 11, pp. 2716–2719, 2019.
- [22] W. H. Peters and W. F. Ranson, “Digital Imaging Techniques In Experimental Stress Analysis,” *Optical Engineering*, vol. 21, no. 3, pp. 427 – 431, 1982. [Online]. Available: <https://doi.org/10.1117/12.7972925>
- [23] Z. Peng and K. E. Goodson, “Subpixel displacement and deformation gradient measurement using digital image/speckle correlation,” *Optical Engineering*, vol. 40, pp. 40 – 40 – 8, 2001.
- [24] C. W. J. Beenakker, “Random-matrix theory of quantum transport,” *Rev. Mod. Phys.*, vol. 69, pp. 731–808, Jul 1997.
- [25] D. S. Wiersma, “Disordered photonics,” *Nature Photon.*, vol. 7, no. 3, pp. 188–196, 2013.
- [26] B. Redding, M. A. Choma, and H. Cao, “Speckle-free laser imaging using random laser illumination,” *Nature Photon.*, vol. 6, no. 6, pp. 355–359, 2012.
- [27] S. Popoff, G. Lerosey, M. Fink, A. C. Boccarda, and S. Gigan, “Image transmission through an opaque material,” *Nat. Commun.*, vol. 1, p. 81, 2010.
- [28] O. Katz, E. Small, Y. Bromberg, and Y. Silberberg, “Focusing and compression of ultrashort pulses through scattering media,” *Nature Photon.*, vol. 5, no. 6, pp. 372–377, 2011.
- [29] I. M. Vellekoop and A. P. Mosk, “Focusing coherent light through opaque strongly scattering media,” *Opt. Lett.*, vol. 32, no. 16, pp. 2309–2311, 2007.
- [30] I. Freund, “Looking through walls and around corners,” *Physica A*, vol. 168, no. 1, pp. 49–65, 1990.

- [31] B. Judkewitz, Y. M. Wang, R. Horstmeyer, A. Mathy, and C. Yang, "Speckle-scale focusing in the diffusive regime with time reversal of variance-encoded light (TROVE)," *Nature Photon.*, vol. 7, pp. 300–305, Oct. 2013.
- [32] O. Katz, E. Small, and Y. Silberberg, "Looking around corners and through think turbid layers in real time with scattered incoherent light," *Nature Photon.*, vol. 6, pp. 549–553, Feb. 2012.
- [33] S. M. Popoff, , A. Aubry, G. Lerosey, M. Fink, A. C. Boccara, and S. Gigan, "Exploiting the time-reversal operator for adaptive optics, selective focusing, and scattering pattern analysis," *Phys. Rev. Lett.*, vol. 107, p. 263901, Dec. 2011.
- [34] R. Berkovits and S. Feng, "Theory of speckle-pattern tomography in multiple-scattering media," *Phys. Rev. Lett.*, vol. 65, no. 25, pp. 3120–3123, Dec. 1990.
- [35] P. N. den Outer, T. M. Nieuwenhuizen, and A. Lagendijk, "Location of objects in multiple-scattering media," *J. Opt. Soc. Am. A*, vol. 10, no. 6, pp. 1209–1218, June 1993.
- [36] G. Cao, V. Gaidin, C. A. Bouman, and K. J. Webb, "Localization of an absorbing inhomogeneity in a scattering medium in a statistical framework," *Opt. Lett.*, vol. 32, pp. 3026–3028, 2007.
- [37] S. R. Arridge and M. Schweiger, "Inverse methods for optical tomography," *Proc. of Information Processing in Medical Imaging*, 1993.
- [38] A. B. Milstein, S. Oh, K. J. Webb, C. A. Bouman, Q. Zhang, D. A. Boas, and R. P. Millane, "Fluorescence optical diffusion tomography," *Appl. Opt.*, vol. 42, no. 16, pp. 3081–3094, June 2003.
- [39] K. A. Nugent, T. E. Gureyev, D. F. Cookson, D. Paganin, and Z. Barnea, "Quantitative phase imaging using hard x rays," *Phys. Rev. Lett.*, vol. 77, no. 14, pp. 2961–2964, Sept. 1996.
- [40] K. S. Morgan, D. M. Paganin, and K. K. W. Siu, "X-ray phase imaging with a paper analyzer," *Appl. Phys. Lett.*, vol. 100, p. 124102, 2012.
- [41] S. Feng, C. Kane, P. A. Lee, and A. D. Stone, "Correlations and fluctuations of coherent wave transmissions through disordered media," *Phys. Rev. Lett.*, vol. 61, no. 7, pp. 834–837, August 1988.
- [42] A. Papoulis and S. U. Pillai, *Probability, Random Variables, and Stochastic Processes*. McGraw-Hill, 2002.
- [43] R. Berkovits, "Sensitivity of the multiple-scattering speckle pattern to the motion of a single scatterer," *Physical Review B*, vol. 43, no. 10, p. 8638, 1991.
- [44] J. R. Fienup, "Reconstruction of a complex-valued object from the modulus of its fourier transform using a support constraint," *J. Opt. Soc. Am. A*, vol. 4, no. 1, pp. 118–123, 1987.
- [45] A. W. Lohmann and B. Wirnitzer, "Triple correlations," *Proc. of the IEEE*, vol. 72, no. 7, pp. 889–901, 1984.

- [46] Z. Wang, M. A. Webster, A. M. Weiner, and K. J. Webb, "Polarized temporal impulse response for scattering media from third-order frequency correlations of speckle intensity patterns," *J. Opt. Soc. Am. A*, vol. 23, no. 12, pp. 3045–3053, Dec. 2006.
- [47] M. Davy, Z. Shi, and A. Z. Genack, "Focusing through random media: Eigen-channel participation number and intensity correlation," *Phys. Rev. B*, vol. 85, p. 035105, Jan 2012.
- [48] R. Horstmeyer, H. Ruan, and C. Yang, "Guidestar-assisted wavefront-shaping methods for focusing light into biological tissue," *Nat. Photon.*, vol. 9, no. 9, pp. 563–571, 2015.
- [49] Y. Liu, C. Ma, Y. Shen, J. Shi, and L. V. Wang, "Focusing light inside dynamic scattering media with millisecond digital optical phase conjugation," *Optica*, vol. 4, no. 2, pp. 280–288, Feb 2017.
- [50] Y. Chen, J. A. Newman, and K. J. Webb, "Circular Bessel statistics: derivation and application to wave propagation in random media," *J. Opt. Soc. Am. A*, vol. 31, no. 12, pp. 2744–2752, Dec 2014.
- [51] J. A. Rodriguez, R. Xu, C. C. Chen, Y. Zou, and J. Miao, "Oversampling smoothness: an effective algorithm for phase retrieval of noisy diffraction intensities," *J. Appl. Crystallogr.*, vol. 46, no. 2, pp. 312–318, apr 2013.
- [52] J. L. Sandell and T. C. Zhu, "A review of in-vivo optical properties of human tissues and its impact on PDT," *J. Biophotonics*, vol. 4, no. 11-12, pp. 773–787, 2011.
- [53] J. R. Fienup, "Phase retrieval algorithms: a comparison," *Appl. Opt.*, vol. 21, no. 15, pp. 2758–2769, 1982.
- [54] J. D. Briers, "Laser doppler, speckle and related techniques for blood perfusion mapping and imaging," *Physiol. Meas.*, vol. 22, no. 4, p. R35, 2001.
- [55] B. Z. Bentz, T. C. Wu, V. Gaiand, and K. J. Webb, "Diffuse optical localization of blood vessels and 3D printing for guiding oral surgery," *Appl. Opt.*, vol. 56, no. 23, pp. 6649–6654, 2017.
- [56] V. Plaks, C. D. Koopman, and Z. Werb, "Circulating tumor cells," *Science*, vol. 341, no. 6151, pp. 1186–1188, 2013.
- [57] J. Bercoff, M. Tanter, and M. Fink, "Supersonic shear imaging : a new technique," *IEEE Trans. Ultrason., Ferroelect., Freq. Control*, vol. 51, no. 4, pp. 396–409, 2004.
- [58] M. A. Webster, T. D. Gerke, A. M. Weiner, and K. J. Webb, "Spectral and temporal speckle field measurements of a random medium," *Opt. Lett.*, vol. 29, no. 13, pp. 1491–1493, 2004.
- [59] H. Zhuang, H. He, X. Xie, and J. Zhou, "High speed color imaging through scattering media with a large field of view," *Sci. Rep.*, vol. 6, no. August, p. 32696, 2016.

- [60] T. Kohlgraf-Owens and A. Dogariu, "Finding the field transfer matrix of scattering media," *Opt. Express*, vol. 16, no. 17, pp. 13 225–13 232, 2008.
- [61] F. Helmchen and W. Denk, "Deep tissue two-photon microscopy," *Nat. Methods*, vol. 2, no. 12, p. 932, 2005.
- [62] C. Ma, X. Xu, Y. Liu, and L. V. Wang, "Time-reversed adapted-perturbation (TRAP) optical focusing onto dynamic objects inside scattering media," *Nat. Photon.*, vol. 8, no. 12, pp. 931–936, nov 2014.
- [63] E. H. Zhou, H. Ruan, C. Yang, and B. Judkewitz, "Focusing on moving targets through scattering samples," *Optica*, vol. 1, no. 4, pp. 227–232, oct 2014.
- [64] D. A. Boas and A. K. Dunn, "Laser speckle contrast imaging in biomedical optics," *J. Biomed. Opt.*, vol. 15, no. 1, pp. 011 109–011 109, 2010.
- [65] A. K. Dunn, H. Bolay, M. A. Moskowitz, and D. A. Boas, "Dynamic imaging of cerebral blood flow using laser speckle," *J. Cereb. Blood Flow Metab.*, vol. 21, no. 3, pp. 195–201, 2001.
- [66] A. Fercher and J. Briers, "Flow visualization by means of single-exposure speckle photography," *Opt. Commun.*, vol. 37, no. 5, pp. 326–330, jun 1981. [Online]. Available: <http://www.sciencedirect.com/science/article/pii/0030401881904284>
- [67] J. H. Li and A. Z. Genack, "Correlation in laser speckle," *Phys. Rev. E*, vol. 49, no. 5, pp. 4530–4533, May 1994.
- [68] Y. Bromberg and H. Cao, "Generating non-rayleigh speckles with tailored intensity statistics," *Phys. Rev. Lett.*, vol. 112, no. 21, p. 213904, 2014.
- [69] A. L. Moustakas, H. U. Baranger, L. Balents, A. M. Sengupta, and S. H. Simon, "Communication through a diffusive medium: coherence and capacity," *Science*, vol. 287, pp. 287–290, Jan. 14 2000.
- [70] F. Lemoult, G. Lerosey, J. de Rosny, and M. Fink, "Manipulating spatiotemporal degrees of freedom of waves in random media," *Phys. Rev. Lett.*, vol. 103, no. 17, p. 173902, 2009.
- [71] R. Pappu, B. Recht, J. Taylor, and N. Gershenfeld, "Physical one-way functions," *Science*, vol. 297, no. 5589, pp. 2026–2030, 2002.
- [72] J. F. Barrera, R. Henao, M. Tebaldi, R. Torroba, and N. Bolognini, "Multiple-encoding retrieval for optical security," *Opt. Commun.*, vol. 276, no. 2, pp. 231–236, 2007.
- [73] B. Redding, S. F. Liew, R. Sarma, and H. Cao, "Compact spectrometer based on a disordered photonic chip," *Nature Photon.*, vol. 7, no. 9, p. 746, 2013.
- [74] A. Z. Genack, "Optical transmission in disordered media," *Phys. Rev. Lett.*, vol. 58, no. 20, pp. 2043–2046, 1987.
- [75] S. Popoff, G. Lerosey, M. Fink, A. C. Boccara, and S. Gigan, "Controlling light through optical disordered media: transmission matrix approach," *New J. Phys.*, vol. 13, no. 1, p. 123021, Dec. 2011.

- [76] A. Mosk, A. Lagendijk, G. Lerosey, and M. Fink, “Controlling waves in space and time for imaging and focusing in complex media,” *Nature Photon.*, vol. 6, no. 5, pp. 283–292, 2012.
- [77] T. Chaigne, O. Katz, A. C. Boccara, M. Fink, E. Bossy, and S. Gigan, “Controlling light in scattering media non-invasively using the photoacoustic transmission matrix,” *Nature Photon.*, vol. 8, no. 1, pp. 58–64, Nov. 2013.
- [78] K. J. Webb, Y. Chen, and T. A. Smith, “Object motion with structured optical illumination as a basis for far-subwavelength resolution,” *Phys. Rev. Appl.*, vol. 6, no. 2, p. 024020, 2016.
- [79] A. J. F. Siegert, *MIT Rad Lab Rep No 465*. Massachusetts Institute of Technology, Cambridge, MA, 1943.
- [80] M. A. Webster, K. J. Webb, A. M. Weiner, J. Xu, and H. Cao, “Temporal response of a random medium from speckle intensity frequency correlations,” *J. Opt. Soc. Am. A*, vol. 20, no. 11, pp. 2057–2070, 2003.
- [81] J. A. Newman and K. J. Webb, “Imaging optical fields through heavily scattering media,” *Phys. Rev. Lett.*, vol. 113, p. 263903, Dec 2014.
- [82] P. Sheng, *Scattering and Localization of Classical Waves in Random Media*. World Scientific Pub Co Inc, 1990, vol. 8.
- [83] S. Feng and P. A. Lee, “Mesoscopic conductors and correlations in laser speckle patterns,” *Science*, vol. 251, pp. 633–639, February 1991.
- [84] R. Berkovits and S. Feng, “Correlations in coherent multiple scattering,” *Phys. Rep.*, vol. 238, no. 3, pp. 135–172, 1994.
- [85] M. C. W. van Rossum and T. M. Nieuwenhuizen, “Multiple scattering of classical waves: microscopy, mesoscopy, and diffusion,” *Rev. Mod. Phys.*, vol. 71, no. 1, pp. 313–371, January 1999.
- [86] F. Scheffold, W. Hartl, G. Maret, and E. Matijevic, “Observation of long-range correlations in temporal intensity fluctuations in light,” *Phys. Rev. B*, vol. 56, no. 17, pp. 10 942–10 952, November 1997.
- [87] Z. Wang, K. J. Webb, and A. M. Weiner, “Coherent incident field information through thick random scattering media from speckle correlations over source position,” *Appl. Opt.*, vol. 49, no. 30, pp. 5899–5905, 2010.
- [88] P. W. Shor and J. Preskill, “Simple proof of security of the bb84 quantum key distribution protocol,” *Phys. Rev. Lett.*, vol. 85, no. 2, p. 441, 2000.
- [89] D. V. Strekalov, A. V. Sergienko, D. N. Klyshko, and Y. H. Shih, “Observation of two-photon “ghost” interference and diffraction,” *Phys. Rev. Lett.*, vol. 74, no. 18, pp. 3600–3603, May 1995.
- [90] F. Ferri, D. Magatti, A. Gatti, M. Bache, E. Brambilla, and L. A. Lugiato, “High-resolution ghost image and ghost diffraction experiments with thermal light,” *Phys. Rev. Lett.*, vol. 94, no. 18, p. 183602, May 2005.
- [91] K. W. C. Chan, M. N. O’Sullivan, and R. W. Boyd, “High-order thermal ghost imaging,” *Opt. Lett.*, vol. 34, no. 21, pp. 3343–3345, 2009.

- [92] K. W. C. Chan, D. S. Simon, A. V. Sergienko, N. D. Hardy, J. H. Shapiro, P. B. Dixon, G. A. Howland, J. C. Howell, J. H. Eberly, M. N. O'Sullivan *et al.*, "Theoretical analysis of quantum ghost imaging through turbulence," *Phys. Rev. A*, vol. 84, no. 4, p. 043807, 2011.
- [93] S. Sun, H. Lin, Y. Xu, J. Gu, and W. Liu, "Tracking and imaging of moving objects with temporal intensity difference correlation," *Opt. Express*, vol. 27, p. 27851, 2019.
- [94] F. Zäh, M. Halder, and T. Feurer, "Amplitude and phase modulation of time-energy entangled two-photon states," *Opt. Express*, vol. 16, no. 21, pp. 16 452–16 458, 2008.
- [95] T. Förster, "Zwischenmolekulare energiewanderung und fluoreszenze," *Ann. Physik*, vol. 2, p. 55, 1948.
- [96] J. Zhang, R. Campbell, A. Ting, and R. Tsien, "Creating new fluorescent probes for cell biology," *Nature*, vol. 3, pp. 906–918, 2002.
- [97] V. Gaiand, S. Kularatne, P. S. Low, and K. J. Webb, "Deep-tissue imaging of intramolecular fluorescence resonance energy-transfer parameters," *Opt. Lett.*, vol. 35, no. 9, pp. 1314–1316, 2010.
- [98] E. H. Tsai, B. Z. Bentz, V. Chelvam, V. Gaiand, K. J. Webb, and P. S. Low, "In vivo mouse fluorescence imaging for folate-targeted delivery and release kinetics," *Biomed. Opt. Express*, vol. 5, no. 8, pp. 2662–2678, 2014.
- [99] J. A. Leendertz, "Interferometric displacement measurement on scattering surfaces utilizing speckle effect," *Journal of Physics E: Scientific Instruments*, vol. 3, no. 3, p. 214, 1970.
- [100] A. Macovski, S. D. Ramsey, and L. F. Schaefer, "Time-lapse interferometry and contouring using television systems," *Appl. Opt.*, vol. 10, no. 12, pp. 2722–2727, Dec 1971.
- [101] M. Takeda, H. Ina, and S. Kobayashi, "Fourier-transform method of fringe-pattern analysis for computer-based topography and interferometry," *J. Opt. Soc. Am.*, vol. 72, no. 1, pp. 156–160, Jan 1982.
- [102] O. J. Løkberg, "Recent developments in video speckle interferometry," in *Speckle Metrology*, R. S. Sirohi, Ed. New York: Marcel Dekker, 1993, vol. 38, ch. 4, pp. 157–194.
- [103] H. Tiziani, "Application of speckling for in-plane vibration analysis," *Opt Acta*, vol. 18, no. 12, pp. 891–902, 1971.
- [104] H.-M. Zhu, Y.-Y. Wu, W.-H. Zheng, and Z.-W. Huang, "In-plane and out-of-plane displacement measurement by ultrasonic speckle correlation method (USCM)," *Arch. Appl. Mech.*, vol. 75, no. 8-9, pp. 521–526, 2006.
- [105] Y.-C. Hsueh and K. J. Webb, "Electromagnetic field control with binary aperiodic nanostructures," *J. Opt. Soc. Am. B*, vol. 34, no. 10, pp. 2059–2071, Oct 2017.

- [106] W. Choi, A. P. Mosk, Q.-H. Park, and W. Choi, “Transmission eigenchannels in a disordered medium,” *Phys. Rev. B*, vol. 83, p. 134207, Apr 2011.
- [107] S. Rotter and S. Gigan, “Light fields in complex media: Mesoscopic scattering meets wave control,” *Rev. Mod. Phys.*, vol. 89, p. 015005, Mar 2017.
- [108] A. Goetschy and A. D. Stone, “Filtering random matrices: The effect of incomplete channel control in multiple scattering,” *Phys. Rev. Lett.*, vol. 111, p. 063901, Aug 2013.

VITA

VITA

Grew up in Hefei, China, Qiaoen Luo received a full scholarship from Ministry of Education of Singapore to continue his study abroad at the age of 15. After graduating from River Valley High School and Hwa Chong Junior Collge , Qiaoen went on to University College London to study Physics. He spent the summer of 2012 working as a research intern in Professor Peter Török's group at Imperial College, learning optical microscopy and designing specific experiments. Later, working closely with Professor Ian Robinson and Dr Fucai Zhang, he completed his final year project about optical ptychographic tomography at Research Complex at Harwell. In Fall 2013, Qiaoen began his direct PhD program at Purdue University in Professor Kevin J. Webb's group, focusing on developing coherent imaging method through scatter. As a research assistant he contributed to grant proposals and reports and attended several conferences. The chapters of this dissertation have been submitted for publication in various journals.